The aerodynamic effects of the location of baseball seams:

An experimental study by PIV

Jorian Knepper

TU Delft

The aerodynamic effects of the location of baseball seams:

An experimental study by PIV

To obtain the degree of Master of Science at the Delft University of Technology, to be defended publicly on [DATE TBD]

Jorian Knepper

Student number: 4178521

TU Delft

DELFT UNIVERSITY OF TECHNOLOGY DEPARTMENT OF AERODYNAMICS

The undersigned hereby certify that they have read and recommend to the Faculty of Aerospace Engineering for acceptance the thesis entitled “The aerodynamic effects of the seam locations of a slow rotating baseball on the wake, a 2D planar PIV study.” by Jorian Knepper in fulfillment of the requirements for the degree of Master of Science.

Thesis committee

Dated:

_____

Name 1:

_____

Name 2:

_____

Name 3:

_____

Name 4:

_____

Preface

This thesis has been written at the Technical University of Delft as part of my master program at the TU Delft. The goal was to investigate the flow fields around a slow rotating baseball for a Reynolds number of 150,000. During the thesis I have been able to enjoy the works of experimental aerodynamics in sports, with the focus on planar PIV.

I would like to express my gratitude to Dr. Andrea Sciacchitano for this chance, as well as for all his valuable time, support and knowledge he has provided me. I would also like to Dr. Ir. Wouter Terra for providing much appreciated feedback and ideas on the report, as well as different insight into sport. Also a special thanks goes to my study group, helping me keep my focus, for taking a genuine interest and providing a much appreciated work area.

I would also like to thank Peter Duyndam, Nico van Beek, Frits Donker, Dennis Bruikman and Henk-Jan Siemer for providing their valuable time and helping to set-up and correct the experimental set-up. In addition, the help of Ir. Edoardo Saredi and Ir. Kushal Ujjaini Kempaiah proved to be vital to understand and solve the problem of the laser misalignment.

Also I would also like to express thanks to my friends, who helped me relax, gave me advice and kept me going, even when I had some difficulties focusing. And finally, gratitude goes out to my family, who always were interested in the work I did, who read the whole thesis and asked a lot of interesting questions and made me comfortable while I was working on my report and kept my spirit high, even when not everything went according to plan. Without everybody, this would not have been possible. Thank you!

Jorian Knepper
Delft, Februari 2022

Abstract

The aerodynamic behaviour for a baseball is conventionally researched by measuring the curve of a baseball during a pitch with a start and end location. From this deflection the aerodynamic forces are derived and statements about the drag and lift can be made. Other experiments entail free flight, for which the repetition rate is lower or CFD models, which entail adaptations to the reality and numerical problems. New insights came by having fully statistically converged flow fields due to wind tunnel testing, due to having a high repeatability rate. These experiments show for different Reynolds numbers the aerodynamic behaviour of a baseball. However, often these measurements are conducted on static (= non-rotating) baseballs. Here however lies an omission of an interesting area in the research field. For a small spin factor, different configurations show a differing lift coefficient. When increasing the spin factor above a threshold, these values tend to coincide and move linear with increasing spin rate.

In order to understand this behaviour of the baseball therefore this thesis is focused on a windtunnel test with planar PIV, with the addition of rotational device. This approach allows for testing both static and rotating baseballs and with a fully converged flow field and a visual understanding of what is happening locally instead of deriving the forces and coefficients as a result. For this thesis the 2 mostly used pitches (the ”two-seam” and ”four-seam”, named after how many columns of seams appear in a 360° rotation, see Chapter 1) are researched, as well as a smooth sphere for a reference. These wind tunnel measurements were conducted in the Aerodynamics Laboratory of TU Delft. The free stream velocity was maintained at 30 m/s, with a test section of 40x40 cm^2 with the equivalent Reynolds number of about 150,000. Due to the time constraint of this thesis not the full 3D flow field is investigated. Instead the experimental approach opted for is planar PIV (2D2C). As a full 3D field is missing, an adaptation has to be made from the flow field to some lift proxy parameter, that can be used to compare it with earlier found data to validate the results and can be visually compared to research the difference in lift for different configurations. This is done by comparing the shift in centre of gravity from the recirculation area (the area inside the wake where the streamwise velocity component is zero) with the momentum theory of a 2D control volume approach, generating a lift proxy parameter.

The static results indicate different regions where the seams do not influence the flow clearly, where the seams cause early separation (separation point on the seam location) and where the seam causes flow tripping and hence delaying separation. These results can be combined into an image where the effects of the seams over the baseball are demonstrated. For the 2-seam configuration it can be seen that the highest positive deflection of the centre of gravity of the recirculation area is when the front seam is at approximately 90°, which should also hold for -90°, as per argument of symmetry. Also the seams in the front cause a relative high centre of gravity shift when the seams are both on 1 side (upper or lower). More counter intuitive is a similar shift occurring when the 2 seam are in the back, indicating that 3D flow effects play a similar part like directly flow tripping of the in plane seams. The 4 seam shows a more on/off behaviour due to a seam appearing every 90°, where either the seam causes separation (around (-)90°), or where the seam in front causes flow tripping and a delayed separation instead is seen. Following the separation at the seam for the 4-seam configuration, a relative large recirculation area is observed, as opposed to both tripping on the upper and lower side, yielding a small recirculation area.

This observation for the static cases also explains the difference when the ball has a small rotation. The 4-seam case has more tripping layers (= seams) and they appear more frequent (every approximately 90°). Therefore with the same free stream velocity and spin rate, a smaller recirculation area appears, which with the same momentum can be displaced further, relating to a larger lift force in opposite direction than the 2-seam case. Here the seams appear less frequent, with less tripping as a consequence and a larger wake. When increasing the RPM, the frequency of the seam becomes high enough to

create similar separation behaviour as for the 4-seam and the shift in centre of gravity becomes similar, which corresponds with the trend found in literature, as shown by Alaways [6]. From these observations and theories it is hence explained how and why the 2-seam and 4-seam configuration differ in lift coefficient for small spin factors.

Contents

List of Figures

List of Tables

Nomenclature

Γ	circulation	$[m\ N\ s/kg]$
δ^*	displacement thickness	$[m]$
δ_z	depth of field	$[m]$
δ_t	pulse duration	$[s]$
λ	wavelength of laser light	$[m]$
ρ	density	$[kg/m^3]$
ρ_p	density of the particle	$[kg/m^3]$
ρ_f	density of the flow	$[kg/m^3]$
μ	dynamic viscosity	$[kg/(m\ s)]$
ν	kinematic viscosity	$[m^2/s]$
ϕ	angle	$[^\circ]$
ω	angular velocity	$[1/s]$

A	surface	$[m^2]$
a	radius flow particle	$[m]$
C_d	drag coefficient 2D	$[-]$
C_D	drag coefficient 3D	$[-]$
C_L	lift coefficient 3D	$[-]$
C_l	lift coefficient 2D	$[-]$
C_Y	side-force coefficient 3D	$[-]$
D	drag	$[N]$
d	diameter object	$[m]$
d_p	diameter particle	$[m]$
d_τ	particle image diameter	$[m]$
d_{geom}	geometrical image diameter	$[m]$
d_{diff}	diffraction image diameter	$[m]$
f	frequency	$[1/s]$
f	focal length	$[m]$
$f\#$	f stop	$[-]$
F	force	$[N]$
k	surface roughness	$[m]$
k_{curv}	path curvature	$[1/m]$
L	lift	$[N]$
L'	lift per meter	$[N/m]$
l	length	$[m]$
m	mass	$[kg]$
M	magnificiation factor	$[-]$
P	pressure	$[N/m^2]$
q	normalised diameter	$[N/m^2]$
r	radius	$[m]$
Re	Reynolds number	$[-]$
S	spin rate	$[-]]$
t	time	$[s]$
u	streamwise velocity component	$[m/s^2]$
u'	change in streamwise velocity component	$[m/s^2]$
v	normal velocity component	$[m/s^2]$
v'	change in normal velocity component	$[m/s^2]$
V	velocity	$[m/s^2]$
V_{rot}	rotational Velocity	$[m/s^2]$
V_{flow}	free stream velocity	$[m/s^2]$
U	free stream velocity	$[m/s^2]$
Y	acceleration	$[N]$
y_{cg}	centre of gravity	$[cm]$
Z_0	object distance	$[m]$
z_0	image distance	$[m]$

CFD	computational fluid dynamics	–
2D−2C	two dimensional and two component	–
2D−3C	two dimensional and three component	–
3D−3C	three dimensional and three component	–
RPM	rotations per minute	$[rev/min]$
PIV	particle image velocimetry	–
Nd YAG	neodymium-doped yttrium aluminium garnet	–
TSA	top separation angle	[°]
BSA	bottom separation angle	[°]
StD	standard deviation	[-]
Avg	average calculated by the average velocity field	$[-]$
Mean	mean calculated by the average values of the individual instantaneous images	$[-]$
recirc	recirculation area	$[cm^2]$

1

Introduction

Baseballs can deviate from their original trajectory. The lateral deflection from this path in flight is called swing, curve, swerve or break. However, these are just baseball terms to qualify what the eye sees and holds bias. For this thesis the terms curve and break will be used for gradual curvature due to constant force (curve) and a sudden erratic movement due to a peak force (break). The way a baseball spins and moves has always sparked a great debate in the baseball community. Before the 1950's there was even a debate whether a curving baseball actually existed or that it was an optical illusion. Documentation was the main issue and although already in 1877 (Cincinnatti experiment, [6]) and with various other experiments it was proven that baseballs did curve, the curve discussion was still not resolved more than 60 years later. More experiments were performed to conclude that a baseball actually curved. The experiments that were performed ranging from pitching baseballs through wooden frames with strings (to monitor the broken strings to visualize a path [52]) to tracking the baseballs with multi-flash and camera images.

The speed of a common professional pitched baseball is measured between 75-105.1 mph, the latter record belonging to Aroldis Chapman [31]. This is between 120.7 and 169.1 km/h This is the fastest recorded pitch, however it is believed 2 other people actually "broke" the record before, but the recording was not that accurate. Nolan Ryan pitched 100.8 miles per hour. Only, this was measured after crossing the plate [31]. This measuring location would lead to an estimated loss of 3 to 7% of the initial velocity.

The rpm of a thrown baseball is around 2200 rpm to 2600 rpm for the most common pitch (4 seam) [48]. The distance from pitch plate to end plate is originally 60 feet 6 inches, but this does not include the smuggled distance from the pitcher. Considering a 100mph fastball, it reaches the home plate under 400 milliseconds, while the swing takes circa 150 milliseconds. That gives the batter only 250 milliseconds, while the human reaction time of top sprinters is recorded to be 142 milliseconds [28]. This indicates that the baseball player almost immediately must make an educated guess whether to try to hit the ball and where. Tricking the batter (by understanding and using curve) into making wrong guesses is therefore the main goal of a pitcher.

Before diving deeper into the why and how of the curve, it is important to understand how a baseball looks and where the seams are located. The official specification by the Major Baseball League states: "The ball shall be a sphere formed by yarn wound around a small core of cork, rubber or similar material, covered with two strips of white horsehide or cowhide, tightly stitched together. It shall weigh not less than five nor more than 5 ¼ oz. avoir dupois and measure not less than nine nor more than 9¼ in. in circumference." [34]. This corresponds to 142 - 149 grams and a circumference of 22,9 - 23,5 cm.

A view of the baseball, along with different angles is given by Figure 1.1 and 1.2. Typically the seams

are 2.24m long and have 106 double stitches. The height of the seam is generally less than 1 mm for the official baseball with radius 36.4 mm [35]. The baseball (wake) forms a 3 dimensional problem involving boundary layer phenomena like separation. Therefore 3 different axes and 2 rotational axes have to be studied [35]. In baseball, pitches rotating around those 2 axes are known as the 4 seam and 2 seam. The name is based on how many columns of seams appear to the public in vertical way. In the 4 seam (Figure 1.2) it rotates around the z-axis, meaning that there are a total of 4 vertical columns of seams per rotation. 2 columns are seen for a=0° and 2 columns for a=180°, totalling 4 or 1 column of seams per 90° starting from a=45°. The 2 seam orientation rotates around the y-axis (Figure 1.2), meaning that there a 2 vertical columns per rotation.

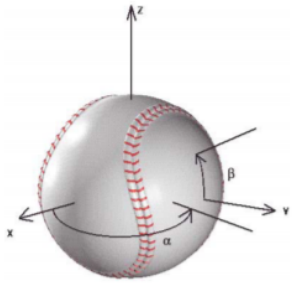

Figure 1.1: A baseball with rotational axes [35]

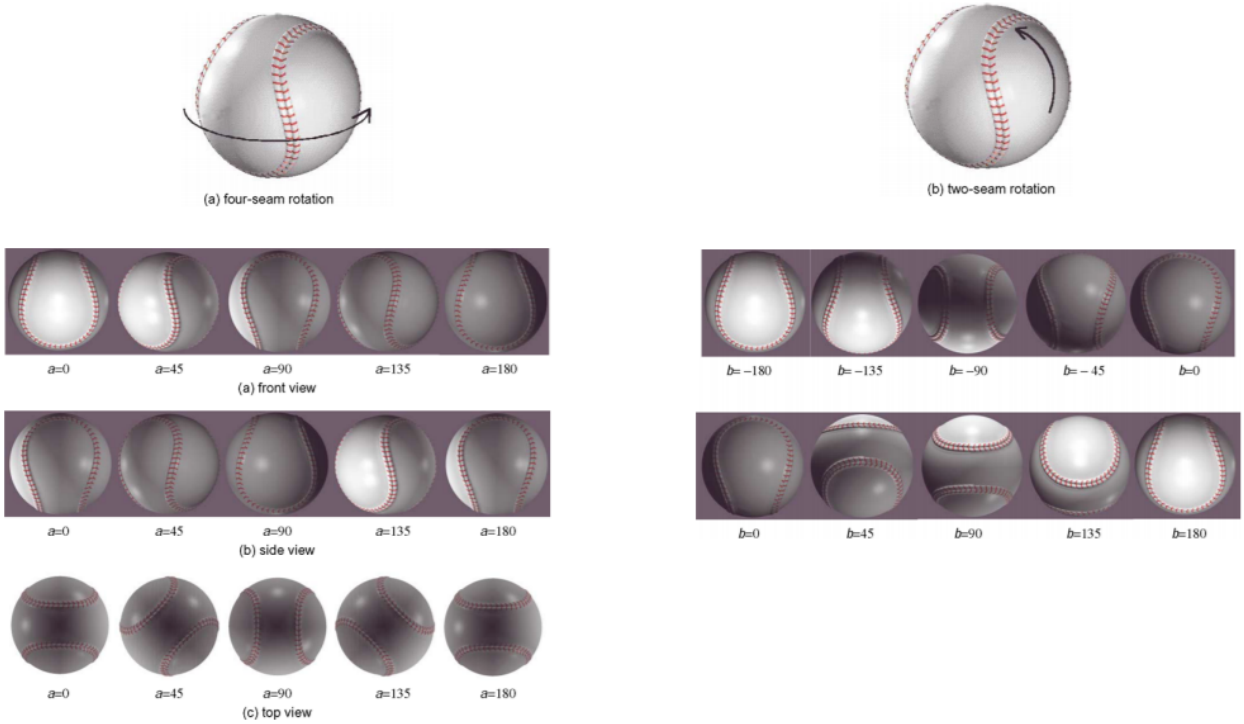

Figure 1.2: Rotational view of a baseball [35]

The ball is not axisymmetric, but has planes of symmetry. It is also clear that when the ball rotates the seams will have a different azimuth with respect to the reference frame (front view). A frame by frame capture of the rotation of the baseball in the 2 major rotations axes can be seen in Figure 1.1 and 1.2. This asymmetrical quantity is the source of some ”erratic” movements in baseball.

Nowadays more elegant and efficient ways of experimenting are available, like Computational Fluid Dynamics (CFD) and Particale Image Velocimetry (PIV) in a windtunnel. This research is focused on PIV. This research investigates the flow field around both rotating and non-rotating baseballs to assess the aerodynamic effects associated with the presence of the seams. For analysing a slow or non-rotating baseball and comparing it to a smooth sphere, a windtunnel can be beneficial in combination with PIV. Here the high repetition rate of the experiment makes it possible to investigate different orientations and have a higher statistical convergence for the results. Also by visualizing the flow, the difference in the flow field for a 4 seam and 2 seam can be explained by investigating the effect of the seams.

Literature data indicates a difference in lift for the 2 seam and 4 seam configuration for a baseball, when there is a small spin factor. When increasing the spin factor above a threshold, these values tend to coincide and move parallel with increasing spin rate. At 0 spin, there is no lift in general for both cases, whereas for high spin factors the different configurations tend to converge to the same lift coefficient, as will be further demonstrated in Chapter 2. Most experiments from literature are conducted on static baseballs, hence not accounting for spin. Therefore this thesis focuses on analysing low spin configurations. This will lead to understanding how and why this occurs and this adaptation of knowledge can be used beneficially for a pitcher. Here he can let the baseball deflect more or less, just by changing the orientation of his pitch and can predict also the amount of deflection better.

Windtunnel measurements were conducted in the Aerodynamics Laboratory of TU Delft, leading to statistically converged flow fields for static baseballs at different orientations and rotating baseballs. The free-stream velocity was set to 30 m/s, relating to a Reynolds number of about 150,000. The goal of the research is to visualize flow fields of the baseballs for multiple configurations (both rotating and stationary). Due to the thesis with a limited time frame, not the full 3D flow field is investigated. Instead it is opted planar PIV (2D2C). This yields as an advantage an understanding of the (2D) flow, without the processing of more additional data for a full understanding of the 3D flow. Using enough 2D planar tests to get statistical convergence results in a lot of data (from the instantaneous flow fields) and also the different configurations (2 seam and 4 seam as well as rotating and non-rotating tests) give more data that needs to be collected and processed. Therefore testing in a windtunnel was chosen, as the repetition rate of the experiments is high and also the set-up is relative easy to switch.

The main focus of the study can be split into different research questions. The primary research question is:

“What is the effect of the location of the seams of a slow or non-rotating baseball (spin factor < 0.2) on the wake?”.

The means to research this are by visualizing the flow field with 2D planar PIV recording in a windtunnel. The primary research question cannot be answered in a quantifiable way directly, but will be divided into smaller sub questions. This will be done by investigating the shift in y centre of gravity (y_{cg}) of the recirculation area (the area inside the wake where the streamwise velocity component is zero) of a 2D flow-field and comparing it to the lift coefficient: *“Can the lift coefficient be compared with the y-centre of gravity of 2D planar PIV for baseballs and does it behave similarly?”*. This would make it possible to compare the intended data with the results from the lift coefficient of a baseball for low spin configurations. The next question will be *“At which angles can the seam influence be noticed to do nothing, cause transition or cause separation?”*, which would make it easier to predict the behaviour of the flow if a trend can be discovered here. Due to the flow tripping, also an expected change in behaviour should be observed in the statistics where this behaviour is triggered by specific location of the seam, whereas a flow without seams would have a less specific change in behaviour due to transition or separation: *“Does the stability of the separation angles, wake size and wake centre of gravity change for these specific seam cases?”* and *“How does the stability differ for different seam positions by looking at the mean and standard deviation of the y centre of gravity and separation angles?”*. The next step is to investigate the seam effects, while also having the Magnus effect and flow hysteresis: *“Is the perceived influence of the seams on the non-rotational baseball case different for small RPM and*

is this solely the Magnus effect or also a combination of the seam effects with Magnus effect and flow hysteresis?". By understanding these effects, the difference in the 2-seam and 4-seam can be found and can be related to literature data: *"Why do the 2-seam and 4- seam configurations have different lift coefficients for low spin factors (S < 0.2) baseballs by looking at the y centre of gravity?"*.

The literature part and the main area where this thesis can contribute is discussed in Chapter 2. Here from the basis of a smooth sphere aerodynamic properties are discussed and then extended to the baseball, which basically is a more rough sphere with seams. In Chapter 3 the ideas and practical implications of PIV are discussed. In Chapter 4 the experimental set-up is shown, as well as the post processing tools in Davis and Python. These results are shown in Chapter 5, where the static (= non-rotating) smooth sphere and baseball (2-seam and 4-seam configuration) are shown, followed by the rotating sphere and baseball and a comparison. This thesis is concluded in Chapter 6, where the research questions will be answered, the conclusion will be made and further recommendations are given.

2

Baseball aerodynamics

The aerodynamic behaviour of a baseball is a combination of that of a smooth sphere and the attached rough elements called the seams. Therefore this chapter will first discuss some properties of the smooth sphere, then focus on the importance of the seams and will conclude with some literature data from experiments and theory.

2.1. Flow around a smooth sphere

The most researched object close to a baseball is the smooth sphere. Even analytic models that are derived from potential flow give precise results for lift, although the drag is 0. The important differing aspect with the baseball, is the absence of seams. Also the surface is assumed smooth (effective roughness k/d = 0) and the ball is perfectly symmetrical with no geometrical or gravitational offsets. However, even for the smooth sphere there are different values for the drag coefficient C_D for different literature [1], see Figure 2.1.

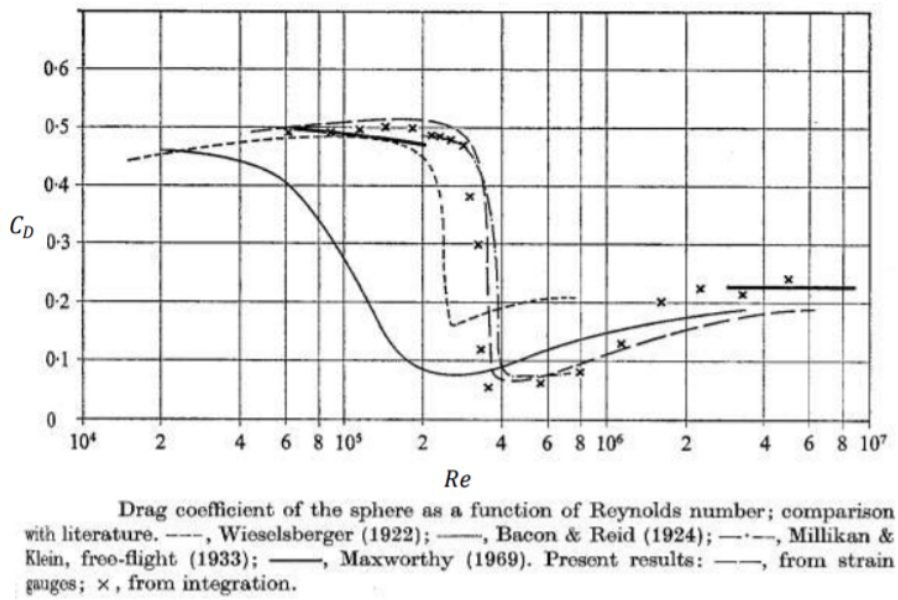

Drag coefficient of the sphere as a function of Reynolds number; comparison with literature. ---, Wieselsberger (1922); ——, Bacon & Reid (1924); —·—, Millikan & Klein, free-flight (1933); ——, Maxworthy (1969). Present results: ——, from strain gauges; ×, from integration.

Figure 2.1: Drag Coefficient smooth sphere for different studies [1] as a function of the Reynolds number

The Reynolds number is the ratio of the momentum convection and the viscous diffusion. It is also the ratio of inertia forces over viscous forces. see Equation 2.1. For aerodynamics it is often an indicator

if the flow is laminar, transition or turbulent.

$$Re = \frac{\rho V l}{\mu} \tag{2.1}$$

where Re is the Reynolds number [-], ρ is the density [m/s], l is the length of the object [m] and μ is the dynamic viscosity [kg · m / s]

Achenbach [1] pointed out that difference in lift and drag coefficients can occur from different boundary conditions with respect to turbulence level of the flow, the supports holding the ball, different balls with other dimensions, windtunnel blockage, different surface roughness and different scaling factors like mach number. Also the chosen calculation method can differ, as the measured factors differ from measuring directly the total drag to measuring the local static pressure or even deriving the drag from the skin friction distribution over the sphere.

2.1.1. Flow Regimes

The boundary layer is the area of the flow in close vicinity of the surface where the viscosity effects are influencing the flow. The flow follows the curvature of the surface while moving. The object in a flow is affected by the reaction of the flow on the surface and nearby disturbances. This area is the boundary layer, which has thickness (δ) and is defined between the surface and where the velocity is 99% of the external uniform flow velocity. The reason for this typical boundary layer structure lies in the frictional quantities of the surface. Due to the viscous shear forces, the velocity at the boundary is 0 and the velocity profile is curved. The boundary layer depends on the geometry of the object, surface roughness and Reynolds number and has a great influence on the aerodynamic properties of rotating and moving objects like sports balls.

For a laminar boundary layer, the exchange of momentum in vertical direction occurs due to shear stress. The scale at which this occurs is microscopic and molecular [51]. Mehta [45] describes this as smooth tiers of air passing on top of the other. On the other side, turbulent boundary layers have a much larger transverse transport of momentum. This is because of larger scale motions of fluid elements (air is moving more chaotically throughout the layer [45]). Hence, in addition to the laminar boundary layer, there is an effective turbulent shear stress. Flow velocities closer to the smooth sphere will be higher for a turbulent boundary layer versus a laminar boundary layer. As a consequence the turbulent boundary layer will have a higher skin-friction drag due to the shear forces [51].

Achenbach like others [1], researched the smooth sphere for high Reynolds numbers and found interesting behaviour for the drag coefficient. 4 regions were identified for the Reynolds number: Subcritical, Critical, Supercritical and Transcritical, see Figure 2.2. These sections helped to identify the behaviour of the drag coefficient and the prediction of the drag crisis, indicated by the critical range.

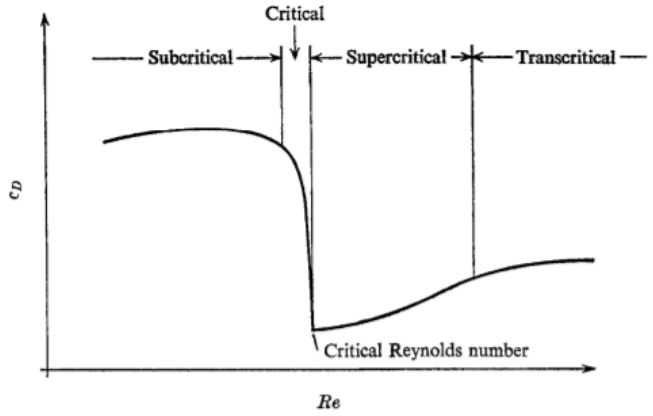

Figure 2.2: Smooth sphere: 4 regions identified by the Reynolds number [1]

The effect of the Reynolds number of the flow can be seen in Figure 2.3. Number 1 to 3 have a laminar Reynolds number (<2000), number 4 Re = 10^4 and number 5 has a Reynolds number of 10^5. A cylinder is chosen as an example, as this corresponds to a geometrical area that is not changing in the plane orthogonal to the measuring section and therefore has no additional 3D flow effects.

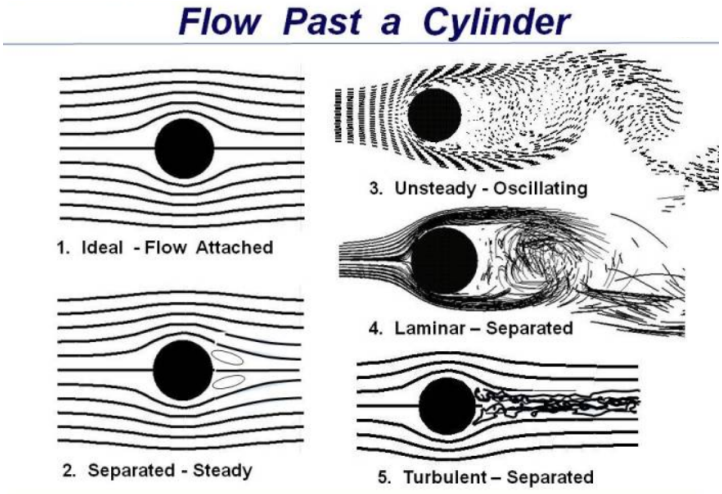

Figure 2.3: Reynolds number effect on cylinder flow [32]

For Figure 2.3, in the first picture the flow is creeping and stays around the cylinder, hence a fully attached wake. The air stagnates just before and after the cylinder. At this stagnation point the pressure is highest. However, as there is no flow separation, the pressure forces on both sides is nearly equal and no net force due to pressure is found. The only unbalanced force acting on the cylinder is the air friction or viscous drag. The second picture shows a steady separation bubble. Separation on both sides occurs at same point and the detached wake is similar size for both upper and lower side, hence no upwards or downwards force. In 4. the air behind the cylinder is not decelerated and the pressure is no longer large at the other side of the cylinder. Since there is still the stagnation point and highest pressure just in front of the cylinder, there is now a large pressure drag. This force is larger than the viscous drag and has a large influence on the velocity component. For scenario 5 the wake is fully turbulent. The flow lines separate from the object and follow the turbulent boundary layer. It corresponds to the laminar flow, but the aft part makes it look like a laminar flow around a different, more elongated object in the aft part [51]. However, this means still that the pressure behind the object rises and the frontal stagnation pressure is better counteracted, meaning that a smaller pressure drag occurs.

The transition location from laminar to turbulent (Figure 2.4) and separation location (Figure 2.5) were

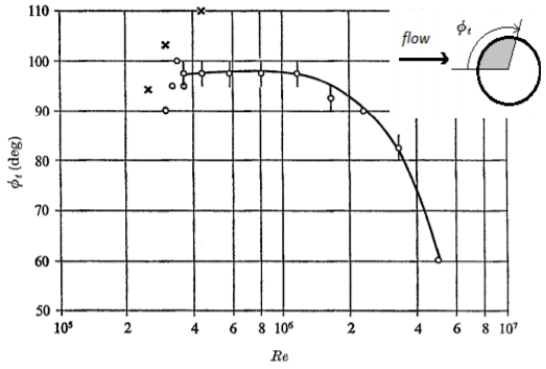

Figure 2.4: Smooth sphere: transition location as a function of Reynolds number[1]

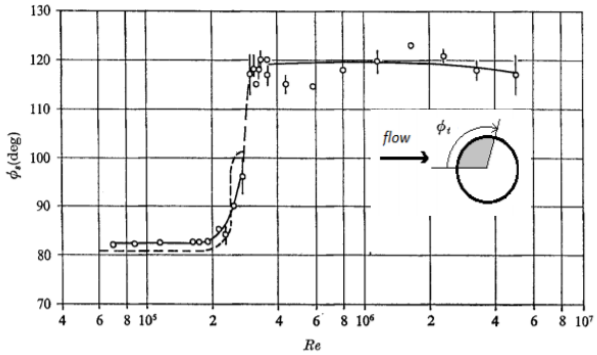

Figure 2.5: Smooth sphere: separation location as a function of the Reynolds number[1]

found for different Reynolds numbers. The difference and effects are observed when Achenbach compares his research to Maxworthy's. Here the transition point on the sphere is found at the same geometrical location. However, the transcritical drag coefficient is different. This indicates that although the flow separation point is similar, the energy distribution in the boundary layer is different [1].

From smooth spheres, it is known that a drag crisis occurs (for example Achenbach [1] [2]). A drag crisis means that the drag coefficient reduces rapidly, while increasing the speed (or the actual dimensionless measure of turbulence, the Reynolds number) only slightly, see Figure 2.2. The critical area is where the drag crisis occurs. This is due to the change in boundary layer, where the boundary layer becomes turbulent [29]. This influences the wake, making the area of negative pressure on the sides and back smaller and reducing the drag [3]

2.1.2. Magnus effect

Spin rate is dependent on the initial release conditions of the ball, the swirling of the ball relates better to circulation. Some comparisons between circulating flows can be made, like the Kutta-Joukowski theorem. Typically the lift is determined by the lift coefficient, surface and the dynamic pressure (Equation 2.2). The lift in 2D case can also be calculated using the Kutta-Joukowski theorem (Equation 2.3). This gives a relation between the circulation and the lift coefficient.

$$L = \frac{\rho C_L A V^2}{2} \frac{\boldsymbol{\omega} \times \mathbf{V}}{|\boldsymbol{\omega} \times \mathbf{V}|} \tag{2.2}$$

$$L' = \rho V \Gamma \tag{2.3}$$

The spin rate is defined as the rotational velocity over the free stream velocity, see Equation 2.4. Though the spinning axis is missing from this equation, as pointed out by Jinji [38], this is still an important parameter. Especially in other researches as the spinning axis is assumed perpendicular on the lift and therefore relates linearly to the lift. As for windtunnel testing, the spinning of the smooth sphere is perpendicular to the flow velocity. Therefore it is sensible for many researches based on windtunnel testing to exclude the spinning axis influence.

$$S = \frac{V_{rot}}{V_{flow}} = \frac{\omega r}{V_{flow}} \tag{2.4}$$

Where S is the spin parameter [-], also known as the spin factor, V_{rot} is the rotational velocity [m/s], V_{flow} is the free stream velocity [m/s], ω is the angular velocity [1/s], r is the radius of the object [m]. $alpha$ is also in some literature used as spin parameter or spin factor.

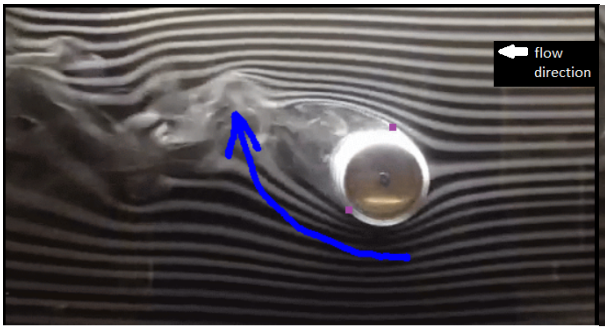

Figure 2.6: Smoke photograph of spinning sphere (clockwise). The air flows from right to left and due to the rotation the wake shift upwards, indicated by the blue arrow. The purple dots indicate the separation points [44]

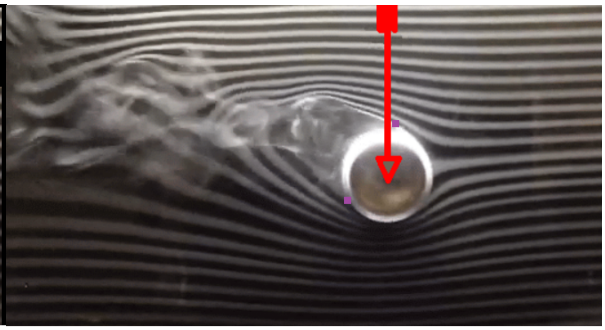

Figure 2.7: Due to the shifted wake upwards, the momentum will be balanced by a force on the sphere acting downwards. This is indicated by the red arrow. [44]

When the smooth sphere moves through the air, the sphere surface interacts with the boundary layer. Due to this interaction, the boundary layer separates from the sphere and creates a low pressured wake. However, if the ball spins, the boundary layer separation occurs at different locations. The spin delays separation on the retreating side and moves the separation point forward on the advancing side. On the advancing side the flow velocity is lower, generating a lower momentum for the boundary layer to counteract the pressure gradient and so the transition starts earlier and the separation point moves more upstream [44] [45]. On the retreating side the flow velocity will be higher and hence the separation point will move more aft. Combining both would deflect the wake, see Figure 2.6. This would result in an asymmetrical wake. This shifting of the wake would lead to a momentum. To balance that it would have to create a reaction momentum on the smooth sphere, see Figure 2.7. The Magnus effect is caused by wake contraction in one direction, leading to an opposite force on the sphere, see Figure 2.7. This is the Magnus force. The Magnus force is a combination of the static pressure, dynamic pressure and the boundary layer and therefore directly dependent on the velocity, density, angular velocity, smooth sphere surface and the surface roughness (= 0 for a smooth sphere) [6]. It was found that the Magnus effect is largest when the angular and translational velocity vectors are perpendicular, and minimal when the angle between the two vectors approached 0° [38]. The pressure difference between front and back leads to a force that is known and slows the smooth sphere down: drag [45].

Using the derived working of the Magnus force, it can be explained a sphere with backspin has a higher lift coefficient than one with topspin. For the lift of a sphere, due to the absence of geometrical and flow disturbances, the ball abides mostly by the Kutta-Joukowski equation, relating the lift linear to the circulation. The backspin will have a retreating rotation on the top and advancing on the bottom, generating a wake like Figure 2.8. The topspin will have opposite rotation, with a Magnus force pointing downwards. Hence, the sphere with topspin will be pushed more down and will cover a shorter distance before landing than one with backspin.

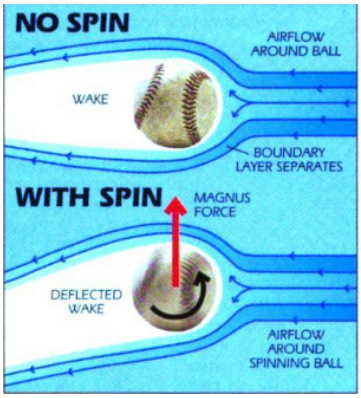

Figure 2.8: Wake contraction and reaction force, Magnus Effect [14]

The inverse Magnus effect occurs when the advancing side causes transition to turbulent of the boundary layer, whereas the retreating side has a laminar boundary layer. This would lead to a postponed flow separation on the advancing side and hence a force in opposite direction of the usual supposed Magnus effect, where the pressure on the advancing side would be higher due to earlier separation [45] [44] [40]. This transition point with separating, reconnecting and the separation bubble is a consequence of the critical Reynolds number and drag crisis. This causes a negative lift based on certain conditions, see Figure 2.9.

The lift coefficient tends to reach a maximum of 0.5, which was also found by Maccol [36].

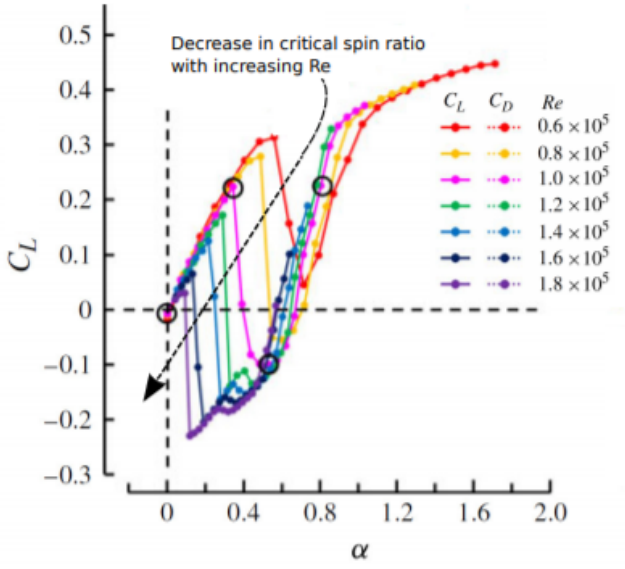

Figure 2.9: Smooth sphere: Lift coefficient for different spin factors (α, in this report given as S in Equation 2.4) and Reynolds numbers [20]

2.2. Flow around a baseball

The flow around a baseball differs in some areas with respect to the flow of a smooth sphere. The main difference between the baseball and sphere are the seams and different surface roughness. The seams can cause flow tripping, which makes the flow turbulent and can lead to more favourable characteristics, like prolonging the flow attachment. It can also cause flow separation. The flow tripping depends on conditions like geometry, surface roughness and the Reynolds number.

2.2.1. Seam effects

In most cases for professional baseball, the thrown velocities are quite high (between 120.7 and 169.1 km/h [31]). In combination with the relative low viscosity of air [51], this makes the Reynolds number quite high and the flow close to the ball turbulent.

Flow tripping happens when a small obtrusion is in the flow domain and the flow stumbles into it. Instead of remaining laminar or turbulent, this may cause the flow to ”trip” and become turbulent instead of laminar or may cause separation.

The seam height over the years fluctuates. This means that the aerodynamic behaviour also changes. The effect of the seam height is demonstrated in Figure 2.10. Here the ball is moving to the left at 90 mph and is not rotating. It can be seen that the 0.022” seams yield a smaller wake than the 0.045” seams. Therefore the pressure force behind the 0.022” is higher and hence the drag is smaller. The drag coefficient seams to be scaling linearly with the seam height, see Figure 2.11.

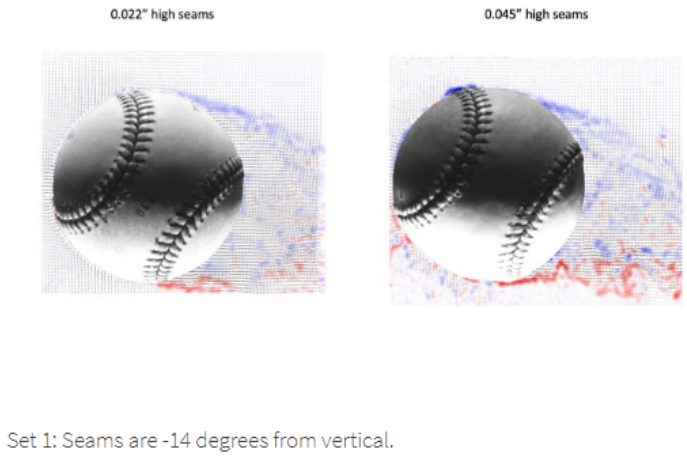

Figure 2.10: Seam height effect on wake baseball tilted at 14 degrees [13]

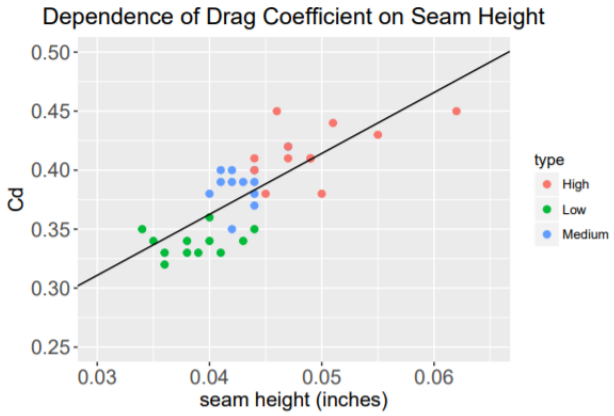

Figure 2.11: Drag coefficient vs Seam Height [24]

A difference in the wake can be observed when the baseball is rotated to -2.7°, see Figure 2.12. Here the 0.045” seam causes a boundary layer transition and flow separation, resulting in a higher drag. The 0.022” seams causes also a boundary layer transition, but more aft. This means the wake is still more contracted and the drag force hence is lower. For both cases the seam causes a shift in boundary layer behaviour, resulting in separation.

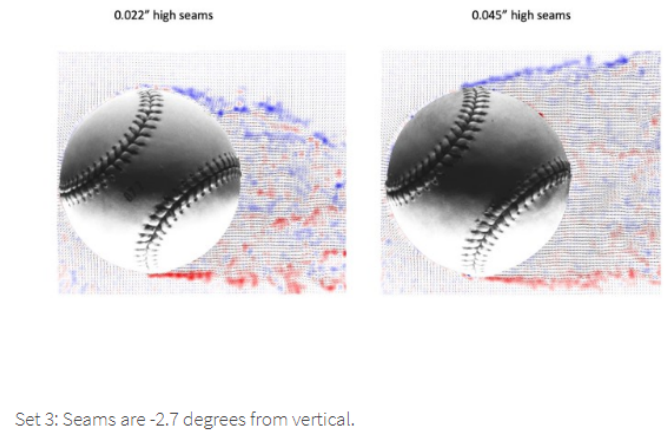

Figure 2.12: Seam height effect on wake baseball tilted at 2.7 degrees [13]

Authors like Kensrud [40] found a drag crisis for a baseball, but not in the same magnitude as a smooth sphere. It was also found that as the height of the seams increased, the drag also increased. The orientation and rotation of the ball reduces the drag crisis. In Figure 2.13 Kensrud observed a drag crisis after a Reynolds number of 160.000, decreasing the C_D to approximately 0.16.

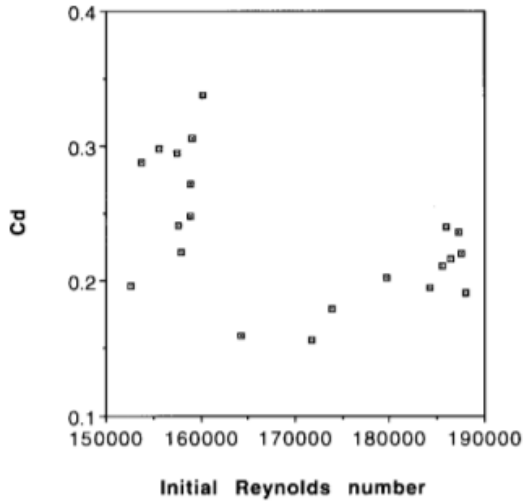

Figure 2.13: Drag crisis observed after 160,000 Re [40]

The baseball committee for the MLB found the same conclusion [24], but also noted that the MLB baseball is relatively smooth and therefore also resulting in the drag crisis. As for the case where lift and ball rotation are perpendicular, they found that lift is proportional to the spin parameter, which is the ratio of rotational speed over linear speed. As this changes, so does also the lift during the drag crisis, see Figure 2.14. Kensrud [40] found the same bilinear trend as Frohlich. For baseballs with larger seams, the lift and drag increases. [40]

However, various other researchers mentioned no detection of drag crisis for a baseball [22] [6] [46]. This is due to the fact that the disruptions on the baseballs, caused by the seams, are not as equally distanced as with the research with adjusted spheres or even the dimples on a golf ball [37]. Instead the seams (orientation and height) play a more asymmetric and less predictable influence on the boundary layer. This influences the Reynolds number and also can induce flow tripping. This affects the wake

behind the baseball and vice versa the wake affects the baseballs. Another factor is that as the spin parameter increases, the drag crisis decreases. As a third factor, Higuchi [34] noticed that for some researches the step size (in range of 5°) was too large to identify the drag crisis.

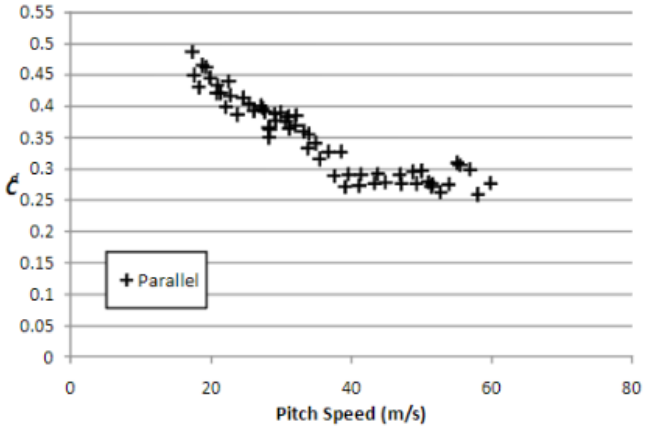

Figure 2.14: Drag coefficient non rotating major league baseball vs Velocity [37]

Often encountered in aircraft aerodynamics is the hysteresis effect. This effect is the cause that for certain locations the flow can differ, based on the history. For aircraft it is encountered in the stall regime. At a certain angle the flow detaches and going further the flow stays detached. However, moving to the point just before originally detaching, the flow will not attach again. Only moving back further, the flow attaches again with corresponding favourable aerodynamics. This is depicted in Figure 2.15. Here the blue line corresponds to increasing angle of attack. This means that the flow is attached until it separates. The green line corresponds to a decreasing angle of attack and hence separated flow until it attaches. The differences can be seen in the lift graph, where for the blue line the flow stays attached until 15° (hence higher $C_{L,MAX}$) and the green line only attaches itself again at 13°, with a lower $C_{L,MAX}$. The same can be observed for the drag coefficient, only the separated flow having a lower drag coefficient, due to the absence of separation bubbles.

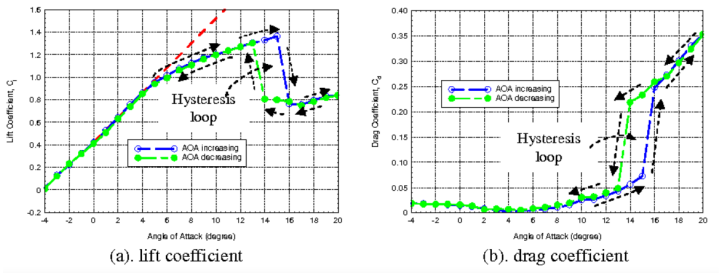

Figure 2.15: Lift and drag coefficients versus angle of attack. [26]

The hysteresis effect was also observed by Higuchi for baseballs [34]. When the ball moves to the left and rotates clockwise, the separation occuring on the top side moves downstream. For the lower side, the separation moves more upstream. The difference in separation points creates a side force. However, the side force varies, as can be seen in the force figure (Figure 2.16) and the wake plot (Figure 2.17).

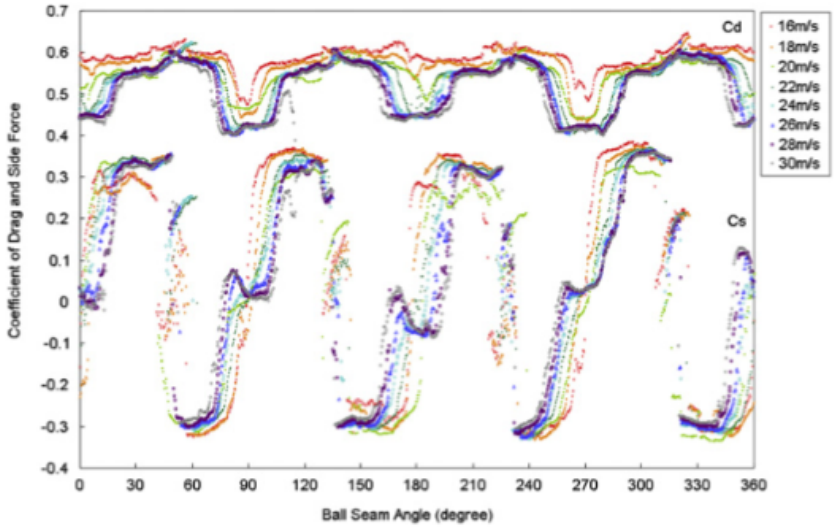

Figure 2.16: Side force versus baseball angle [34]

At 52°, the separation happens before the attached flow interacts with the seam on the upper side. Rotating the ball backwards the flow remains unattached until 30°. Near 60° the same hysteresis effect was found, but now for the lower side. This effect was found to be robust and largely invariant with time or upstream disruptions [34].

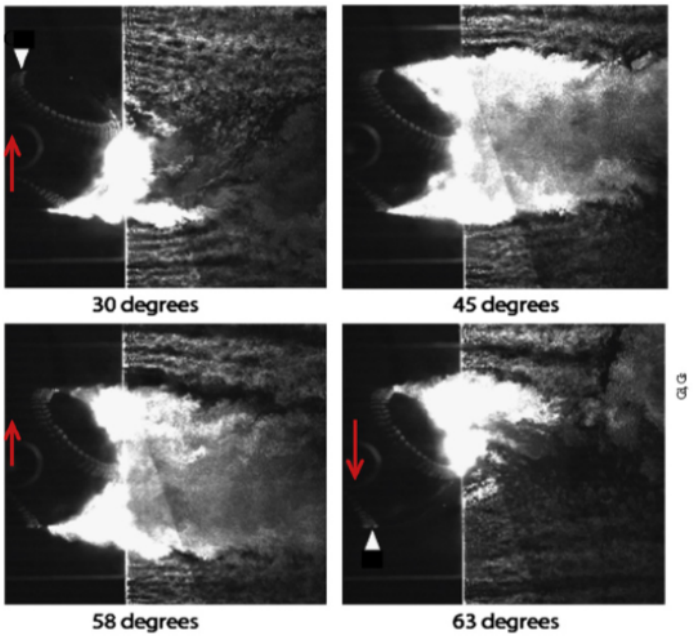

Figure 2.17: Wake baseball for 30, 45, 58 and 63 degrees [34]

2.2.2. The knuckle-ball

Interesting is the research done by Watts [54]. Here a knuckleball is researched, a ball with (almost) no rotation and hence an absence of the Magnus effect. Here the trajectory is hence dominated by the seam orientation and the effect on the boundary layer, introducing an asymmetric pressure and hence for the eye an irrational effect on the path.

As the ball is round, the force can be estimated as a periodic one:

$$F = F_0 sin(\omega t + \phi) \tag{2.5}$$

Where F_0 is a constant, ω is the natural period and ϕ is the phase. As F = m · a, the force introduces an acceleration. Integrating F/m twice hence yields a distance, the lateral deflection. Hence:

$$y = -\frac{F_0}{m}\frac{1}{\omega^2} sin(\omega t + \phi) \tag{2.6}$$

This yields an interesting fact, which also explains why seam orientation is so important at low spin rates. As omega is smaller, the lateral deflection (Equation 2.6) becomes bigger and also the spin rate decreases, which in fact makes the Magnus force smaller. The maximum value occurs when the sinus equals 0.5 π, hence a total rotation of 90 degrees over the distance would maximize the ”break” from the normal trajectory.

However, when a lateral force F_0 is instantly applied on a ball at rest, the equation becomes:

$$y(t) = \int_0^{+t} \int_0^{\tau} F(\lambda)\, d\lambda\, d\tau \tag{2.7}$$

If F is a constant and the traveling time is assumed as the total distance over the initial velocity (assuming velocity does not change much over the distance, which is a plausible assumption as the traveling time is short), this would yield:

$$Y = \frac{1}{2}\frac{F_0}{m}(\frac{D}{V})^2 \quad \text{[54]} \tag{2.8}$$

From Figure 2.18 it can be observed that the force F scales with the square root of the velocity. Combining this with the result from Equation 2.8, the lateral deflection is not dependent on the speed. Hence the lateral movement of the baseball depends solely on the small rotation earlier depicted in Equation 2.6 and the seam orientation which influences the boundary layer, which introduces an oscillating wake.

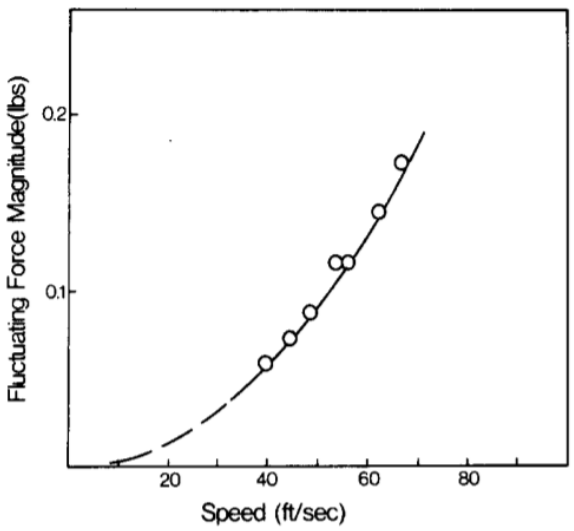

Figure 2.18: Lateral force versus the velocity [54]

The effect of the rotation on the ball on the lateral deflection can be seen in Figure 2.19, for a speed of 21 m/s [54].

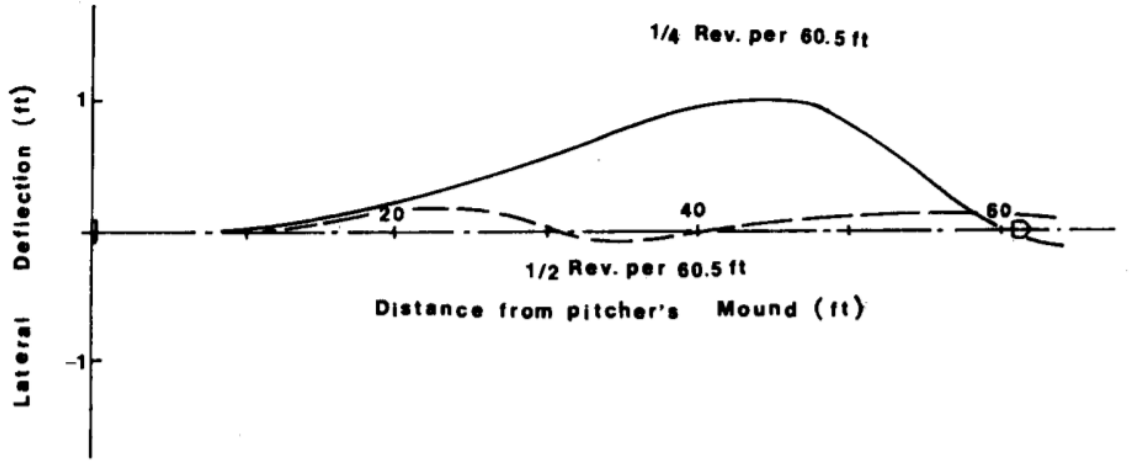

Figure 2.19: Rotational effect on the lateral displacement for 21 m/s [54]

Watts [54] places a final note, by relating the quantities to the curvature of the path:

$$k_{curv} = \frac{F_0}{m\,V^2} \tag{2.9}$$

Hence the curvature is constant for a constant force F_0. However, from the receiver point of view, the deflection is changing by the rate of acceleration from Equation 2.8. However, if the force is erratic (due to boundary layer separation, surface roughness of the seams or even the wind), this could even fluctuate more or less, making a prediction of the ball even more difficult for a batter.

Watts concluded that there are 2 possible mechanisms which could explain the erratic movement of the knuckleball. The first mechanism is a result from the seams being at the location where the boundary layer separates, resulting in a fluctuating lateral force. But the most likely explanation is that the ball spins slowly. This would change the location of the rough elements (strings and seams) and hence causing a non-symmetric velocity distribution with a shifting wake as an consequence.

2.3. Earlier performed experiments/theory

The difference for seam orientation seems to fade when the spin parameter increases. Alaways [6] found that when there was little spin, the lift and drag coefficient for the 2 and 4 seam configurations differed more, than at a higher spin rate. This leads to the believe that if the spin rate increases even more, eventually there will be no difference in drag an lift coefficient for a 2 and 4 seam. The results were bundled with results from other authors like Watts [53] and presented in Figure 2.20. These results also show why Watts [53] could not detect difference in lift coefficient for the 2 and 4 seam configurations.

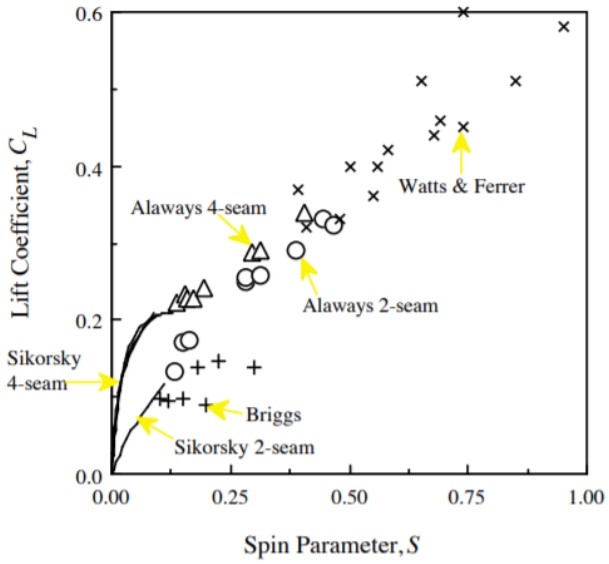

Figure 2.20: Lift coefficient versus Spin rate of baseballs [6]

All the effects previously described also influence the lift of the baseball. However, till now the relations were only qualitative. In this section some relations between the spin rate and lift coefficient will be derived and the dominating roles of the seam effect and the Magnus effect.

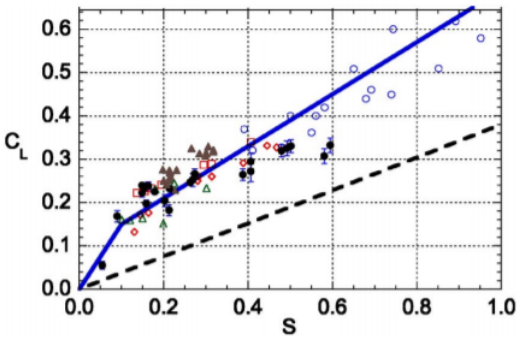

Figure 2.21: Cl vs Spin rate from different researches for baseballs [46]. The closed circles indicate the experiment performed by Nathan [46], while the open circles, open triangles, open diamonds and squares, closed triangles are from other experiments summarised by Nathan [46]. The dashed line shows a parametrization for the assumed Magnus force based on the difference in drag of the 2 sides of the ball due to rotation [46].

From Figure 2.21 it can be seen that the seam effect is the dominating factor for C_L for S < 0.1. However, for S > 0.2 the 4 and 2 seam are nearly on the same line and the Magnus effect is now the dominating force. The closed circles are from the Nathan [46], open circles are from Watts [53], open triangles are from Briggs [16], open diamonds and squares are from Alaways two- and four-seam [6], [7] and closed triangles are from the pitching machine data of Jinji [39]. To parametrize this behaviour, Sawicki [27] opted for the following Equation 2.10:

$$C_L = 1.5 \cdot S \quad for \quad S < 0.1, \tag{2.10}$$

$$C_L = 0.09 + 0.6 \cdot S \quad for \quad S > 0.1 \tag{2.11}$$

This parametrization is seen as the blue solid line in the figure. This equation predicts the behaviour

quite good, however it neglects the seam orientation, which play a big role when the spin factor is small. Also, only a few data points are chosen between an spin parameter of 0 and 0.1. Figure 2.22 gives a more clear overview and the difference between the 4 and 2 seam configuration for a low spin rate.

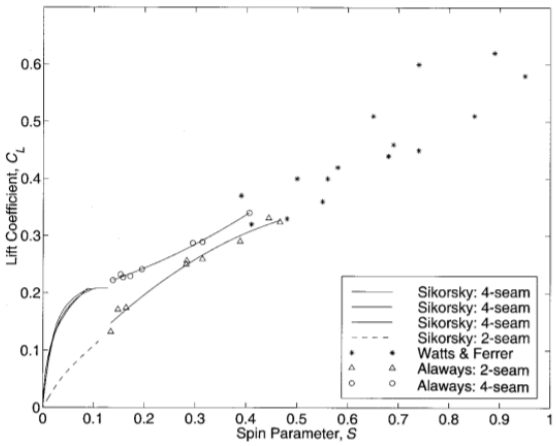

Figure 2.22: Cl vs low spinrate for 4 seam and 2 seam ball [8]

The experiment from Briggs [16] used a wrong lift correction and therefore the lift values should be increased by approximately 50%. This was done in Figure 2.21. After the correction, similar results were found by the strain gauges of Watts [53] in a windtunnel experiment, though the velocity was kept constant at 37 mph and hence only a (rough linear) relation between C_L and S could be found. Nathan [46] also found that the lift coefficient C_L was not dependent on the velocity, as seen in Figure 2.23. This contradicts Adair [4], whose conclusions were based on the erroneous data from Briggs.

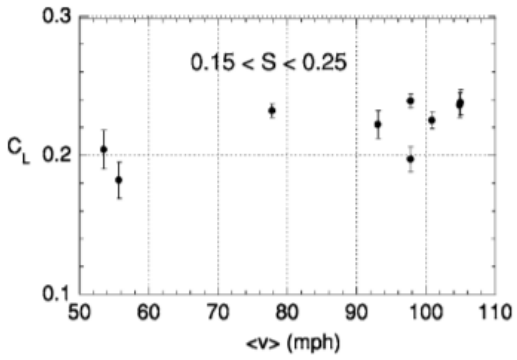

Figure 2.23: Cl vs Velocity [46]

Observed from Figure 2.22, C_L of the 4 and 2 seam seem to converge for higher spin rates and is verified with multiple experiments.

Important to notice is that the results in this section all have assumed perpendicular axis between the velocity vector and the angular velocity vector. Jinji [38] proved that if this is not the case, the vertical component in the direction of the velocity vector should be used. This correction can be done by taking multiplying the velocity vector with the sinus of the angle between the 2 planes. This corresponds to the Kutta-Joukowski theorem as earlier described.

Also Figures 2.22 and 2.20 show that for a low spin parameter, the difference in C_L between a 4-seam

and 2-seam is quite big, indicating that something extra happens here with the combination of rotation and the seams locations.

3

Particle Image Velocimetry

Particle Image Velocimetry will be used to visualize the flow in the wake of the baseball. In this chapter PIV and the basic principles will be introduced shortly in 3.1 and in the Section 3.2 the processing of the data into a flow field will be discussed.

3.1. Principles

PIV is a non-intrusive measurement method, which means that the flow is not altered by the measurement equipment (in contrast to for example a hot wire anemometer). By tracking tracing particles and processing the traveled distance and time, an instantaneous velocity field can be created. It only requires optical access so the laser can enlighten the particles and the camera which must have a clear line of sight for the measurement plane, see Figure 3.1. PIV is accepted as the most modern and advanced measurement technique for fluid mechanics research. However, processing the PIV data is often time consuming and expensive, as the storage of images can contain up to several gigabytes and the image processing takes hours or days before statistical information on the flow is obtained [25] [49].

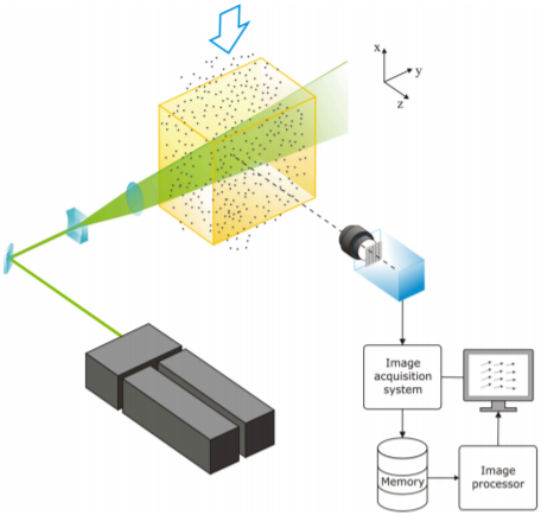

Figure 3.1: Schematic of a typical planar PIV measurement system [49]

3.1.1. Seeding/Tracer Particles

Microscopic particles are injected in the flow and distributed randomly. They are convected along the fluid. These particles must follow the flow, as these particles are used to deduce the flow qualities. The amount of particles introduced in the flow are so that is considered not affecting the flow properties

and hence non-intrusive. The seeding tracers concentration C usually is in the range of 10^9 and 10^{12} particles/m^3. Exceeding this effect, the particles tracers have an influence on the flow properties, also known as multi-phase flow effects. It is related to the mass ratio and should be smaller than 0.1%.

For proper seeding 4 factors are key:

1. The tracer particles must follow the flow.
2. The concentration must be enough to visualize the whole flow field
3. The concentration must not be superfluous to temper with the flow characteristics
4. The light scattering must be sufficient to be traced accordingly

For the scatter the main parameters are the diameter of the particle and the index of refraction relative to the fluid medium. These parameters conflict with each other, so an efficient trade-off must be made. [49]

The quasi viscous term, also known as Stokes drag, dominates the particle dynamics if the tracers are sufficient small. The difference between the velocity of the particle and the flow field is given in Equation 3.1 [25].

$$V - U = \frac{2}{9}\frac{a^2(\rho_p - \rho_f)}{\mu}\frac{dV}{dt} \tag{3.1}$$

Here V is the particle velocity, U is the flow velocity, a is the radius of the flow particle, ρ_p is the density of the flow particle, ρ_f the density of the flow and μ is the dynamic viscosity.

The term $V - U$ is the slip velocity. Observed from Equation 3.1 is that if the density of tracer is equal to the density of the flow, there is no offset. If the density of the particle corresponds closely to the flow that $\frac{\rho_p - \rho_f}{\rho_f} \ll 1$, the particle is neutrally buoyant. If not, there is a discrepancy, which can be observed in Figure 3.2 [25] [49].

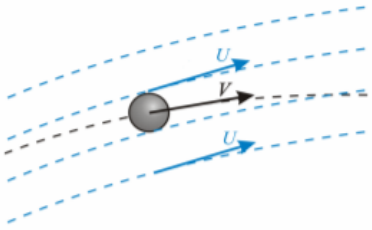

Figure 3.2: Difference particle and surrounding fluid velocity [49]

The particles in the flow must scatter enough light to be detected by the camera. However, this requirement contradicts the flow following requirement. Usually particle dimensions are in the order of a micrometer for gas (air) and tens of micrometers for liquids [49].

The scattering efficiency is described by the scattering cross section. This depends on 3 factors, namely the ration of refractive index, the wavelength of the light and the diameter of the particle. Mie scattering theory is valid if the particles diameters d_P is larger then wavelength of the incident light. The formula describes the scattering of particles as a function the diameter and the wavelength, see Equation 3.2 [49]. Here q is the normalized diameter.

$$q = \frac{\pi d_p}{\lambda} \tag{3.2}$$

If q exceeds 1, approximately q local maxima appear in the angular distribution in the range of 0° to 180°, see Figure 3.3. If q increases, the ratio of forward to backward scatter will increase by a higher rate [49]. Therefore recording the forward scatter seems the most logical step. However, with a limited depth of field and also limited optical access, usually the camera records from the side, at an angle of 90°. Here the minimum scattered light intensity is measured, as also seen in Figure 3.3.

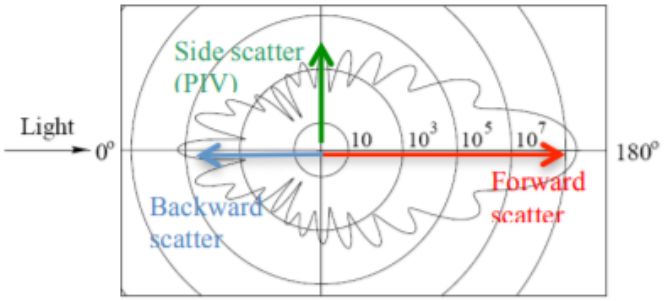

Figure 3.3: Light Scatter [49]

3.1.2. Imaging

The magnification of the camera is defined by Equation 3.3 [49].

$$M = \frac{z_0}{Z_0} \tag{3.3}$$

Where M is the magnification factor, z_0 is image distance and Z_0 is the object distance as depicted in Figure 3.4 [25].

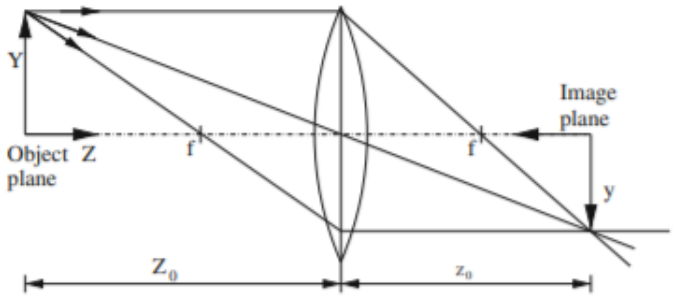

Figure 3.4: Reconstruction of a geometric image [25]

With also the focal length (f) known, the object distance can be determined [49].

$$\frac{1}{f} = \frac{1}{Z_0} + \frac{1}{z_0} \tag{3.4}$$

The intensity distribution on the image plane by the particles is captured by the CCD sensors of the camera. The particle image diameter is the Euclidean sum of the diffraction and the geometrical image diameter [49], see Equation 3.5.

$$d_\tau = \sqrt{d_{geom}^2 + d_{diff}^2} \tag{3.5}$$

The geometrical diameter is determined by the diameter of the particle times the magnification factor, see Equation 3.6.

$$d_{geom} = d_p M \tag{3.6}$$

The diffraction diameter is given by Equation 3.7 and is the Fraunhofer diffraction. This is the diffraction of light when a point light source, such as the light scatter of a particle, passes a circular aperture (lens) [50]. For PIV the geometric image diameter is small in comparison to the diffraction term and hence the geometric image diameter is neglected. If the size of the diffraction-limited particle image is too small, it moves within the same pixels and the velocity cannot be extrapolated accurately, see Figure 3.5. This is known as peaklocking. This should be prevented and therefore d_τ should be around 2-4 pixels [50].

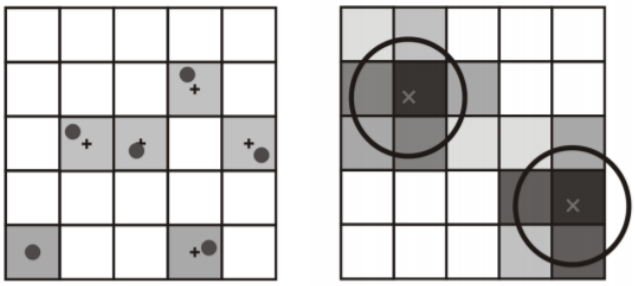

Figure 3.5: Left: Particle position not detected with sub-pixel accuracy, leading to positional errors. Referred as Peak locking. Right: The particle image position can be reconstructed by interpolating the light intensity distribution over several pixels [49]

For the measurement within the entire depth of the laser sheet, the depth-of-field Δz thickness should be equal to or more than the laser sheet [50] [49]. The depth-of-field is determined by Equation 3.8.

$$d_{diff} = 2.44\lambda(1 + M)f_\# \tag{3.7}$$

$$\delta_z = 4.88\frac{M + 1}{M}^2 f_\#^2 \lambda \tag{3.8}$$

3.1.3. Light Source

PIV measurements detect particle motion for a finite observation time. This observation time is the separation time between the light pulses, Δt. The particles have to be illuminated twice and observed within this separation time. The light pulse should be short, so particle images appear as circular dots and not streaks. This happens if the particle displacement within the separation time is significantly smaller than the particle image [49], see Equation 3.9.

$$\delta t << \frac{d_\tau}{VM} \tag{3.9}$$

Here δt is the pulse duration, d_τ is the diameter of the particle image, V is the velocity and M is the image magnification.

Also, the particles lying within a thin sheet are required to be illuminated so that they all can be sharply recorded. As a third requirement, the light intensity of the source must be such that the scattered light of the seeding particles are detected by the imaging devices. Energy pulse E is proportional to the linear dimension L of the investigated area. Typically E around 100 mJ gives enough light to illuminate a 10 by 10 cm area in air and twice for water [49].

Lasers are used, since they produce a pulsed, collimated, monochromatic light beam. This is easily shaped into a thin light sheet with the help of mirrors and lenses. Most common device for PIV experiments is the solid state frequency-doubled neodymium-doped yttrium aluminium garnet laser (Nd:YAG). This emits light with a wavelength of 532 nm. The pulse duration is very short (between 5 ns and 10 ns). It illuminates seeded flows instantly without limiting the flow speed. Nd:YLF lasers are generally used for high-speed applications. They operate between 1 and 5 kHz with a wavelength of 527 nm [49] [50].

3.1.4. PIV variants

The most simple PIV set-up is a 2D system. Here a laser forms a thin light sheet, which light up tracer particles in the flow and and with the 2 images shortly taken after each other, the displacement can be calculated and the local velocity is determined from the travelled distance and the time interval. In 2D PIV only 1 camera is used to measure the 2 in-plane velocity components (2C). By adding a second camera, stereo-piv is introduced. This allows to observe the true velocity vector by viewing another angle. The two 2C displacement vectors from both cameras are combined. This gives the third component of the velocity vector (out-of-plane), with the help of some geometrical reconstruction. Notice that although all 3 velocity components are determined in a plane, still the view is limited to a plane in the flow field. An useful extension is the use of time-resolved PIV. Here continuously images are recorded with a sufficient frame rate in order to observe the dynamical evolution of the flow.This allows to also determine the average velocity profile next to the instantaneous structures of the turbulent boundary layer in a plane [25] [56]. The experimental set-up for planar PIV an stereo-PIV is shown in Figure 3.6, as well as the tomographic PIV set-up discussed below the figure.

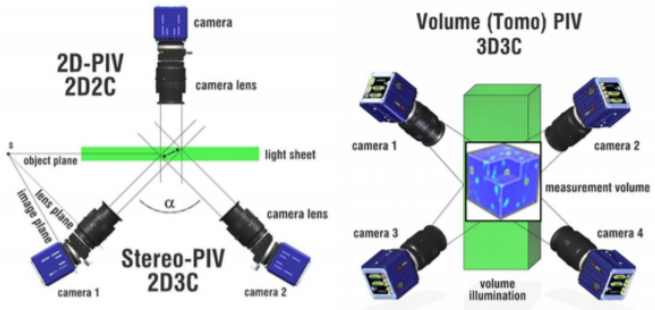

Figure 3.6: Experimental setup for planar PIV (2D2C), Stereo-PIV (2D3C) and volumetric tomographic PIV (3D3C) [56]

The next step is using PIV in a full volume and to see the instantaneous structures inside the turbulent boundary layer. This is done by simultaneously recording the reflection of the particles by capturing the images with typically 3 or 4 cameras with different viewing directions. The location of the particles are first determined in 2D, with the help of peak fit (e.g. Gaussian, see 3.2). With a triangulation procedure, the particle images are matched from different cameras, resulting into possible 3D-particle positions. The last step is to track the 3D positions in time and space by computing particle velocities and Lagrangian trajectories. Due to overlapping particles and ghost particles, the approach is usually limited to low seeding densities (500-5000 particles per megapixel sensor). In order to have a denser volumetric flow field, tomographic PIV was developed by Elsinga et al. [23]. This uses an iterative reconstruction technique to have a much higher seeding density. Finally a 3D cross-correlation method is used on the local interrogation volumes to compute the 3 dimensions, 3 component flow field: 3D3C. [56] [25]

3.2. Flowfield determination

The procedure to construct a motion field of the tracing particles is given by:

1. Image Windowing
2. Cross-correlation analysis
3. Correlation peak sub-pixel interpolation
4. Time and scaling

The procedure is illustrated in Figure 3.7. The interrogation window is the subdivision of the images into smaller areas. Each area will be processed to calculate one vector. Determining which particle from frame 1 is the same particle in frame 2 is done by a cross-correlation using Fast-Fourier Transforms. This procedure computes the peak, which is the probability for the displacement value. Due to the use of the interrogation windows, sub-pixel calculations can find the velocity from the cross-correlation, resulting in a velocity vector. Additional calculations and post-processing can be used on the whole field to reduce noise [19]. This whole procedure is carried out by the program DAVIS 8 by Lavision ©

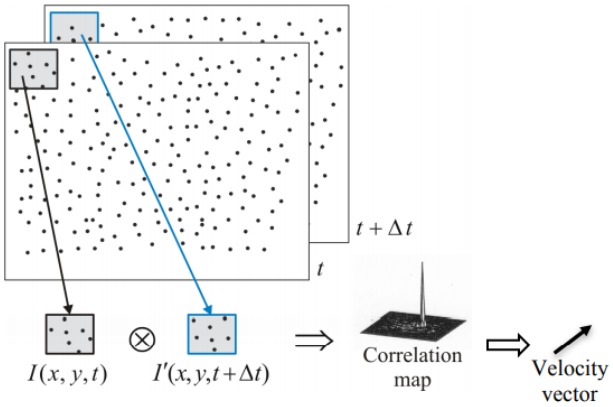

Figure 3.7: Flowfield determination procedure [49]

3.2.1. Interrogation window

The size of the interrogation window defines the spatial resolution of the enclosed velocity profile. The interrogation size must be small enough (> 10), such that the effects of the velocity gradients in a sufficient seeded flow are minimal. Using a large interrogation volume usually leads to an underestimation of the root-mean-square or the dissipation rate. Normal interrogation windows are in the range from 16x16 to 128x128 pixels [25].

The spatial resolution in the velocity field determines the obtainable spatial resolution of the differential estimation. Using a differentiation scheme the spatial resolution reduces due to smoothing effects. The effect of the size of the interrogation window on the velocity and vorticity is shown in Figure 3.8. [25] [57].

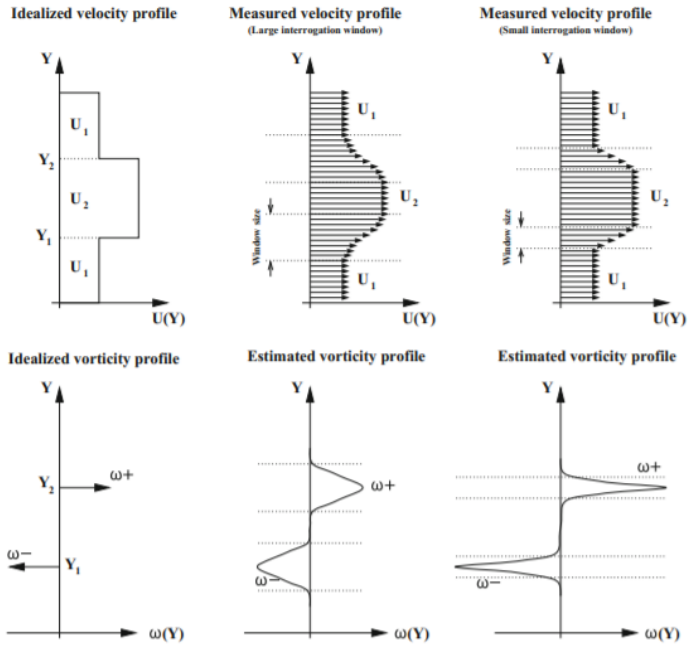

Figure 3.8: Effect of spatial resolution on vorticity estimation [25]

The total amount of velocity vectors is also determined by the interrogation window. This also influences the maximum spatial resolution of the velocity map. Raffel [25] indicates that typical values from 16x16 tot 128x128 pixels are used. Smaller interrogation windows lead to to a smaller measurement area to be used. The small sampling area decreases the amount of cross-correlated particle images and also decrease the cross-correlation peak and data yield. Using a large interrogation window leads to a higher cross-correlation value, but also results in a poorer spatial resolution in the larger measurement area[57]. The situation is demonstrated in Figure 3.9, where the interaction between in-cylinder turbulent flow field and flame propagation is investigated inside a single-cylinder optical gasoline engine operated at 1200 rpm. The interrogation area 16x16 has more than 12% incorrect vectors, originating near the piston. Using a grid of 32x32 or 64x64 gives roughly 95% correct vectors [43].

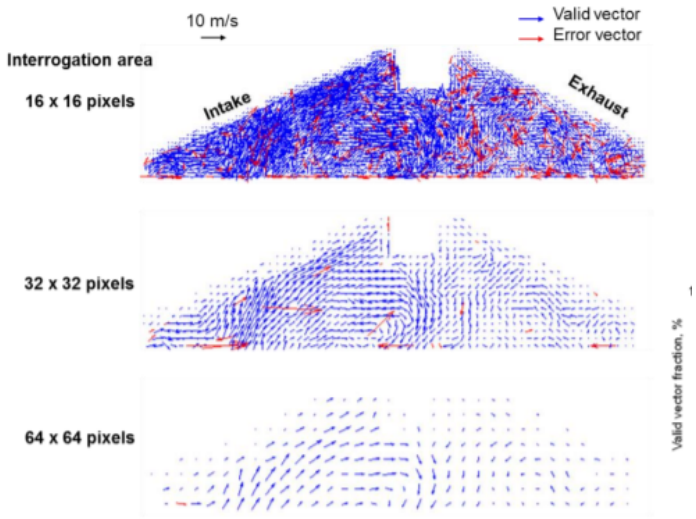

Figure 3.9: Processing of flow-fields with different interrogation areas: 16x16, 32x32 and 64x64 [43]

Using an overlap in the interrogation window between 2 frames, the data can be made more smooth

and to reduce the spacing between vectors in the resulting vector grid [21]. Important is to have a large enough window size to contain a sufficient amount of particles, to produce reliable vectors [30]. The optimum overlap percentage is based on the time delay between laser pulses and the minimum allowable dynamics spatial and velocity ranges [57].

Sub-pixel resolution errors can occur due to the particle image size, size of the interrogation window, local velocity gradient, particle density of the interrogation window, the performance of the instrument recording and digitizing the images, the quantisation effects (the light measurement resolution of the pixels, measured in bits per pixel) and computational errors like truncation errors. Westerweel ([55]) showed that displacement measurement errors can be underestimated, due to an incorrect probability density function for the image intensity. He found a match between his theoretical analysis and the Gaussian light-sheet and seeding [57].

3.2.2. Cross-correlation analysis and peak interpolation

The most suited peak finding technique is the cross-correlation. This uses 2 frames and uses the known sequence of the images to determine the direction of the particles. The cross-correlation analysis is performed by using a statistical tracking operator. This calculates the discrete cross-correlation map. The peaks show the average particle images displacement The highest peak is chosen from the the correlation map. This resembles the particles motion. The position is found by the closest integer pixel shift. Cross-correlation is advantageous when having a high signal to noise ratio. The accuracy can be expected to be approximate 0.05 - 0.1 pixel. Using the pixel size and the magnification factor, this accuracy can be converted into a real scale [19] [25]. A suitable method is to fit the correlation data to a function, specifically a Gaussian peak fit due to the behaviour of the particles. Using only three adjoining values, the component of the displacement can be estimated to find the correlation peaks [25].

3.2.3. Time and scaling

Dividing the gathered result by the time separation of the laser pulses, multiplying the pixel distance by the size of the pixels and dividing over the image magnification gives the corresponding flow field. The displacement of the particles over time delay between laser light pulses equals the local fluid velocity. Typically the velocity field of a PIV analysis have 10^4 vectors per image. The measurement accuracy is approximately 2%, depending of the digital image format and the interrogation resolution [49].

3.2.4. Reflections

PIV images three main components can be distinguished: Reflections from seed particles, the background and the background noise (reflections). This is seen in Figure 3.10, where the flow field of a model for a high lift airfoil is shown. [15]. Often images are affected due to unwanted light reflections which occur when the laser light reflects off a solid surface. The reflection's intensity can be a magnitude larger than the particles in the image. This causes a high auto-correlation peak. This peak can be larger than the other cross-correlation peak, hence interfering with the accurate determination of the flow velocity [5]. Therefore, a high quality image will have a high contrasts between the reflections of the particles and the background and background noise. The contrast between the intensities is show in the signal to noise ratio [15].

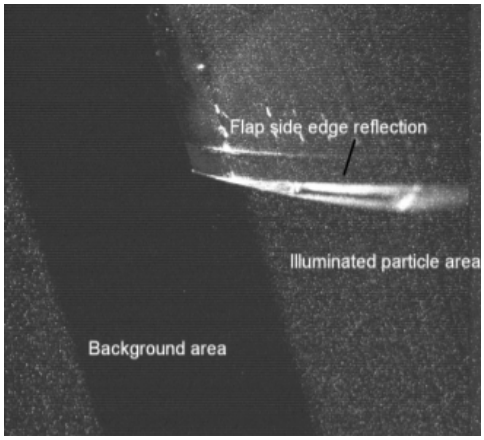

Figure 3.10: High lift airfoil with identified particles, background and reflections [15]

3.2.5. Instantaneous and time-averaged flow fields

In low, steady Reynolds number flows with no abrupt geometry changes, the flow is generally laminar and either steady or periodic. Therefore instantaneous flow information will be similar to the time-averaged flow data. But with different flow structures due to higher Reynolds numbers resulting in unsteady behaviour, the instantaneous flow data is useful [18]. To understand the behaviour of the flow, the instantaneous velocity data is important. Here the different element of some unsteady behaviour can be seen over time. Using these different images over time and taking the average would give the time-average velocity field. This can be used to understand the mean effect of the flow, although this would leave out some important flow details. Another interesting statistical value is the root mean square velocity. This gives extra information how the flow is differing over time [11].

4

Experimental set-up

In this chapter the set-up of the experiment is discussed, as well as data acquisition procedure and the data processing. In section 4.1 the experiment is discussed and in section 4.2 the data acquisition and processing.

4.1. Setup Planar PIV

In this section the description for the used experimental apparatus is discussed. The experiment is performed in the W-tunnel of the Aerodynamics Laboratories of TU Delft. Figure 4.1a shows the picture of the set-up, while in Figure 4.1b the schematic of the experimental set-up is given. The laser sheet is aimed over the centerline of the baseball, parallel to the flow direction. This allows to visualize the particles over the centre of the baseball for multiple configurations.

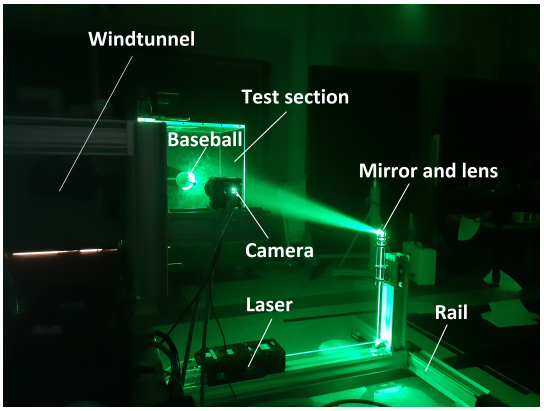

(a) The experimental set-up

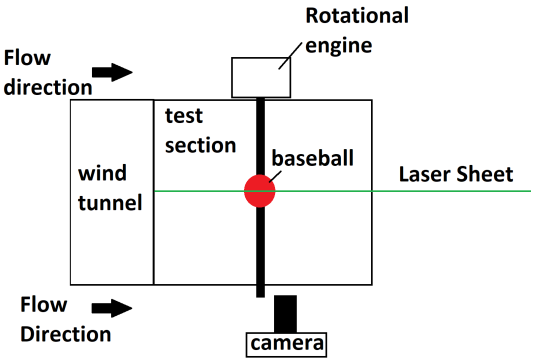

(b) Topview schematic

Figure 4.1: Experiment Set-up and schematic drawing

4.1.1. Windtunnel

The experiment is conducted in the windtunnel in the the W-tunnel of the Aerodynamics Laboratories of TU Delft, see Figure 4.2. The W-tunnel is an open jet windtunnel, where velocities up to 35 m/s can be achieved. It is regulated by controlling the RPM of the centrifugal fan, see Figure 4.3. The minimum achievable turbulence level is in the order of 0.5%, but is dependent on the flow velocity. The outlet is a square area of 0.4x0.4 m^2 [12].

Due to the velocity limitation of the windtunnel, the testing velocity was set at 30 m/s, relating to a Reynolds number of circa 150,000. This would relate to a subcritical or transcritical flow for a smooth

Figure 4.2: The windtunnel

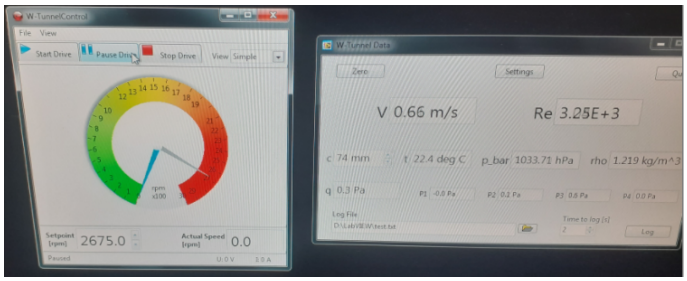

Figure 4.3: The controller of the windtunnel

sphere. The test section consists of 4 plexiglass walls, creating a 40x40 cm^2 inner region, while the walls are 1 cm thick. The size of the inner region is chosen such that it fits the exit of the windtunnel, hence not needing an additional nozzle or diffuser. The test section area is significantly bigger than the baseball area (40x40 cm^2 vs baseball diameter 7.3-7.5 cm, which relates the area to 1600 cm^2 versus 41.8 cm^2), which make the effects of blockage negligible (< 3%).

The configurations that are tested are the smooth sphere for comparison and to validate the expected results and the 2-seam and 4-seam configuration, see Chapter 1 for the orientation. The local seam effects without rotation are investigated to determine the flow effects with respect to flow tripping, wake deflection and size of the wake. The smooth sphere, 2-seam and 4 seam are also tested with a small spin parameter (S < 0.2), to investigate why the difference in lift coefficient occurs by researching the wake. The windtunnel velocity was set at 30 m/s. For non-rotating tests, the configurations are measured at specific angles. The 2 seam configuration has a symmetry axis about 180°, therefore the 180 domain is tested by steps of 5°. For the 4 seam configuration, the symmetry axis is seen every 90°, here also steps of 5° are used. The baseball has a circumference of 22.86 cm and a weight of 0.14 Kg and is the official baseball, which is used by the Dutch national team. For the rotating tests the baseball was varied between 300 and 1800 RPM, resulting in a spin parameter between 0 and 0.23 (see Equation 2.4)

4.1.2. Baseball mount

Inside the test section, the baseball is mounted on a horizontally-placed rod, going through the horizontal plexiglass plates, see Figure 4.4. This horizontal rod can be rotated by engine with an almost steady RPM or be mounted under a certain angle, see Figure 4.5. This allows for quick and efficient testing of static angles, as well as the relative easiness of mounting a rotational engine on the rod. The RPM of the engine is controlled with a voltage and current generator and is read out with a digital tachometer, see Figure 4.6a and the specifications in Figure 4.6b.

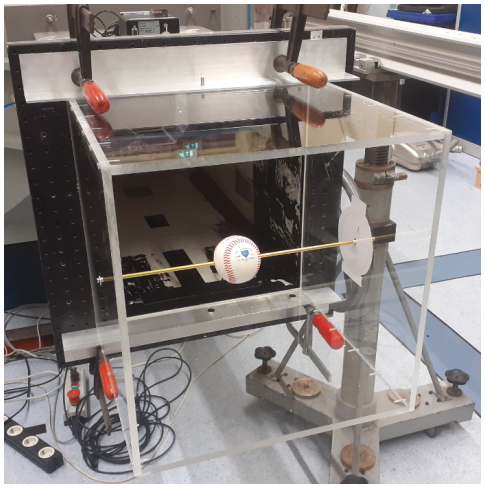

Figure 4.4: Test section

Figure 4.5: The angular control for the baseball

(a) HBM Digital Tachometer with Laser [33]

Technical data of the HBM Digital Tachometer With Laser.

Range	2.5~99999RPM.
Hz	From 0.05 to 1666 Hz.
Gladly	From 1 to 99999 Count.
Resolution	0.1RPM (2.5~999.9RPM)
1 RPM	(above 1000 RPM)
0.01Hz	(0.05 ~ 99.99Hz)
0.1Hz	(above 100Hz)
Accuracy	± (0.05% + 1digital)
Sampling Time	0.8 seconds (more than 60 RPM)
Select range	Auto range.
Time base	6MHz Quartz Crystal
Detect Distance	50mm - 500mm.
Size	155 x 70 x 35mm.

(b) Specifications HBM Digital Tachometer with Laser[33]

Figure 4.6: HBM digital tachometer device and specifications

4.1.3. Seeding device

Inside the windtunnel is a seeding device (Figure 4.7), which allows the release of the tracer particles. The particles can be filtered out of the air with an external ventilation system.

Figure 4.7: Seeding Device

4.1.4. Laser and mirror positioning

The laser chosen to light the particles up for tracking purposes is the Evergreen Nd:YAG in the first experiment. Due to the unavailability of the Evergreen laser in the second experiment, a spectra physics laser was used. This laser has a lower frequency (10 Hz) than the Evergreen and the intensity of the laser is higher.

The Evergreen laser is a dual pulsed laser for PIV applications with a 200 mJ pulse at 15 Hz. The system has a single laser head with a single power supply. It delivers a combination of precisely overlapping beams (532 nm). [17]

The laser is mounted on a rail, constructed with aluminum beams. This ensures the stability and also makes it easier to align the laser with the baseball centre. The laser is placed beneath the test section and the laser beam is reflected via a mirror upwards and via another mirror into the test section. The resulting laser beam is then diverged through a lens, such that the laser sheet lights up the particles inside the control volume.

As the light source was located below the baseball, particles further upstream under the center line of the baseball were observed than above. Therefore separation angles are limited to approximately 90° and higher on the top side and on the bottom side to approximately -80° and lower.

The laser sheet is also observed when looking into the test-section, see Figure 4.8. Hereby the horizontal light beam is the rod holding the baseball, where the vertical beam of light is the laser sheet.

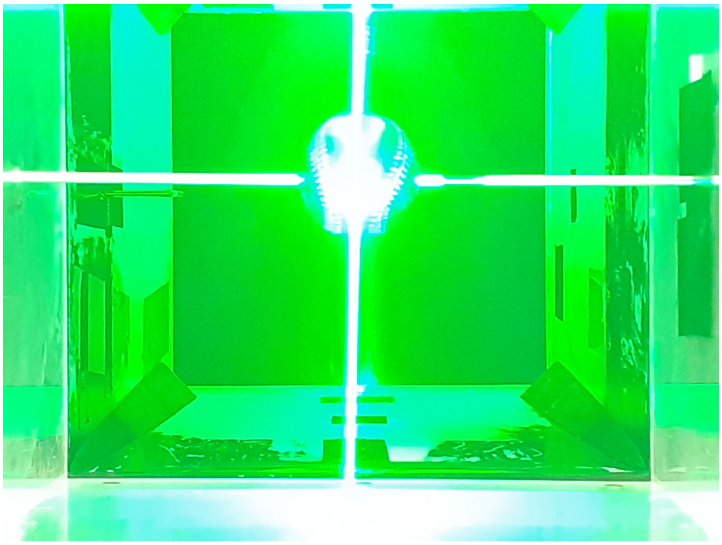

Figure 4.8: The laser sheet directed vertically at the centre of baseball. The horizontal green bar of light is the support (rod) of the baseball, which lights up due to the laser

4.1.5. Camera position

Most advanced and suitable cameras for PIV measurements have CMOS (sCMOS) sensors. Before the sCMOS cameras, the best digital high-speed cameras could only capture 500 frames per second within 256x256 pixels. Modern sCmos cameras are capable of frame rates above 20 kHz with an one mega pixel sensor [56]. The low light imaging and the large signal variation, high temporal and spatial resolution over large field of views make it useful for PIV applications. [41]. The CMOS sensors use active pixel sensor (APS) in which a photo-diode creates an electronic charge by converting light and an amplifier is embedded in each pixel, which can be read. Using the photo-diode, this will convert the stored charge into a voltage. This is amplified inside the pixel and is processed in sequential rows and columns along further signal processing circuits. Using a parallel structure, the CMOS sensor can use more channels with respect to a charge coupled device. Usually high-speed PIV sCMOS cameras have 32 or more output channels. While saturation effects might occur, the high pixel intensities are not influencing the image with respect to blooming in charge coupled device [49]. Blooming is the effect when a charge developed on a pixel leaks into nearby pixels and corrupts the scene [9].

The camera used has a double shutter for two images with 120 ns interframing time. The exposure time can be varied between 15 µs and 100 ms. The number of pixels are 2560 x 2160, with a pixel size of 6.5 µm x 6.5 µm. The active area covers 16.6 mm x 14.0 mm, with a spectral range from 370 to 1100 nm. The quantum efficiency. The frame rate is 50 fps. The highest resolution frame rate for 2560 x 2160 oixels is 50 fps. The camera dimensions are 103 mm x 80 mm x 86 mm and it weighs 700 g. [41]

The sCMOS camera (Figure 4.9) is positioned at the side. It is linked with the Programmable Timing Unit (PTU) and the computer, to synchronize the taking of pictures with the firing of the laser. The field of view is shown in Figure 4.10. The field of view is ca. 95mm by 115mm, having a magnification factor of 0.15. Due to the frequency of the laser, the frame rate is set at 15 Hz. The dt is 13 microseconds.

Figure 4.9: sCMOS Camera by Lavision ©

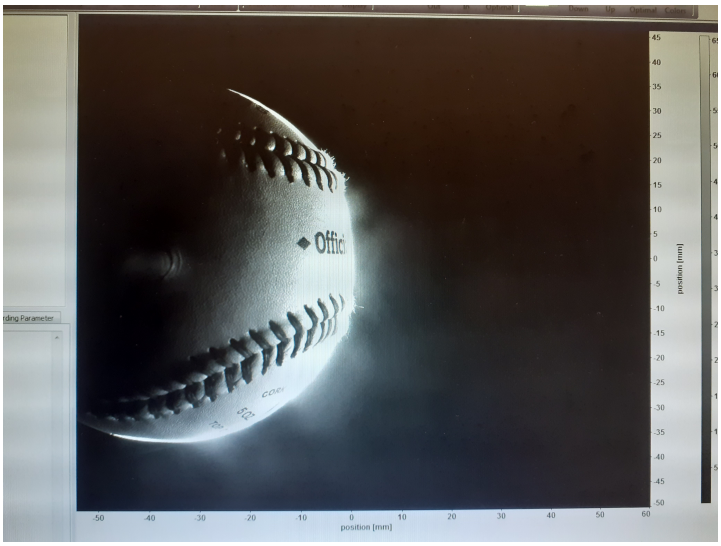

Figure 4.10: Field of view. The dimension is ca. 95mm by 115mm resulting in a magnification factor of 0.15

4.2. Processing planar PIV

In this section the data processing of the experiment is explained. First the processing in Davis is explained, where the data from raw images is processed into a velocity field. In the python code this data is analysed to determine the separation position and angles of the flow, as well as the size and centre of gravity (c.o.g.) of the recirculation area.

4.2.1. Processing in Davis

The first step on the PIV data is to apply the time-filter. Here for each pixel the minimum amount of light intensity is found over a temporal kernel of all successive snapshots. This minimum will be subtracted for every image. This would filter the static background noise due to other lighting effects and would yield solely the enlighted particles and the background noise due to more dynamic effects, like reflections. The next step is to process the images with the particles. This is done first by setting a mask. This allows to add an area in the frame, where no particles are expected. Then a multipass image windowing procedure is used. Starting from a double pass 64x64 window and decreasing it to 32x32 double pass with 75% overlap, a dense vector field is found with sufficient precision. As stated earlier about the camera, it contains 2560 by 2160 pixels, with a pixel size of 6.5 µm x 6.5 µm. Also a

filtering operation is applied, where the median filters strongly removes outliers and iteratively replaces them. The final step is to also add some statistical data. From the instantaneous flow fields the mean velocity field is determined, as well as the Root Mean Square of the velocity field and the Reynolds stress

4.2.2. Processing by Python

The flowfields computed by Davis are used an the input for the Python code. Here both instantaneous and time-averaged results are investigated further, by analysing the separation position, as well as the separation angles. Also the wake is analysed by investigating the recirculation area and centre of gravity.

For the experiment, the image of the smooth sphere is mirrored with respect to the horizontal line through the smooth sphere center. This is done as the baseball rotated in opposite direction as the smooth sphere. By mirroring the image, the smooth sphere and baseball rotate in the same direction. Due to this correction, the bottom separation angle can be observed up to -90°, while the top separation angle can be observed up to 80°

The separation position on the upper side and the lower side of the baseball are observed in Figure 4.11. To quantify this, the separation position is the position on the baseball where the horizontal velocity u becomes 0 for the first time. From this position also the angle is computed with respect to the geometrical centre of the baseball.

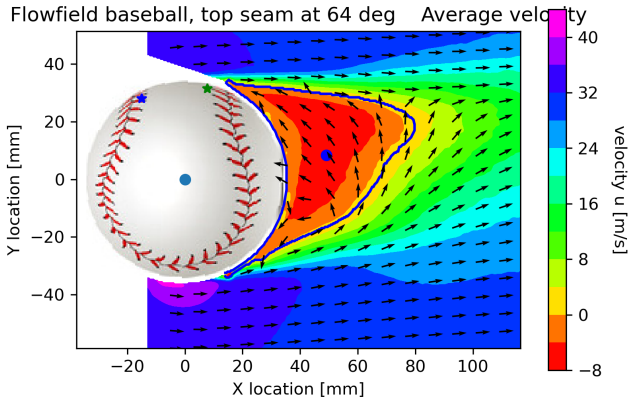

Figure 4.11: Time-averaged flow field baseball, 2-seam configuration with seam at 23 degrees. Notice that 86400 vectors are computed, but in the figure this is reduced to 288 vectors. In the computations the full field is considered. The flow field is the horizontal component of the velocity. The blue dot inside the baseball corresponds to its geographical center. The blue dot inside the flow field corresponds with the y centre of gravity of the recirculation area, indicated by the area enclosed by the blue lines. The blue star denotes the location of the top seam, while the green star represents the bottom seam. For illustration purposes a sketch of the baseball is given, so have a better understanding of where exactly the baseball is and how the seam pattern looks like. The stars denote the actual location of the seams, the baseball sketch is less accurate.

From the separation points, also the recirculation area is computed. This is the area where the borders have zero horizontal velocity, such that inside these borders there is an area with negative flow velocity. This is referred to as the recirculation area. Determining the centre of gravity for this field and specifically the y location determines if the wake is deflected upwards or downwards by comparing the y-c.o.g. of the recirculation area with the y-c.o.g. from the baseball centre. The recirculation area is the area inside the blue lines, where the blue circle shows the centre of gravity of the recirculation area. The stars on the baseball show the seam locations.

Using the collection of separation angles and the information from the recirculation areas and centres

of gravity, a statistical comparison can be made to inspect how these local effects are distributed with respect to the means.

The next step is to verify if the centre of gravity displacement of the wake can be compared with the lift coefficient. This is done by applying the momentum theory on a 2D plane, as explained by De Kat ([47]). Here the momentum integral of the wake velocity is used and is corrected for velocity fluctuation levels, by means of Reynolds averaging:

$$L = \iint_{Wake} \rho(\overline{u}\ \overline{w} + \overline{u'w'})dS \tag{4.1}$$

Here L is the lift [N], ρ is the density [kg/m^3], $\overline{u}$ is the mean horizontal velocity [m/s], $\overline{w}$ is the mean vertical velocity [m/s], $\overline{u}'$ is the average difference with respect to the horizontal mean velocity [m/s], $\overline{w}'$ is the average difference with respect to the vertical mean velocity [m/s]. Note that this is only the lift in 2D, while the full-field is unknown. Therefore this is not the true lift, but only a planar 2D proxy for comparison only. By taking the relative changes in the proxy lift and comparing those to the relative change in y-c.o.g. , this method is verified to check if it can be used to compare to the literature data from the lift coefficient for baseballs.

5

Results

In this chapter the results are discussed. From the flow fields the separation angles, recirculation areas and the shift in y centre of gravity are analysed. The chapter is divided into flow around a smooth sphere (Section 5.1), followed by the flow fields around a non-rotating baseball for the 2-seam and 4-seam configurations (section 5.2 and 5.3). The shift in y_{cg} will also be compared with a lift proxy in section 5.2.4 and 5.3.4, derived from the earlier introduced control volume momentum in section 4.2.2. These static flow fields are also compared with each other in section 5.3.5). From here the flow fields are analysed for a rotating smooth sphere, 2-seam and 4-seam configurations (section 5.4) and compared with each other and also a comparison is made between the static and dynamic cases. After demonstrating the similarity of behaviour for both the shift in centre of gravity and the lift proxy for the static cases, the shift in y_{cg} will be compared to the lift coefficient from literature data (Section 5.4.6).

5.1. Average Flow fields for the static smooth sphere.

This section discusses the flow field around a smooth sphere to understand the influence of a clean configuration, without the seams, on the wake. The main goal is to understand local flow phenomena before flow disturbances due to the seams have an influence of the size of the wake and the centre of gravity position.

The smooth sphere does not have flow altering seams. Therefore a symmetrical wake with respect to the horizontal axis through the centre of the smooth sphere is expected, such as found in the experiment performed by Jux, for a Reynolds number of 100,000 [10], see Figure 5.1.

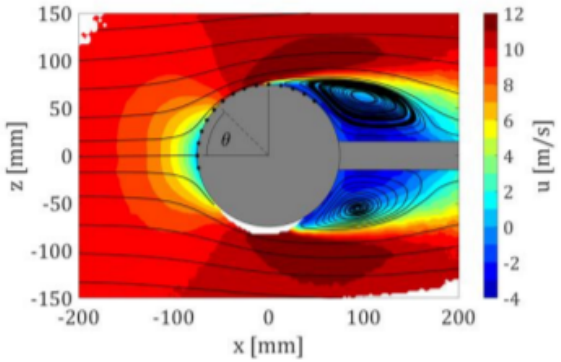

Figure 5.1: Flow field for 15 cm diameter sphere in a free stream at 10 m/s. The corresponding Reynolds number $Re_d = 10^5$. Here the wake is symmetrical, with the same separation angle on top and bottom. [10]

As the flow is laminar, from Figure 2.5 separation angles of 80-90 degrees are expected. However in the flow field (Figure 5.3) a non-symmetrical wake is observed. This is caused by a disturbance in the flow. As the separation point on the lower side lies before the measuring region, while the separation point on the top side lies around approximately 90 degrees, it is not exactly clear why the flow is shifted. An explanation is that with the assembly of the smooth sphere (it comprises of 2 halves), a small offset has occurred. The comprisal of the 2 halves with the glue line is shown in Figure 5.2.

Figure 5.2: Photograph of the 3D printed baseball, where the dotted line indicates where the 2 halves are glued together. The smooth sphere has the same orientation, with the same vertical glueline vertical through the center of the baseball, when viewed from the side.

This leads to a small edge on the lower side, which causes a disturbance flow and a smaller wake than the top side. At the top side the flow experiences laminar separation, leading to a larger wake, similar to the results earlier observed by the baseball. Another explanation could be that the shifted flow field is a result of the disturbance due to the horizontal rod in the test section. As a result the flow already experiences a shifted wake at zero rotation, as observed in Figure 5.3. The blue dot inside the white area denotes the center of gravity of the object, while the second blue dot (in the flow field) denotes the center of gravity from the recirculation area. The smooth sphere is not rotating. The separation angles are observed at 90 degrees (start of the recirculation area, enclosed by the blue lines). The recirculation area (delimited by the blue line) exhibits a centre of gravity that is located with the center of gravity above the horizontal line through the y_{cg} of the sphere, therefore the wake is shifted upwards. The separation occurs before 90°, which is expected due to laminar flow.

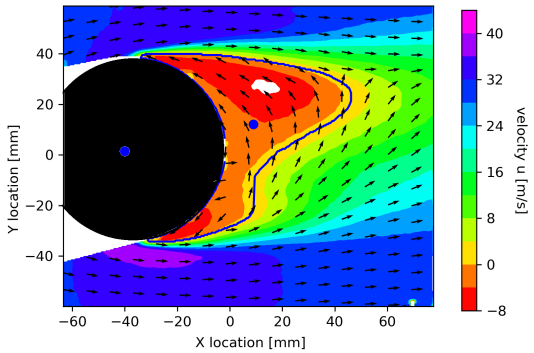

Figure 5.3: Contour of time-average streamwise velocity component of the smooth sphere, with in-plane velocity vectors. For this figure and all the following flow fields 86400 vectors are computed, but only 288 vectors are shown to have a less crowded vector plot and a more clear overview of the flow. The flow field is give for the horizontal velocity component in [m/s]. The black area indicates the sphere.

5.2. Flow analysis for the static 2-seam configuration

In this section the non-rotating 2-seam baseball is discussed. In section 5.2.1 the average streamwise velocity fields are shown with corresponding separation angles, y_{cg} and recirculation area. From these results and the location of the seams a direct effect of the seams can be distinguished, divided into 3

categories: separation before the seams, separation at the seams and separation after the seams. Also the separation will be divided into laminar separation, turbulent separation or separation at the seam. In section 5.2.2 the instantaneous images are in bulk analysed to find the mean value and standard deviation from the separation angles, recirculation area and y_{cg}. This differs from the value in Section 5.2.1, where the average velocity field is first computed and from the average velocity field the separation angles, recirculation area and y_{cg} are determined. In Section 5.2.3 the instantaneous images are analysed more in detail, to explain why the standard deviations differ for different configurations and to observe interesting behaviour, such as the in Section 5.2.3 explained bi-stability found in some configurations. Section 5.2.4 calculates the lift proxy parameter and compares it to the shift in centre of gravity.

5.2.1. Average Flow fields for the static 2-seam configuration

The starting configuration (also referred to as the neutral case, where the seams are in the back) is almost symmetrical with respect to the horizontal line passing through the y_{cg} of the baseball. This is not the most symmetrical configuration with respect to the seams. However, the most symmetric case for the seams showed a more shifted wake to 1 side and therefore the more balanced wake was chosen as a neutral point to start.

The front view and the back view for the starting configuration are shown in Figure 5.4. The front view shows 2 vertical seam, which are not inside the 2D planar measuring plane. However later in this chapter, flow effects will be detected explained by these vertical seams. The vertical seams are closest to each other when the 2 horizontal seams are 180 degrees on the other side, as demonstrated in Figure 5.4. For this chapter the orientation for the 2-seam baseball will be given with respect to the top seam, indicated with a blue star in the flow field, near the edge of the baseball.

Figure 5.4: Front view (left), back view (middle) and side view(right) for the symmetric 2-seam configuration

In Figure 5.5 the starting 2-seam orientation is given, with 2 seams at the back (respectively top seam at 151° and bottom seam at -162°). The separation angles can be observed from the start of the blue lines. The enclosed area by the blue lines encases the recirculation area. Inside this area the streamwise velocity component is zero or negative. As there are no seams upstream of the separation angle or other disturbances, the boundary layer is laminar and laminar separation occurs. Separation angles occur at approximately 90° and -90°, though for the upper side it is uncertain if separation actually occurs earlier, as angles before 90 degrees cannot be detected. The wake is relatively large, as the flow separates early from the baseball (before or approximately on 90° and -90° on top and bottom). This corresponds to the separation point of a smooth sphere for a Reynolds number of circa 150,000, see Figure 2.5 and the experiment from Jux ([10], Figure 5.1). Notice that the wake is wider, as Jux observed a more flattened elliptical shape. This is due to the vertical seam of the baseball in the front and possibly the material (the baseball not being a smooth sphere), changing the behaviour inside the boundary layer. As the horizontal seams are in the back, the separation occurs upstream of the seams.

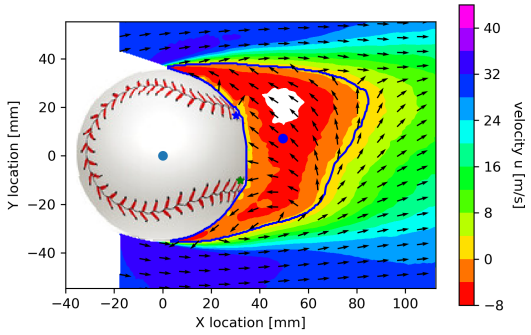

Figure 5.5: Contour of time-averaged flow field of the baseball with in-plane velocity vectors. This is the 2-seam configuration with the top seam at 151°, also referred to as the neutral case. Separation angles occur at approximately 90 and -90 °.

Changes in behaviour of the flow can be observed, while rotating the baseball clock-wise and counter-clockwise. The baseball is rotated between the measurements, while at the time of the measurements the baseball remains at a fixed position. The baseball will first be rotated counter-clockwise and later in this section the neutral position is rotated the other way, to have a comparison between +5°, +10° and -5°,-10° versus the neutral position.

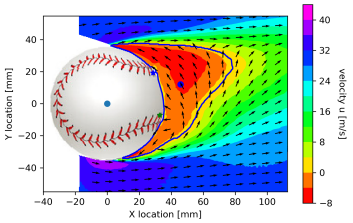

Figure 5.6: 2-seam configuration with the seam at 146°, rotated 5° counter clockwise with respect to the neutral configuration. The bottom separation occurs at approximately -90 degrees, while the size and up shift of the wake indicate that the top separation angle occurs before 90 degrees

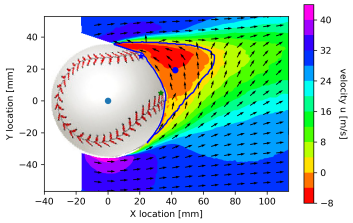

Figure 5.7: 2-seam configuration with the seam at 127°, rotated 24° counter clockwise with respect to the neutral configuration. The bottom separation occurs later than for the previous cases, indicating that the tripping effects on the bottom causes a turbulent boundary layer.

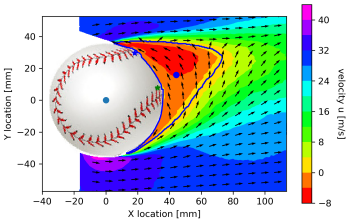

Figure 5.8: 2-seam configuration with the seam at 122°, rotated 29° counter clockwise with respect to the neutral configuration. The bottom separation occurs later than for the previous cases, indicating tripping effects on the bottom causes a turbulent boundary layer.

When the baseball is rotated 5° in counter-clockwise direction from the neutral configuration (see Figure 5.6), the 2 vertical seams move downwards over the lower side of the baseball, while the 2 horizontal seams rotate over the top side. This leads to delayed separation on the lower side and the shift of the wake upwards. The wake detaches on the lower side more vertically, which yields a smaller recirculation area. The upwards shifted wake along with a later separation on the lower side indicates an influence of the seams. This is not a direct influence of the horizontal seams, as these are in the back, downstream of the separation point. This is the influence of the vertical seams in the front, which are on either side of the 2D field. By interacting with the flow, a cross component appears to be disturbing the flow in the measurement plane and changing the behaviour of the flow, resulting in postponed separation. As these seams are upstream of the separation point and shift 5 degrees towards the backside of the baseball in the flow due to the rotation from the neutral configuration (151°) to this configuration (146°), the influence of a cross component of the flow on the boundary layer on the lower side increases. This would alter the flow and causes the boundary layer on the lower side earlier to transition. This results in a more aft separation point on the lower side. The top separation appears to be unaltered, while the y_{cg} is shifted upwards and the recirculation area appears smaller, due to a smaller recirculation area on the lower side.

The trend observed from rotating the baseball in steps of 5° (top side separation remains at similar position, while bottom separation moves more aft) continues up until 127°, as seen in Figure 5.7. By rotating the baseball further the flow on the lower side starts separating earlier again, see Figure 5.8. It appears that the vertical 2 seams in front are rotated to a point in front where the transition on the lower side of the flow happens later and does not cause the turbulent separation. Instead now laminar separation is seen.

The wake remains similar in behaviour up until the top seam reaches 106°, see Figure 5.9. At this location the seams appears to cause separation. By rotating it further the flow separation follow the seam, leading to earlier flow separation on the top side, as seen in Figure 5.10. More effects can be observed by rotating it 5 more degrees, to 91°, see Figure 5.11. Here separation occurs earlier, also at the seam and the wake on the top deflects upwards. The wake increases as the separation on the top occurs earlier and the wake shifts upwards.

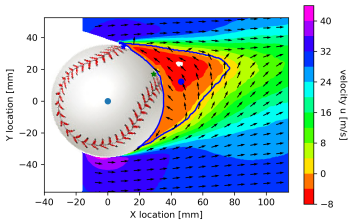

Figure 5.9: 2-seam configuration with the seam at 106°, rotated 45° counter clockwise with respect to the neutral configuration.

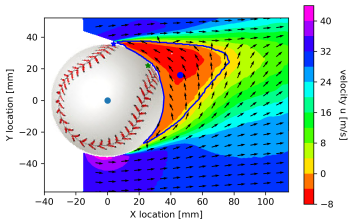

Figure 5.10: 2-seam configuration with the seam at 96°, rotated 55° counter clockwise with respect to the neutral configuration. The bottom separation point has moved again more aft, due to the influence of the 2 vertical seams that also moved more aft.

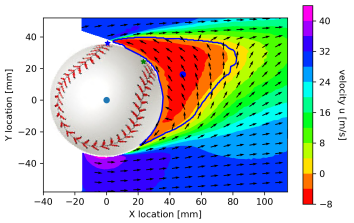

Figure 5.11: 2-seam configuration with the seam at 91°, rotated 60° counter clockwise with respect to the neutral configuration. The recirculation area has grown with respect to previous configuration.

Rotating it further counter-clockwise causes the same trend of earlier separation and increasing of the recirculation area. With this information, it appears that the separation is following the seam. This however cannot be detected, as only separation angles >90° can be detected. When the top seam passes 80°, the flow behaviour is altered. At a location of 78° for the top seam, the wake decreases a little, but for a location of 73° for the top seam there are more distinct changes in the flow, see Figure 5.12 and 5.13. It appears that now the bottom seam is causing separation. In Figure 5.13 a smaller and more symmetric wake can be observed. The top seam causes the boundary layer to transition to a turbulent boundary layer on the upper half, with as consequence a later separation point. This is negated by the bottom seam, which causes separation. The influence of the vertical seams causes a similar delay in transition on the lower side. While rotating the baseball further the top seam keeps causing the flow to trip to make it turbulent, while the bottom seam causes the flow to separate. On the lower side, the 2 vertical seams move more aft, but the behaviour on the lower plane does not change.

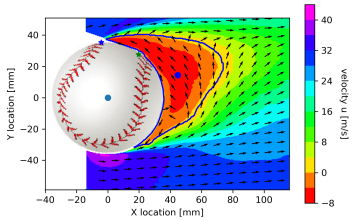

Figure 5.12: 2-seam configuration with the seam at 78°, rotated 73° counter clockwise with respect to the neutral configuration. The y_{cg} of the recirculation area is shifted upwards. The bottom separation angle does not appear to be changed, but on the top side the recirculation area has grown.

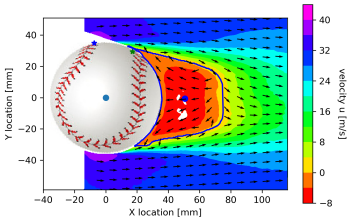

Figure 5.13: 2-seam configuration with the seam at 73°, rotated 78° counter clockwise with respect to the neutral configuration. Both separation angle have moved more aft, relating to separation occurring due to a turbulent boundary layer.

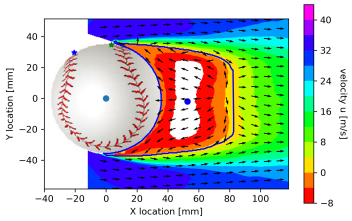

Figure 5.14: 2-seam configuration with the seam at 50°, rotated 101° counter clockwise with respect to the neutral configuration. Here the recirculation area is quite large, as both upper and lower separation occurs early. The lower seam, indicated by the green star, tends to cause separation on the top side, while on the lower side the effect of the 2 vertical seams is now downstream of the separation point.

By rotating it further, the behaviour is altered: At a location of 50° for the top seam, see Figure 5.14, a large symmetrical wake occurs. The combination of the top seam and bottom seam causes the flow to separate at the bottom seam, while for the lower half the influence of the 2 vertical seams is moved more aft. As the vertical seams move more aft than the laminar separation point, the lack of influence on the flow causes laminar separation. While rotating the baseball, the behaviour on the lower side is not visibly altered, since the 2 vertical seams are now more aft than the bottom separation point. The top seam and bottom seam on the upper half of the baseball however are moving more to the front.

With the seam position at 37°, the current placement of the seams forces the top separation point to move more aft. The bottom seam does not cause separation anymore, but instead the combination of the 2 seams trip the flow, see Figure 5.15 and Figure 5.16. The separation point on the top side moves more aft, until the front seam is at the front. Counter rotating it further, would position the top seam at the bottom half of the baseball and it will be affecting the bottom half. This is seen in Figure 5.17.

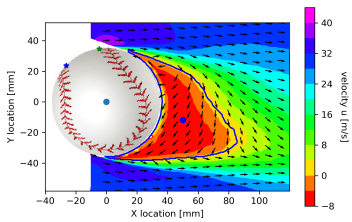

Figure 5.15: 2-seam configuration with the seam at 37°, rotated 114° counter clockwise with respect to the neutral configuration. The bottom has laminar separation. On the top side turbulent separation is observed. The recirculation area becomes smaller and is shifted downwards.

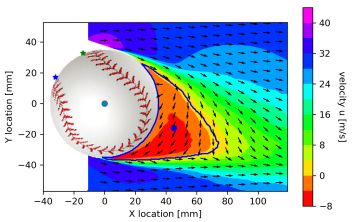

Figure 5.16: 2-seam configuration with the seam at 23°, rotated 128° counter clockwise with respect to the neutral configuration. The top side experiences a more turbulent boundary layer as compared to the previous configuration, Figure 5.15. As the top separation is delayed, the recirculation area decreases.

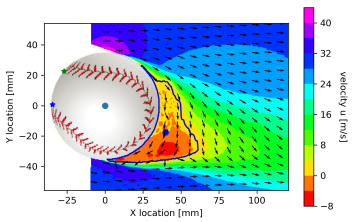

Figure 5.17: 2-seam configuration with the seam at -4°, rotated 155° counter clockwise with respect to the neutral configuration. The recirculation area here is small. The behaviour on the bottom side is not changing. On the upper side, the flow becomes more fully developed turbulent. Due to the upper side separation point moving more aft, the recirculation area size decreases.

By rotating the baseball further, a position is reached where the top seam is almost symmetric with the

bottom seam (Figure 5.18), with respect to the horizontal axis through the centre. The top seam is at -12°, the bottom seam is at 25°. Both seams are at the front of the baseball. The almost symmetrical outlook is also observed in the wake, where it appears approximately symmetric and the y_{cg} is roughly the same as the baseball centre of gravity. The recirculation is also much smaller, although early separation angles are observed (close to -90° and 90°). This observation will be explained in section 5.2.3.

Rotating the baseball further cancels out the balancing behaviour, although the seams move to a more symmetric position (-16° and 21° and -22° and 17°), see Figure 5.19 and 5.20. Here the top seam causes on the lower side of the baseball a turbulent flow, while the bottom seam is not causing a turbulent flow on the upper side. This leads to a delayed separation on the lower side, while the upper side flow is separating early. Interesting is to see that for a more broken symmetry setting such as Figure 5.18 a more symmetrical wake is observed.

In Figure 5.21 different behaviour is detected by comparing it to Figure 5.19 and 5.20. The wake appears again to be more symmetric and with a smaller recirculation area, like Figure 5.18. The seams are located at-25 ° and 12°. This is mirrored with respect to Figure 5.18. Here also the wake is smaller and will also be explained in section 5.2.3.

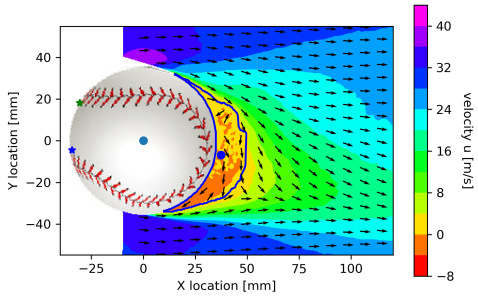

Figure 5.18: 2-seam configuration with the seam at -12°, rotated 163° counter clockwise with respect to the neutral configuration. The recirculation is small and also the higher negative velocities (deep red regions in the figure) do not seem to occur. The separation angles are not far aft, so this flow field is different than the other.

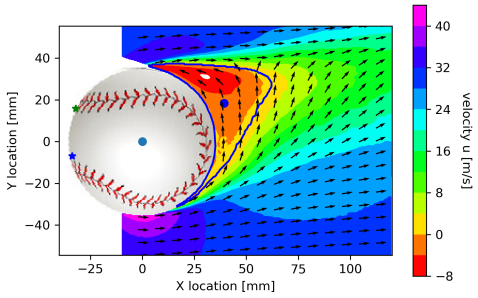

Figure 5.19: 2-seam configuration with the seam at -17°, rotated 168° counter clockwise with respect to the neutral configuration. Top side separation occurs early, indicating the effect of the lower seam is not influencing the boundary layer. On the lower side the separation point is delayed, indicating that the top seam, which is now on the lower half, influences the flow into a turbulent boundary layer

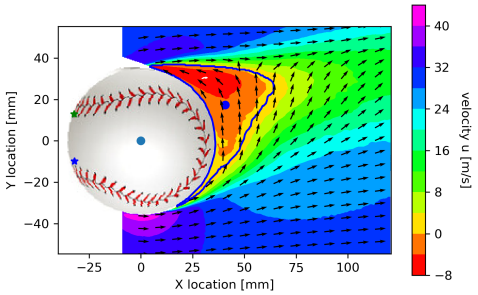

Figure 5.20: 2-seam configuration with the seam at -22°, rotated 173° counter clockwise with respect to the neutral configuration. The flow field appears similar as the previous one, for both top separation angle and bottom separation angle. The recirculation area size and shift of y_{cg} also appears similar.

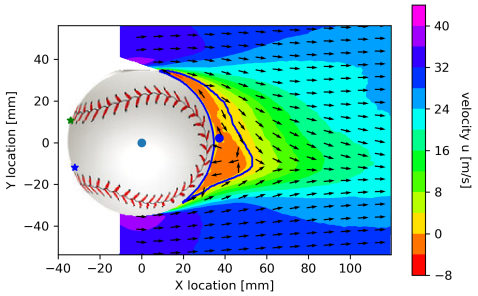

Figure 5.21: 2-seam configuration with the seam at -25°, rotated 176° counter clockwise with respect to the neutral configuration. Here the recirculation area tends to be similar as previous configuration (Figure 5.18). and also similar more aft separation angles.

The clockwise rotation from the neutral position can be observed in Figure 5.22 and 5.23. Similar for the counter-clockwise rotation, the horizontal seams are downstream of the separation point and the vertical seams are not in the 2D path of the flow, but still changes in the flow are observed. On the upper side separation is delayed with respect to the neutral case Figure 5.5, while separation on the lower side is still occurring at circa 90°. Figure 5.22 and 5.23 show a much smaller wake and recirculation area, due to a sharper angle from the upper separation point from the 2 vertical seams, which moved upwards. This causes the size of the wake to be smaller and to have a lower y_{cg}. The size of the recirculation area has decreased with respect to Figure 5.5 and Figure 5.22 and 5.23 show a lower y_{cg}.

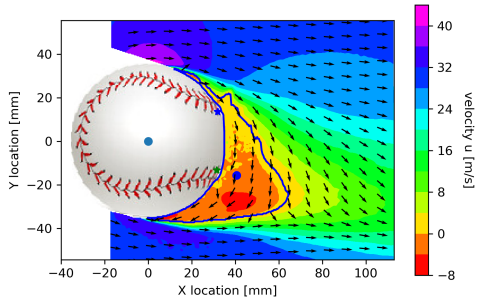

Figure 5.22: 2-seam configuration with the seam at 157°, 5 degrees clockwise rotated with respect to the neutral configuration. At the bottom the flow is still undisturbed and a separation angle of approximately 90 degrees is observed. For the top side however a delayed separation is seen, as the separation angle moves more aft and the recirculation area with the y_{cg} is also deflected downwards.

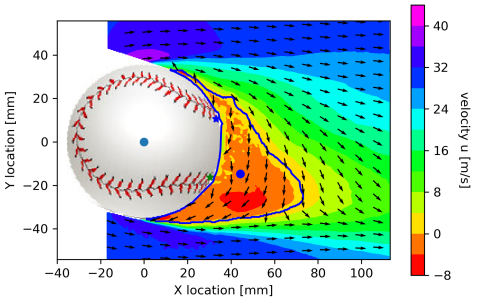

Figure 5.23: 2-seam configuration with the seam at 162°, rotated 10° clockwise with respect to the neutral configuration. The bottom shows again a similar separation angle, while on the top the separation is further delayed due to the vertical seam moving more downstream of the flow. This results in a later turbulent transition and a more downwards shifted wake.

Interesting here is that Figure 5.22 has seams which are closer to a full symmetric setting (seams at 156° and -157°) than the neutral case, where the seams are at 151° and -162, but here also a more shifted wake is seen. Similar to what was previously observed with the seams in front close to the symmetric case (Figures 5.18 to 5.21). Figure 5.23 shows a larger recirculation area for approximately similar separation angles in comparison with Figure 5.22.

The observed separation angles are summarised in Table 5.1 and visualised in Figure 5.24 and Figure 5.25. Notice that grey line in Figure 5.24 is the location where the seam angles match the separation

angle. The first grey line observed holds for the lower seam, while the second grey line is the top seam. The y_{cg} and the recirculation area are summarised in Table 5.2, and visualised in Figure 5.27 and Figure 5.26.

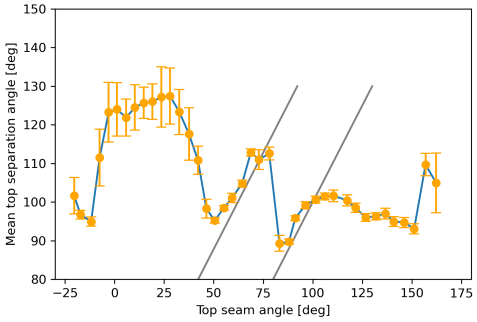

Figure 5.24: Overview top separation angle per configuration, within a bound of -1 and 1 standard deviation. As the baseball counterrotates, the top seam and bottom seam will pass to the separation domain on the upper side and therefore is the influence with the flow can be observed. Separation on the seam is observed when then grey line intersects with the graph. The first grey line indicates separation on the bottom seam, while the second grey line indicates separation on the top

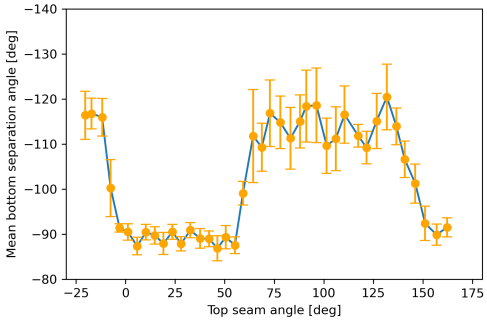

Figure 5.25: Overview bottom separation angle per configuration, within a bound of -1 and 1 standard deviation

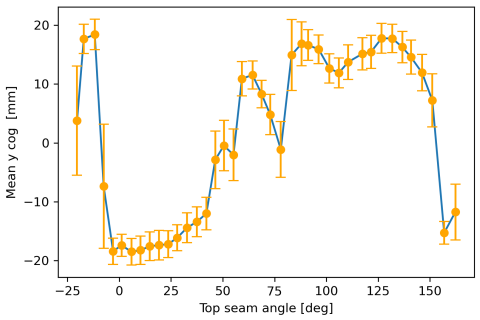

Figure 5.26: Overview y_{cg} per configuration, within a bound of -1 and 1 standard deviation

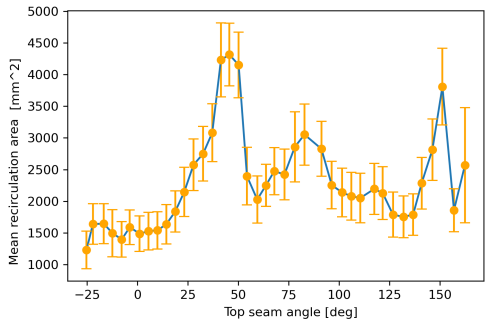

Figure 5.27: Recirculation area per configuration, within a bound of -1 and 1 standard deviation

The influence of the seams can also be captured as a pie chart over the baseball, to indicate in which regions the seams cause separation, are aft the separation or cause tripping, resulting into delayed separation. This is done in Figure 5.28 and 5.29. The first figure is the separation angle with respect to the top seam angle, the second figure is with respect to the bottom separation angle.

For the top seam, from 180° to 106° the seams are behind the separation point. Separation on the top seam happens at 106° to 77°, while separation on the bottom seam happens at a top seam angle of 78° to 37°. From 37° to 0°, the seams are in front of the separation point and the flow is tripped, leading to a turbulent and more aft separation. For the lower seam these angles are shifted all approximately 42°.

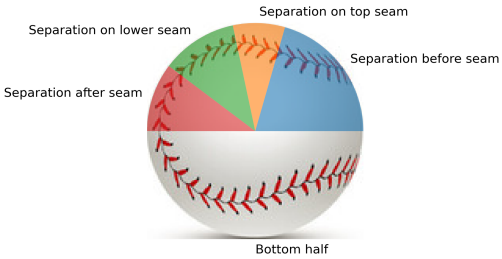

Figure 5.28: Area of influence of the seams on the 2-seam configuration. Orientation with respect to the top seam

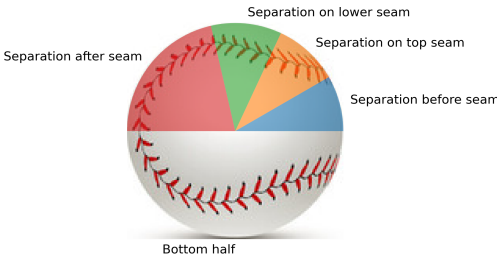

Figure 5.29: Area of influence of the seams on the 2-seam configuration. Orientation with respect to the bottom seam

5.2.2. Statistical analysis of the static 2-seam baseball configurations

The previous section focused on the average velocity fields and the corresponding separation angles, recirculation areas and y_{cg}. To investigate these observations the variation of the separation angles, recirculation areas and y_{cg} are investigated. This will be done by comparing the mean values and standard deviations per configuration. Here the mean value is the separation angle calculated from finding the separation angle per instantaneous image and finding the mean value. This differs from the separation angle found in the average velocity fields, where first all the instantaneous velocity fields are averaged and from this average field the separation angle is determined. The standard deviation is taken with respect to the mean value of the separation angles from the instantaneous images and not the values from the average velocity field. In the end a visual comparison will be given, where the average values are plotted within the bounds of -1 and +1 standard deviation.

The flow field illustrated in Figure 5.5 features laminar separation (the neutral case, with the seams in the back). The separation occurs at -96° and 94°. For the top side it is possible that this value is not entirely accurate as separation occurring before 90° cannot be detected and the value for these cases will be approximately 90°. This is also observed in the standard deviation of the top separation angle, which is relatively small (1.8°). The standard deviation on the bottom side shows more variance (3.9°). These angles are also given in Table 5.1, along with the other configurations. The first column denotes the configuration. The second and third column are the bottom separation angle average (BSA Avg) and the bottom separation angle standard deviation (BSA StD). The fourth and fifth column are the top separation angle average (TSA Avg) and the top separation angle standard deviation (TSA StD). The green color indicates top separation upstream of the seam. The yellow color indicates separation on or very close to the top seam. The blueish color indicates separation on or very close to the bottom seam. The red color shows separation downstream of the seam.

From Table 5.1 it can be observed that the top separation angle is relatively fixed for seam angle for 151 to 106° (Figures 5.5 to 5.9), while the separation angle is around 89-100° (Table 5.1). This is the range where the seam is downstream of the separation point, hence the separation point varies less. When counter rotating the baseball further, the separation point follows the top seam.

The flow field for 73° seam angle (Figure 5.13) with a separation angle similar to turbulent separation, shows a small standard deviation for the top separation angle (1.8 °, from Table 5.1). If the flow separates at the seam, it is expected that there is less variation downstream of the seam, as the geometrical offset of the seam causes direct separation (or in some individual images delay of separation). For laminar separation, there is no triggered separation due to the seam and the separation location is more normal distributed. This is observed for the bottom separation angle, where the standard deviation is larger (6.2 °, from Table 5.1).

Top right seam angle [°]	BSA avg [°]	BSA StD [°]	TSA avg [°]	TSA StD [°]
151	-96	3.9	94	1.8
157	-90	2.7	110	3.2
162	-92	2.3	110	8.1
146	-106	4.6	94	1.7
122	-111	3.9	99	1.5
96	-130	8.3	100	1.1
91	-127	8.0	97	1.0
78	-118	5.9	89	2.2
73	-121	6.2	114	1.8
50	-93	1.9	98	0.7
37	-93	1.3	113	3.7
23	-92	1.1	133	7.6
-4	-95	0.8	132	6.8
-12	-106	6.3	115	7.6
-17	-118	4.3	95	1.5
-22	-119	3.4	97	1.4
-25	-124	5.4	105	4.9

Table 5.1: The top and bottom separation angle averages and standard deviations. The first column denotes the configuration. The second and third column are the bottom separation angle average (BSA Avg) and the bottom separation angle standard deviation (BSA StD). The fourth and fifth column are the top separation angle average (TSA Avg) and the top separation angle standard deviation (TSA StD). The green color indicates top separation upstream of the seam. The yellow color indicates separation on or very close to the top seam. The blueish color indicates separation on or very close to the bottom seam. The red color shows separation downstream of the seam

Seam angle 50° (Figure 5.14) shows stable separation behaviour, due to a small standard deviation. The stable separation behaviour along with the position of the seam indicates that the seam still has a separating effect. When the seams move upstream of the separation point, there is a larger and increasing variance in the separation angle, as observed for top seam angles ranging from 37° to 4° (Figure 5.15 to Figure 5.17 and Table 5.1). This corresponds to an increasing separation angle, relating to turbulent separation. For top seam angles -17° and -22° (Figure 5.19 and 5.20) the separation is laminar. The first detection here is around 95° and has a small standard deviation.

This variation in separation angles also influences the y_{cg} and the recirculation area, as observed in Table 5.2. Here the starting configuration (top seam angle at 151°, Figure 5.5) has a relative large wake and the y_{cg} varies relatively much in comparison to the ones with top seam angle at 157 and 162°, considering 162° has bi-stable behaviour due to the bottom separation angle and 151° has not. The effect of the bi-stable behaviour (explained in Section 5.2.3) is shown from the standard deviation of the recirculation area. The bi-stable behaviour with top seam angle at -12° and -25° shows the largest standard deviation for the y_{cg}, while the bi-stable behaviour of 162° causes the largest changes in recirculation area.

Top seam angle [°]	y_{cg} avg [mm]	y_{cg} StD [mm]	recirc avg [mm^2]	recirc StD [mm^2]
151	3.9	4.6	3001	608
157	-19.1	2.1	1305	341
162	-18.4	4.8	1672	909
146	9.2	3.1	2139	487
122	15.3	2.8	1602	415
96	15.9	2.5	1742	375
91	16.3	2.6	2260	435
78	15.5	6.0	2104	554
73	0.5	4.7	1954	400
50	-1.4	4.5	3405	519
37	-11.5	3.0	2510	458
23	-16.7	2.2	1690	389
-4	-19.7	2.0	1159	273
-12	-9.7	10.6	740	372
-17	15.0	2.6	1177	317
-22	14.1	2.5	1224	321
-25	-1.9	9.3	693	296

Table 5.2: The y_{cg} and recirculation area averages and standard deviations. The green color indicates top separation upstream of the seam. The yellow color indicates separation on or very close to the top seam. The blueish color indicates separation on or very close to the bottom seam. The red color shows separation downstream of the seam

For a top seam angle of 157° and 162° (Figure 5.22 and 5.23), the flow field shows a downwards deflected wake. The bottom separation tends to have less spreading in separation angles, as the standard deviation is smaller, see Table 5.1. This can be explained by the fact that the 2 horizontal seams are downstream of the separation point, while the 2 vertical seams are on the upper half of the baseball and influences the flow on the lower side less. The top separation for 157° and 162° happens at the same point, however a difference in standard deviation is observed. The top seam angle at 162° shows bi-stable behaviour on the top side and hence has a higher standard deviation (respectively 8.1 vs 3.2).

5.2.3. Instantaneous flow analysis for the static baseball in the two-seam configuration.

The top separation angles per instantaneous image can be seen in Figure 5.30 for the neutral case, the bottom separation angles per instantaneous image for the neutral case can be seen in Figure 5.31. Here the blue lines indicate the separation per instantaneous image, the ”avg” line is the separation angle according to the averaged velocity field, while the ”mean” line represents the mean value of all the separate instantaneous separation angles. For the top separation angle the minimum is indeed observed as 90°, where most of the images show a separation angle between 90° and 100°. The bottom separation angle shows more variation, where the separation differs mostly between -85° and -97°. Configurations with similar trends with respect to separation, also show relative small standard deviations, as can be observed for seam angles 157°, 151°, 146° and 122°.

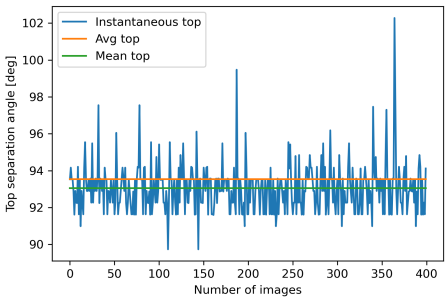

Figure 5.30: 2-seam, top seam angle 151°: Top separation angle. The blue lines indicate top separation per instantaneous image, the orange ”avg” line is the top separation angle according to the averaged velocity field, while the green ”mean” line represents the mean value of all the separate instantaneous top separation angles.

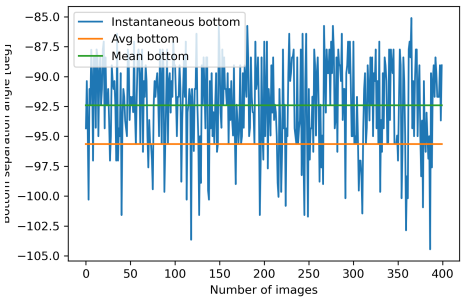

Figure 5.31: 2-seam, top seam angle 151°: Bottom separation angle. The blue lines indicate bottom separation per instantaneous image, the orange ”avg” line is the bottom separation angle according to the averaged velocity field, while the green ”mean” line represents the mean value of all the separate instantaneous bottom separation angles.

Top seam angles located between 96 and 91° (Figure 5.10 and 5.11) show bottom separation at -130 and -127°, indicating turbulent separation on the lower side. This is also observed from a relative high standard deviation. By rotating the baseball further, the 3D influence becomes apparent, as the standard deviation decreases and the separation point moves more upstream. The separation angles for the instantaneous images correspond with this, see Figures 5.32 to 5.35. In these figures it can be seen that on the top side there is no apparent change on the top side, where the bottom shows a lot more variation due to the turbulent separation.

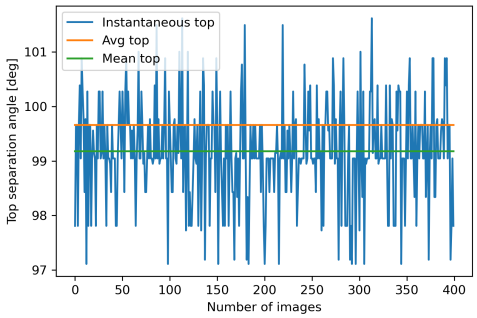

Figure 5.32: 2-seam, top seam angle 96°: Top separation angle. The blue lines indicate top separation per instantaneous image, the orange ”avg” line is the top separation angle according to the averaged velocity field, while the green ”mean” line represents the mean value of all the separate instantaneous top separation angles.

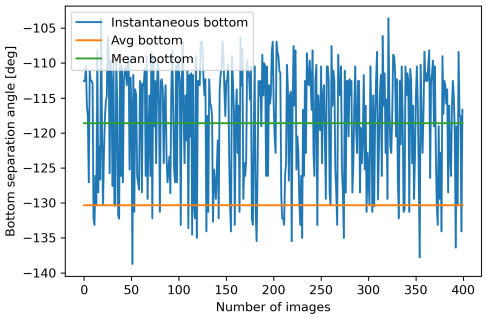

Figure 5.33: 2-seam, seam angle 96°: Bottom separation angle. The blue lines indicate bottom separation per instantaneous image, the orange ”avg” line is the bottom separation angle according to the averaged velocity field, while the green ”mean” line represents the mean value of all the separate instantaneous bottom separation angles.

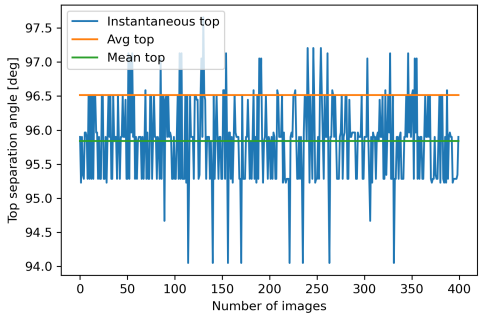

Figure 5.34: 2-seam, top seam angle 91°: Top separation angle per instantaneous image

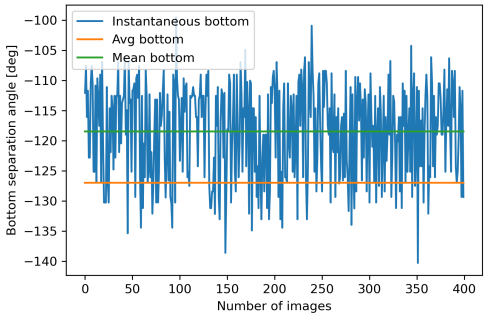

Figure 5.35: 2-seam, seam angle 91°: Bottom separation angle. The blue lines indicate bottom separation per instantaneous image, the orange ”avg” line is the bottom separation angle according to the averaged velocity field, while the green ”mean” line represents the mean value of all the separate instantaneous bottom separation angles.

At 50° top seam (Figure 5.14) there is again relative early separation and the standard deviation becomes again relatively small. As the separation point remains approximately constant from 50° to 23° (Figure 5.14 to 5.16), this suggests that there is laminar, fixed separation. For the cases where the seam angle is between 23° and -4°, a high standard deviation is observed on the top side, with also corresponding turbulent separation (separation angles > 120° or < -120°). This is also observed in Figures 5.36 and 5.37.

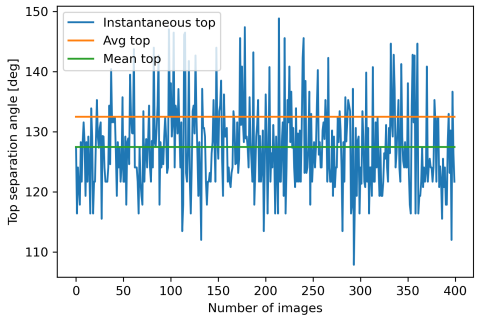

Figure 5.36: 2-seam, top seam angle 23°: Top separation angle. The blue lines indicate top separation per instantaneous image, the orange ”avg” line is the top separation angle according to the averaged velocity field, while the green ”mean” line represents the mean value of all the separate instantaneous top separation angles.

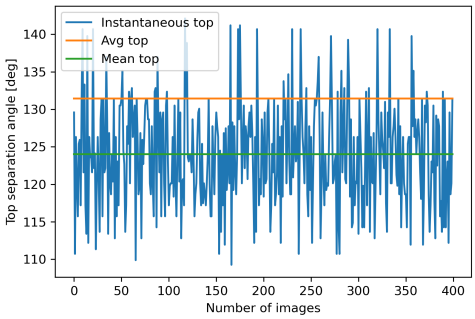

Figure 5.37: 2-seam, top seam angle -4°: Top separation angle. The blue lines indicate top separation per instantaneous image, the orange ”avg” line is the top separation angle according to the averaged velocity field, while the green ”mean” line represents the mean value of all the separate instantaneous top separation angles.

From -4° to -25° (Figure 5.17 to 5.21) the separation angle moves more aft and the standard deviation increases.

Special cases are when the top seam angles are at -12° and -25° (Figure 5.18 and 5.21). Here the flow shows bi-stable behaviour. This is the changing of the behaviour of the flow, where there are 2 main configurations. The flow alternates modes between these configurations. Figure 5.38 and Figure 5.39 show both instantaneous image of the same configuration, but with different flow behaviour demonstrating the bi-stability. As a consequence a high standard deviation is seen in Table 5.1. The top separating angle per instantaneous image can be seen in Figure 5.40 and 5.41. This shows the alternating behaviour.

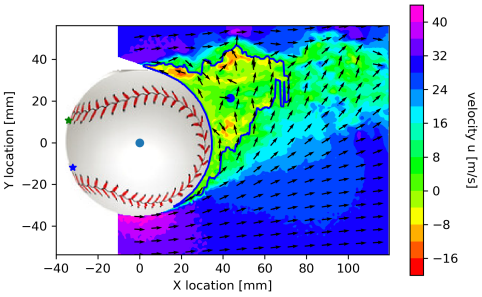

Figure 5.38: Instantaneous image with the seam at -25°: Wake is deflected upwards

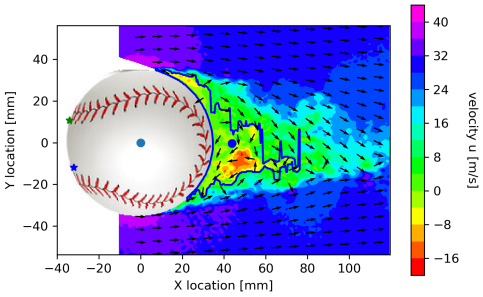

Figure 5.39: Instantaneous image with the seam at -25°: Wake is smaller and does not appear to have an upwards or downwards deflection

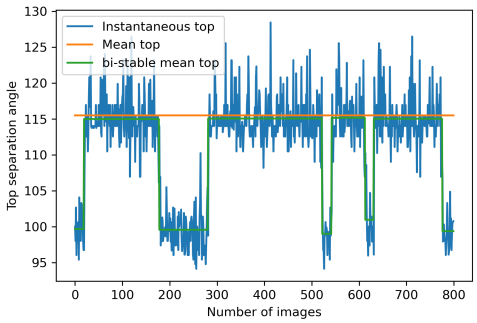

Figure 5.40: 2-seam, top seam angle -12°: Top separation angle. The blue lines indicate top separation per instantaneous image, the orange ”avg” line is the top separation angle according to the averaged velocity field, while the green ”mean” line represents the mean value of the separate instantaneous top separation angles, sorted by the bistable modes.

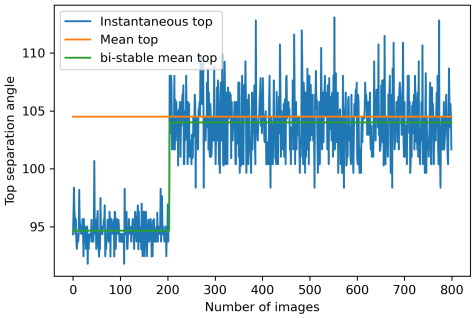

Figure 5.41: 2-seam, top seam angle -25°: Top separation angle.

The bi-stable behaviour of the bottom separation angles for these configuration are seen in Figure 5.42 and 5.43. Here it shows that there can be early separation or later separation and the flow alternates between these modes. Due to the bi-stability of the separation angles, it also shows the y_{cg} for both cases has bi-stability. Due to the -12 degrees configuration having both top and bottom separation angles which alternate at the same moment, the recirculation area here shows no bi-stability. For -25° both the y_{cg} and recirculation area show corresponding bi-stable behaviour to the top separation angle, meaning that the change of separation angles also increases and decreases the recirculation area. This is seen in Figure 5.44 to 5.47.

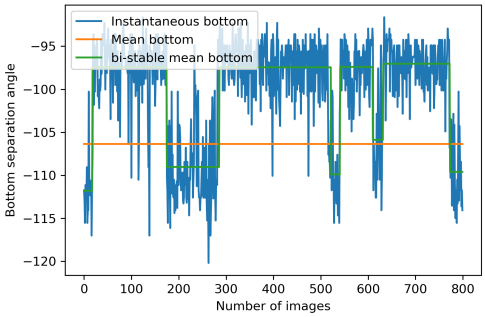

Figure 5.42: 2-seam, top seam angle -12°: Bottom separation angle. The blue lines indicate bottom separation per instantaneous image, the orange ”avg” line is the bottom separation angle according to the averaged velocity field, while the green ”mean” line represents the mean value of the separate instantaneous bottom separation angles, sorted by the bistable modes.

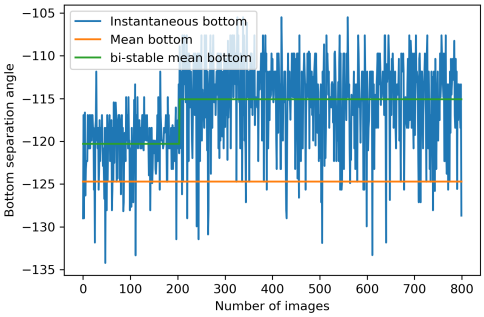

Figure 5.43: 2-seam, top seam angle -25°: Bottom separation angle.

An explanation for the bi-stable behaviour could be that the bottom seam is close enough to the front to have a switching role for the lower and upper flow, while the top seam is not significantly influencing the flow with respect to the bottom seam. This could also be due to a geometrical offset or some influence on the flow from the horizontal rod holding the baseball.

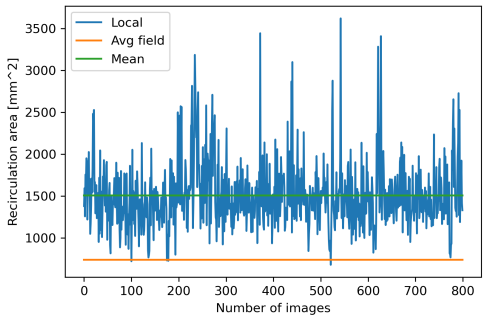

Figure 5.44: 2-seam, top seam angle -12°: Recirculation area per instantaneous image

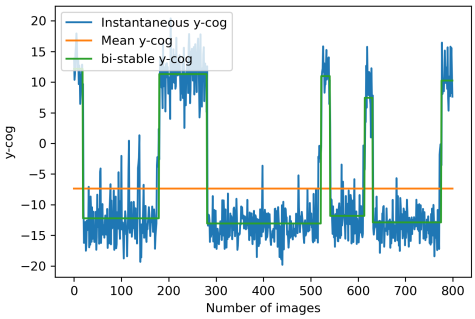

Figure 5.45: 2-seam, top seam angle -12°: y_{cg} per instantaneous image

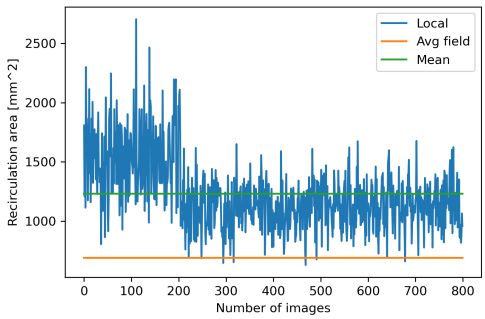

Figure 5.46: 2-seam, top seam angle -24°: Recirculation area per instantaneous image

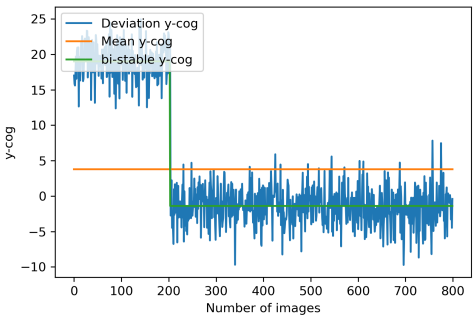

Figure 5.47: 2-seam, top seam angle -24°: y_{cg} per instantaneous image

The altering modes can also be observed for the configuration with the seams in the back at 162°

(Figure 5.23) in Figure 5.48. Meanwhile, the bottom separation angle has no bi-stable behaviour, as observed in Figure 5.49.

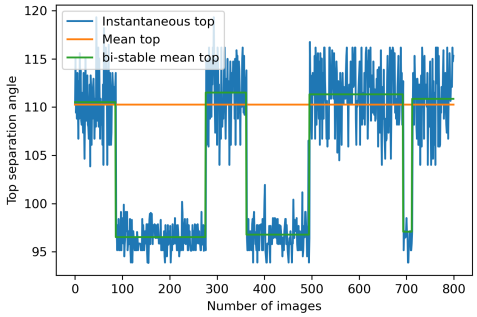

Figure 5.48: 2-seam, top seam angle 162°: Top separation angle. The blue lines indicate top separation per instantaneous image, the orange ”avg” line is the top separation angle according to the averaged velocity field, while the green ”mean” line represents the mean value of the separate instantaneous top separation angles, sorted by the bistable modes.

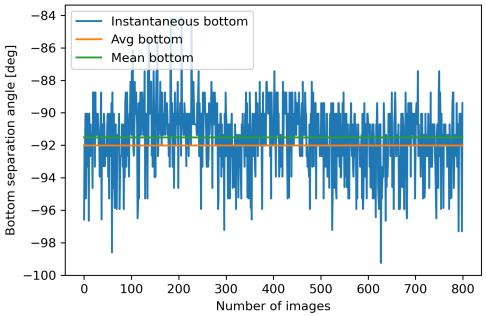

Figure 5.49: 2-seam, top seam angle 162°: Bottom separation angle. The blue lines indicate bottom separation per instantaneous image, the orange ”avg” line is the bottom separation angle according to the averaged velocity field, while the green ”mean” line represents the mean value of all the separate instantaneous bottom separation angles.

The bi-stable behaviour with the seams in the back was not observed on the lower side for the seam at 162°. Here the configuration with the top seam angle at 162° (Figure 5.23) shows the smallest standard deviation for the bottom separation angle. However, there is bi-stable behaviour observed for the top separation angle. As a consequence therefore, also the y_{cg} and recirculation area vary, observed in Figure 5.50 and 5.51

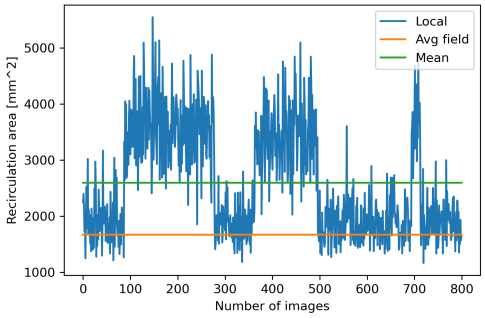

Figure 5.50: 2-seam, top seam angle 162°: Recirculation area per instantaneous image

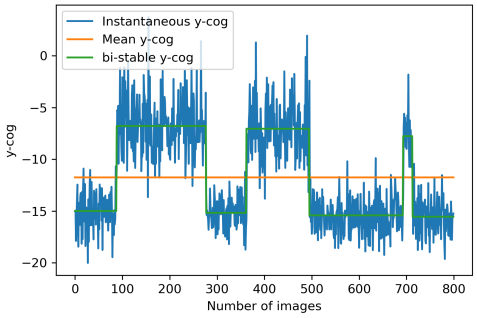

Figure 5.51: 2-seam, top seam angle 162°: y_{cg} per instantaneous image

5.2.4. Comparison lift similarity parameter and centre of gravity shift for the non-rotational 2-seam configuration

As described in section 4.2.2, the shift in centre of gravity is compared to a 2D lift proxy parameter. This step is performed on the data from the non-rotating 2-seam and 4-seam. For every seam position of the 2-seam configuration, the positional shift in y_{cg} is calculated, For the same configurations also the wake integral velocity and Reynolds stresses are calculated by using Equation 4.1. These results are compared with each other. Figure 5.52 shows the shift in y_{cg}. This shift is made non-dimensional by dividing it over the radius of the baseball.

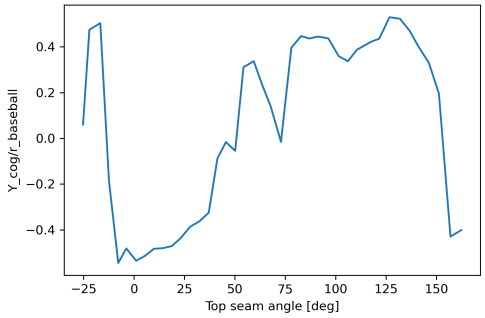

Figure 5.52: Shift in y_{cg} per configuration (non-dimensional)

The next step is to calculate the lift proxy parameter. This is done by taking the momentum exchange at the vertical line at the end of the flow field. These results are also made non-dimensional, by dividing over free stream dynamic pressure and the diameter of the baseball. Figure 5.53 shows the wake integral of the velocity versus the top seam angle. Figure 5.54 shows the Reynolds stresses versus the top seam angle.

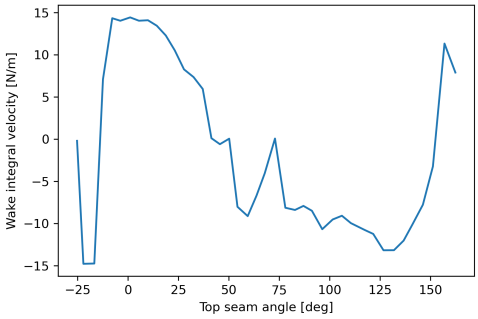

Figure 5.53: Wake integral of the velocity versus the top seam angle

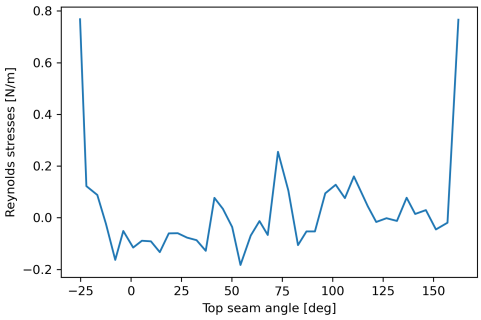

Figure 5.54: Reynolds stresses versus the top seam angle

It can be concluded that the Reynolds stresses in most cases account for < 5%, but for some configurations have a small correcting quality. Also Figure 5.53, 5.54 are compared with each other in Figure 5.55 (non-dimensional). Here the wake integral property consists of the stream wise and normal velocity, while the lift proxy includes the wake integral and the Reynolds stresses. Here the action-reaction principle becomes apparent, as the shift in y_{cg} is in the same order as the opposite reaction of the lift force. When mirroring the response (the force upwards is taken as negative), the plots indicate similar behaviour, as seen in Figure 5.56 (non-dimensional.

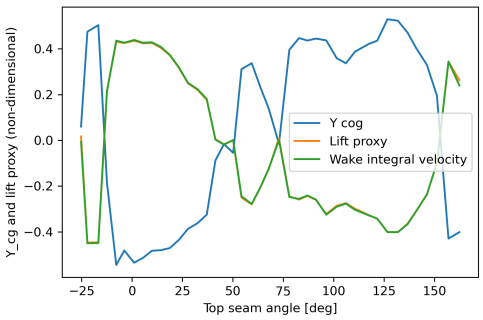

Figure 5.55: Comparison of the non-dimensional shift y_{cg} with the 2D lift proxy. Here a positive lift proxy corresponds with a force moving upwards

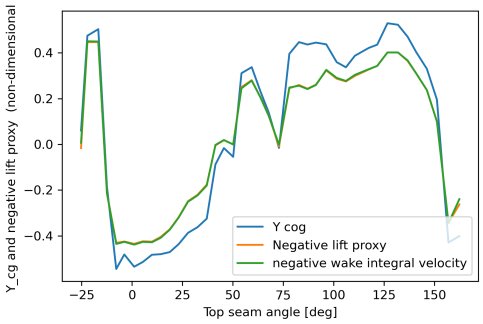

Figure 5.56: Comparison of the non-dimensional shift y_{cg} with the 2D lift proxy. Here a positive lift proxy corresponds with a force moving downwards

5.3. Flow fields 4-seam

In this section the static flow fields of the 4-seam configuration are discussed. This holds the same structure as the 2-seam configuration. Now in the measurement plane there are more seams and also more evenly spaced. This will hold that for every 90 degrees rotation, the baseball will be symmetric to the original case and therefore only rotation up to 90° is researched.

5.3.1. Average Flow fields for the static 4 seam configuration

The almost symmetrical outlook of the 4-seam with respect to the horizontal axis through the centre of the baseball produces similarly an almost symmetrical wake, see Figure 5.57 with the top right seam located at 130°. The wake is much smaller in comparison to laminar separation, as separation occurs much later. This indicates that the seams in front have tripped the flow into turbulence, while the seams in the back cause separation. While rotating the baseball counter clockwise, it is clear that the flow separates at the top right seam and moves with the seam, see Figure 5.58 and 5.59. On the lower half it is seen that the separation occurs approximately at the same position, indicating a normal turbulent separation angle. While rotating the baseball further, the separation still follows top right seam. The separation of the lower half is postponed due to the shift of the seam, resulting into a wake shifting up.

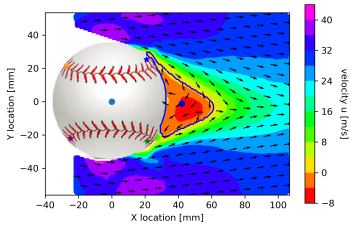

Figure 5.57: Time-averaged flow field baseball, 4-seam configuration with the top right seam at 130°.

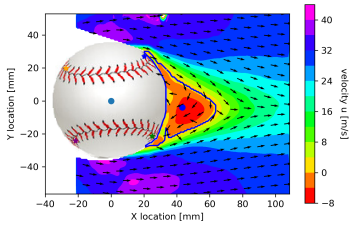

Figure 5.58: Time-averaged flow field baseball, 4-seam configuration with the top right seam at 127°.

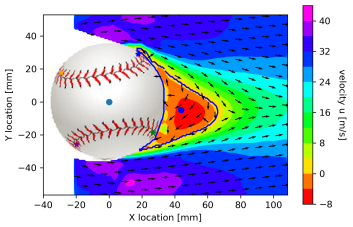

Figure 5.59: Time-averaged flow field baseball, 4-seam configuration with the top right seam at 122°.

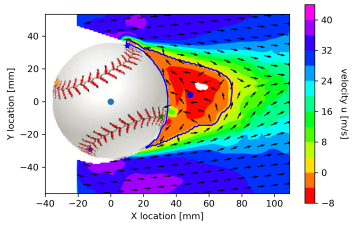

Figure 5.60: Time-averaged flow field baseball 4-seam configuration with the top right seam at 107°.

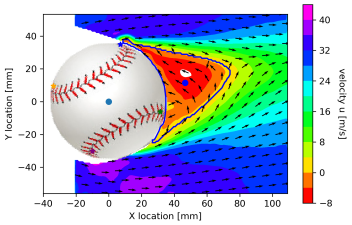

Figure 5.61: Time-averaged flow field baseball, 4-seam configuration with the top right seam at 102°.

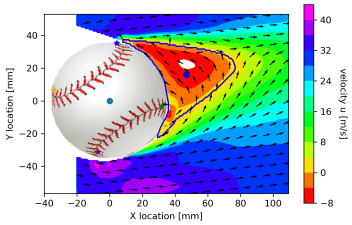

Figure 5.62: Time-averaged flow field baseball, 4-seam configuration with the top right seam at 97°.

The 4-seam configuration has separation at the seam, when at the top a seam is between 85 and 127°, see Figures 5.59 to 5.64. For separation angles between 85° and 95°, the wake is large. This behaviour occurs on both upper and lower side, hence the wake is approximately symmetric.

By rotating the baseball further, the top seam at 71° , see Figure 5.66) trips the flow into turbulence, leading to a later separation point. The bottom seam in Figure 5.66 causes separation at the back side, but rotating it further (see Figure 5.67 and 5.68) creates separation at the same angle, but a more balanced wake due to similar turbulent separation on both top and top side instead of due to a disturbance by a geometrical offset. By rotating it further, the starting position (Figure 5.57) is reached.

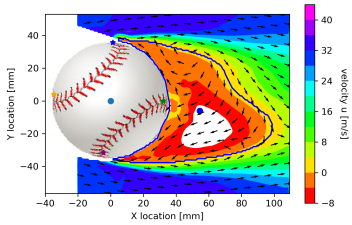

Figure 5.63: Time-averaged flow field baseball, 4-seam configuration with the top right seam at 92°.

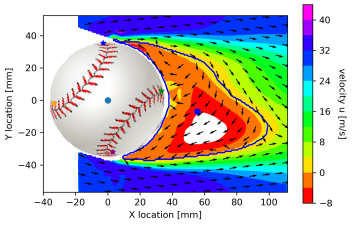

Figure 5.64: Time-averaged flow field baseball, 4-seam configuration with the top right seam at 85°.

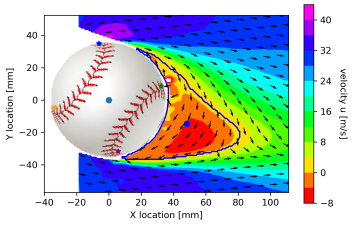

Figure 5.65: Time-averaged flow field baseball, 4-seam configuration with the top right seam at 80°.

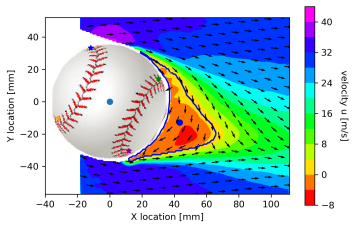

Figure 5.66: Time-averaged flow field baseball, 4-seam configuration with the top right seam at 71°.

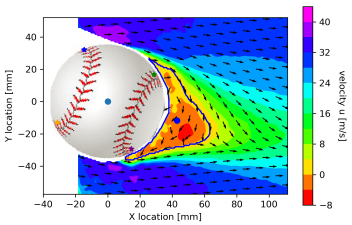

Figure 5.67: Time-averaged flow field baseball, 4-seam configuration with the top right seam at 66°.

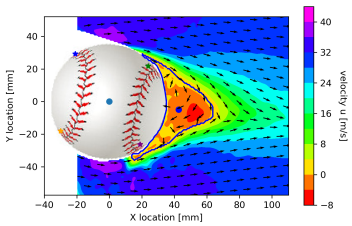

Figure 5.68: Time-averaged flow field baseball, 4-seam configuration with the top right seam at 54°.

The observed separation angles are summarised in Table 5.3 and visualised in Figure 5.69 and Figure 5.70. Here the grey lines are where a seam angle coincides with the separation location. The y_{cg} and the recirculation area are summarised in Table 5.4, and visualised in Figure 5.72 and Figure 5.71.

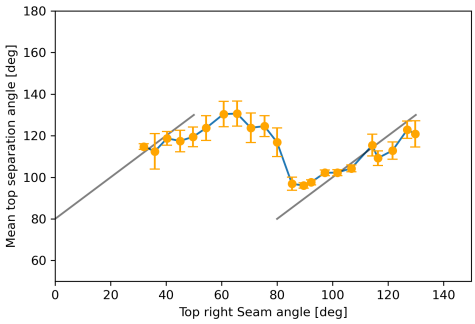

Figure 5.69: Overview top separation angle per configuration, within a bound of -1 and 1 standard deviation. As the baseball counterrotates, the top right seam will pass to the separation domain on the upper side and therefore is the influence with the flow can be observed. Separation on the seam is observed when then grey line intersects with the graph.

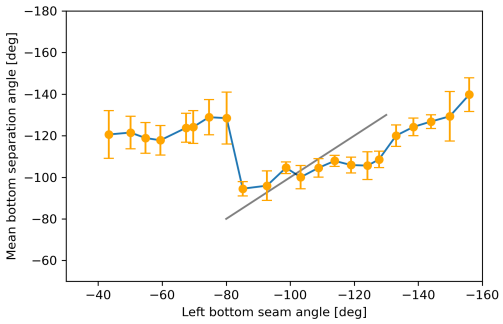

Figure 5.70: Overview bottom separation angle per configuration, within a bound of -1 and 1 standard deviation. As the baseball counterrotates, the bottom left seam will pass to the separation domain on the lower side and therefore is the influence with the flow can be observed. Separation on the seam is observed when then grey line intersects with the graph.

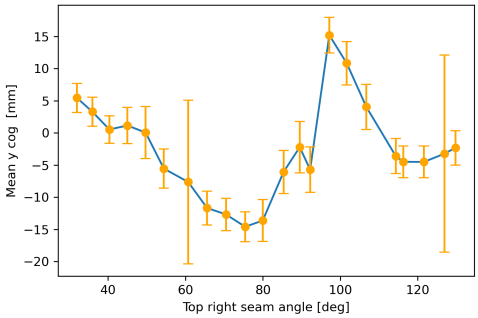

Figure 5.71: Overview y_{cg} per configuration, within a bound of -1 and 1 standard deviation

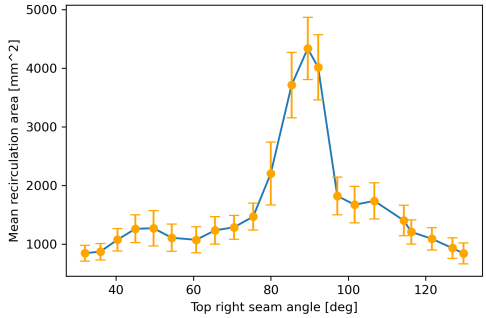

Figure 5.72: Recirculation area per configuration, within a bound of -1 and 1 standard deviation

The influence of the seams for the 4-seam are also captured as a pie chart over the baseball, to indicate in which regions the seams cause separation, are aft the separation or cause tripping, resulting into delayed separation. This is done in Figure 5.73. From a top right seam angle of approximately 85° to 127°, the flow separates at the seam position. If the top right seam angle is between 40° and 80°, the flow is tripped and there is turbulent separation. If the top right seam angle is larger than 130° or smaller than 40°, the top left seam or lower right seam are the dominating seam on the top side with respect to the flow effects, as the angles between the seams are approximately 90°

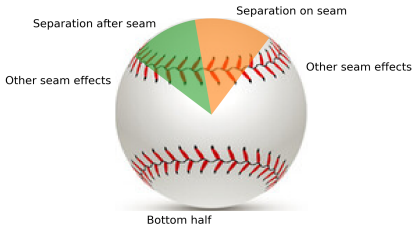

Figure 5.73: Area of influence of the seams on the 4-seam configuration. Orientation with respect to the top right seam

5.3.2. Statistical analysis of the static 4-seam configuration

For the 4-seam when the seams are not on the top (between 85 and 95°), turbulent separation is expected as seen in Section 5.3.1. This section discusses the stability of the separation points, recirculation area and the y_{cg}.

From Table 5.3, it is seen that the standard deviation for the bottom separation angle for the first few configurations (top right seam angle 130° to 97°), is quite high. Especially when compared to the results from the 2-seam configuration, see Table 5.1. This indicates that there is no apparent geometrical offset which causes abrupt separation. Instead the turbulent separation causes a highly varying separation angle on the top. This concurs with the Figures 5.57 to 5.62, where the seam is more aft than the separation point. However, the top separation angle has a smaller standard deviation, which decreases even more when rotating the ball counterclockwise. The flow appears to separate at the seam for the top side. This finding is supported by the standard deviation which decreases by rotating the baseball further. At top right seam angles 92° and 85° (Figure 5.63 and 5.64) the seams are tripping the flow into separation and a small standard deviation is found on both sides.

At 85° to 80° and smaller seam angles the behaviour changes. No longer is there top separation at the seam, but the seam trips the flow and separation is postponed. This coincides with the increasing standard deviation from the top side. On the lower side now appears there is now a influence from the seams, which does not longer cause turbulent separation, but instead let the separation occur earlier. The standard deviation on the top side is also lower than for the 85°+ configurations.

Top right seam angle [°]	BSA avg [°]	BSA StD [°]	TSA avg [°]	TSA StD[°]
130°	-148	11.3	125	6.2
127°	-127	7.5	124	4.1
122°	-122	6.9	117	4.0
107°	-128	7.6	104	1.7
102°	-136	8.1	102	1.3
97°	-144	9.9	102	1.4
92°	-93	3.4	97	1.2
85°	-105	2.8	96	3.3
80°	-103	5.3	118	6.7
71°	-108	2.5	122	6.8
66°	-107	3.3	134	5.9
54°	-111	3.6	125	5.8

Table 5.3: The top and bottom separation angle averages and standard deviations. The green color indicates top separation upstream of the seam. The yellow color indicates separation on or very close to the seam. The red color shows separation downstream of the seam.

The y_{cg} changes for the configurations. A maximum positive displacement of 14.8 mm at 97° with respect to the horizontal line passing through the center of gravity of the baseball is observed, while the maximum negative displacement is 15.2 mm at 80°. The standard deviation for the y_{cg} seams to remain constant, in the order of 2.5 - 3.5. For the seam at 80°, this is the configuration just rotated past where there was separation at the top side and bottom side due to a seam. Here one the top side the flow separates early due to the seam, where on the other side the seam trips the flow, making it transition and hence delayed separation. For the 97° this corresponds to the latest separation point on the lower side, while having roughly separation at the seam on the top side. The recirculation area shows the largest areas when the flow separates at both at the top and bottom at a seam, causing a large wake. This also causes the biggest standard deviations.

Top right seam angle [°]	y_{cg} [mm]avg	y_{cg} StD [mm]	recirc avg [mm^2]	recirc StD [mm^2]
130°	-2.8	2.7	711	177
127°	-5.0	2.8	823	176
122°	-6.0	2.5	977	190
107°	2.7	3.5	1596	307
102°	9.9	3.4	1412	312
97°	14.8	2.8	1536	321
92°	-7.1	3.5	3581	557
85°	-7.6	3.3	3224	559
80°	-15.2	3.3	1805	535
71°	-13.3	2.5	1063	204
66°	-11.9	2.6	1009	235
54°	-5.2	3.1	934	232

Table 5.4: The y_{cg} and recirculation area averages and standard deviations

5.3.3. Instantaneous flow analysis for the static baseball in the four-seam configuration.

In this section the results from the average velocity field and the average separation angles, y_{cg} and recirculation area are further analysed, by looking more in depth into the instantaneous images. Previously observed were the high standard deviations for the separation angles when dealing with late (turbulent) separation, while having moderate standard deviations when there appears to be separation at the seam. Also the shift in y_{cg} from positive to negative number and vice versa will be analysed further.

From Table 5.3, it is seen that the standard deviation for the bottom separation angle for the first few configurations (top right seam angle 130° to 97°), is quite high. With the top right seam at 130°, the standard deviations found on both the lower separation angle and the top separation angle were relatively large. The separation angle versus instantaneous image is shown in Figure 5.74 and 5.75. Here it can be observed that usually there is turbulent separation, which leads to a high standard deviation. For the bottom separation point can be observed that sometimes that there is laminar flow separation and hence separates early. This increases the standard deviation further.

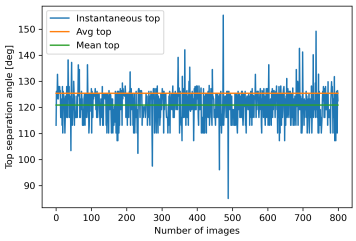

Figure 5.74: 4-seam, top right seam angle 130°: separation angle per instantaneous image

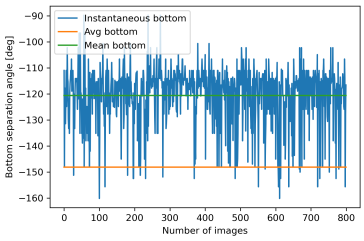

Figure 5.75: 4-seam, top right seam angle 130°: separation angle per instantaneous image

By rotating it further, the top and bottom separation points of the flow move more aft. The bottom separation becomes more spread, which leads to a higher standard deviation for turbulent separation and no seam to trip the flow into separation. The top separation angle has a high standard deviation for these seam angles (< 80◦), comparable to the starting configuration, indicating that the separation point fluctuates more. For a top right seam angle of 80 and 71°, this indicates that the top left seam (in Figure 5.65) has a double function. Sometimes this seam causes earlier separation and sometimes instead delays it. This can be observed in Figure 5.76 and 5.77, where the blue lines indicate the separation per instantaneous image, the ”avg” line is the separation angle according to the averaged velocity field,

while the ”mean” line represents the mean value of all the separate instantaneous separation angles. This wide range of angles is diminished, as the ball is rotated further (Figure 5.78), with the exception of some outliers. The 54° top right seam again has a wide range and a higher standard deviation, as the seam is just aft of the average velocity field separation angle. Hence for instantaneous images on instances it occurs before and on other instances it is still attached as it passes the seam and the seam helps delay the separation, hence creating cases for separation in the range of -115 to -125° and other cases with separation angles past -130°.

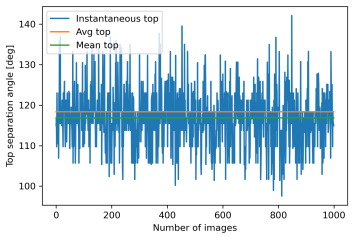

Figure 5.76: 4-seam, top right seam angle 80°: separation angle per instantaneous image

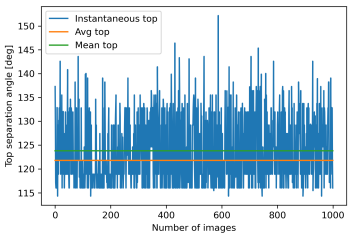

Figure 5.77: 4-seam, top right seam angle 71°: separation angle per instantaneous image

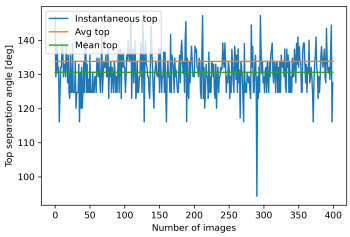

Figure 5.78: 4-seam, top right seam angle 66°: separation angle per instantaneous image

For the bottom separation angle, the standard deviation increases with the separation point moving more aft with the exception of 80°, where the standard deviation is higher than other seam configuration closely related. This is also seen in Figure 5.79, where separation is seen in a range from from -90 to -115°, indicating here also a double function for the seam (bottom right), sometimes directly separating and sometimes delaying separation. For other configurations like 71° (Figure 5.66), the range is much smaller, with the exception of a few outliers, as observed in Figure 5.80.

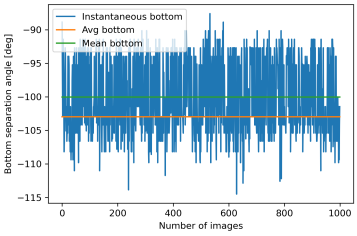

Figure 5.79: 4-seam, top right seam angle 80°: separation angle per instantaneous image

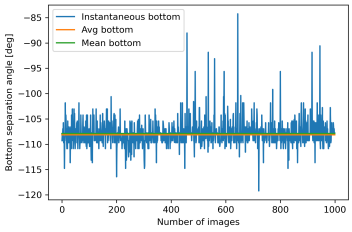

Figure 5.80: 4-seam, top right seam angle 71°: separation angle per instantaneous image

5.3.4. Comparison lift similarity parameter and centre of gravity shift for the non-rotational 4-seam configuration

The same approach as described in section 5.2.4 is also used for the 4-seam case, with the exception of the use of the reynolds stresses, as they have proven to be sufficiently small for the 2-seam case. The results are also made non-dimensional by dividing over the free stream dynamic pressure and the diameter of the baseball. The results can be seen in Figure 5.81 and 5.82

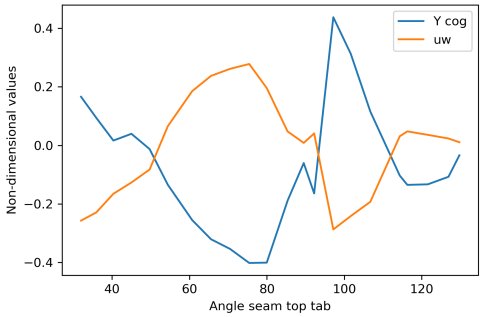

Figure 5.81: Comparison of the shift y_{cg} with the 2D lift proxy (non-dimensional).

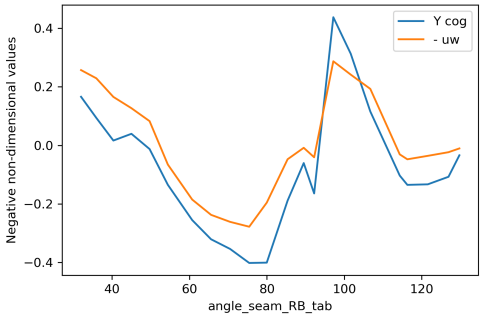

Figure 5.82: Comparison of the shift y_{cg} with the negative 2D lift proxy (non-dimensional).

Although this curve fits less ideally than for the 2 seam case, this shows sufficiently proof that the 4-seam shift in y_{cg} and the lift proxy derived from the conservation of momentum are a match. The discrepancy for the results are explained by the extra noise in the images, resulting in some errors in the flow field further downstream of the baseball, without impacting the results of the separation angles, centre of gravity or the recirculation area.

5.3.5. Comparison between the non-rotating cases

For the smooth sphere laminar separation is observed on both sides, even with the symmetry broken and the flow field a little bit more shifted upwards. The top side for the 2-seam and 4-seam will be discussed first. For the 2-seam case, 3 regions can be distinguished: < 80°, where there is turbulent separation with top separation angles between 110° and 130°, the region 80° to 110-120°, where the seams cause separation and > 120°, where the seams are behind the separation. This is different than for the 4 seam case, where only 2 regions are seen: The regions 90° to 130°, where the separation is on the seam, and the region 40° to 90°, where the seam trips the flow, causing turbulent and more aft separation.

For the bottom separation of the 4-seam a similar trend can be observed with respect to top side, now with negative angles, as is expected by symmetry. The 2-seam has a different effect, as there is no symmetry and the 2 seam is rotating over the upper half, while they are absent on the lower side. If the 2-seam has a negative top seam angle, it means the top seam is on the lower side. This causes the flow to early transition into turbulent, with a separation angle around -120°. If the top seam angle is positive, but smaller than 0°, both seams are on the top side and this causes the flow to separate laminar, similarly to the smooth sphere. However, as the top seam moves past 50°, separation becomes more turbulent, but also more erratic, as it moves -110 and -130°, due to the effect of the vertical seams, outside of the 2 seam measurement plane. Moving past a top seam angle 130°, causes the flow to separate earlier again, as the vertical seams cause separation.

The 2 seam and 4 seam cases therefore behave differently. While the 4 seam baseball is a case of a seam every 90 degrees, where the flow separates on the seam or has turbulent separation if the seam is < 90 degrees, with 4 symmetric cycles due to 4 seams, the 2 seam has a combination effect. On the upper side, the combination of the top and bottom seam near each other causes different (combined) separation effects, while on the lower side the 3D flow effects are also apparent as the vertical seam influence the flow not noticeably when they are aft of the separation point, but delay separation when being between -50 and -120°.

The recirculation area for the 4 seam case show mostly a smaller area, due to turbulent separation. Only when the seams are in the region 80-100°, the seams cause separation and the recirculation area is increased significantly. The 2 seam shows a more complex behaviour, due to the different behaviour

of the top and bottom. The average wake is usually larger than the 4 seam, while the recirculation area peaks are lower than the 4 seam, due to different peak areas (= early separation) for the top and bottom. The largest recirculation area for the 2-seam can be found between a top seam angle of 35 and 50°.

Due to the different peak areas of top and bottom separation, the y_{cg} of the 2 seam case also has a bigger spread, between 20 and -20 mm, while the 4 seam stays between 15 and -15 mm.

5.4. Rotating flow fields and comparison

In this section the results of the rotating smooth sphere and baseball are discussed. First the smooth sphere is analysed, to understand the clean configuration, before looking at the 2-seam and 4-seam configuration. The tested RPM's are 300, 600, 900, 1200, 1500 and 1800. For 0 RPM there should be no lift due to symmetry and hence also no shift in y_{cg}.

5.4.1. Rotating Smooth Sphere

The smooth sphere is rotating clockwise at different set constant RPM. Due to the baseball spinning in counterclockwise direction, the axis are mirrored to obtain the similar direction. However, as already seen in Section 5.1, there is a disturbance for the smooth sphere, resulting in a shift in y_{cg}. This shift is taken as the reference, and the shift of the y_{cg} is taken with respect of the reference and the geometrical center of the smooth sphere. As the RPM increases, the recirculaton area diminishes and the y_{cg} shifts upwards, as seen in Table 5.6 and Figure 5.83 to 5.88. This corresponds to the earlier explained Magnus effect.

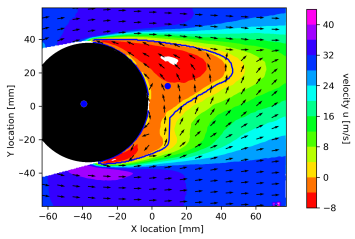

Figure 5.83: Smooth Sphere 300 RPM

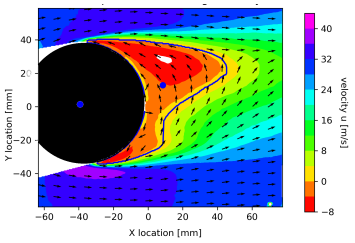

Figure 5.84: Smooth Sphere 600 RPM

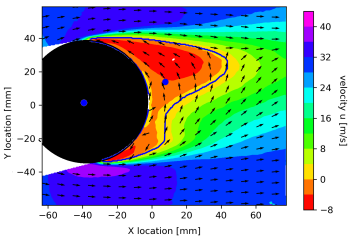

Figure 5.85: Smooth sphere 900 RPM

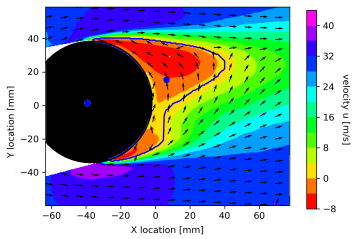

Figure 5.86: Smooth sphere 1200 RPM

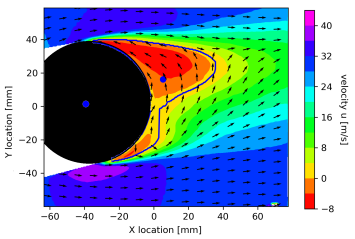

Figure 5.87: Smooth sphere 1500 RPM

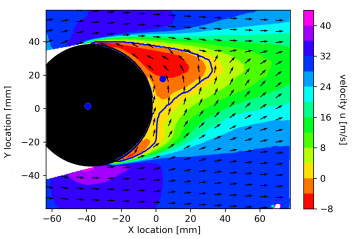

Figure 5.88: Smoothsphere 1800 RPM

	TSA avg	TSA mean	TSA StD	BSA avg	BSA mean	BSA StD
0 RPM	99.5	98.4	3.1	-104.6	-103.5	3.8
300 RPM	98.2	96.1	2.8	-104.1	-102.9	3.2
600 RPM	96.9	94.7	2.9	-105.6	-104.2	3.2
900 RPM	95.6	94.0	2.8	-107.8	-106.1	3.2
1200 RPM	94.9	93.4	2.9	-111.3	-108.8	3.6
1500 RPM	96.2	95.0	3.6	-114.1	-110.5	4.3
1800 RPM	93.6	93.4	3.3	-116.5	-115.0	3.6

Table 5.5: The top and bottom separation angles (average velocity field and mean separation angles) and standard deviations for set RPM

	y_cg avg	y_cg mean	y_cg StD	recirc avg	recirc mean	recirc StD
0 RPM	10.5	8.3	2.80	2257	3059	531
300 RPM	10.7	8.9	2.91	2288	3076	516
600 RPM	11.5	9.6	2.98	2199	2967	537
900 RPM	12.5	10.4	3.05	2060	2810	494
1200 RPM	14.0	11.9	3.17	1824	2525	462
1500 RPM	14.8	12.5	3.44	1570	2238	439
1800 RPM	16.4	14.0	3.50	1356	1980	412

Table 5.6: The y_{cg} and recirculation area averages and standard deviations for set RPM

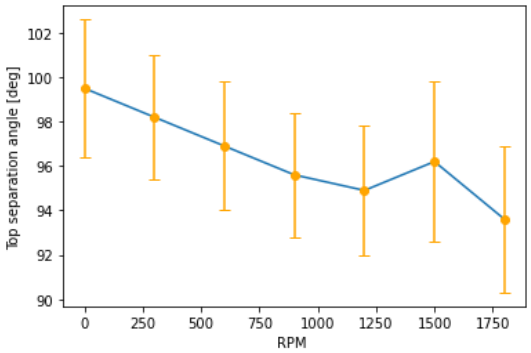

Figure 5.89: Overview top separation angle per configuration, within a bound of -1 and 1 standard deviation

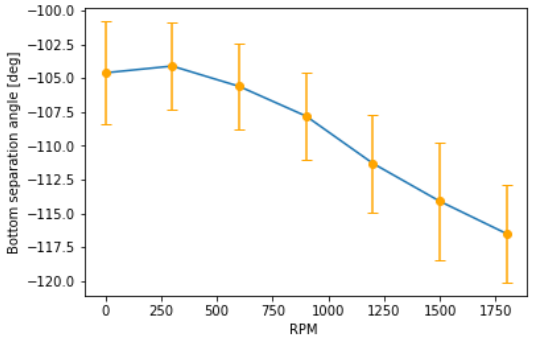

Figure 5.90: Overview bot separation angle per configuration, within a bound of -1 and 1 standard deviation

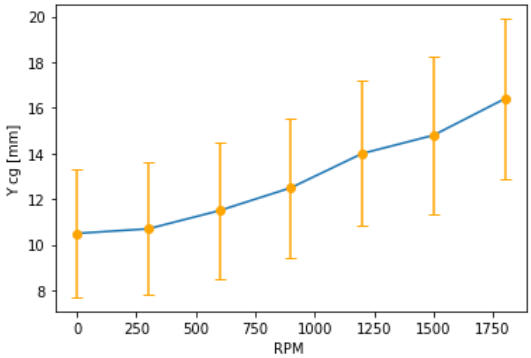

Figure 5.91: Overview y_{cg} per configuration, within a bound of -1 and 1 standard deviation

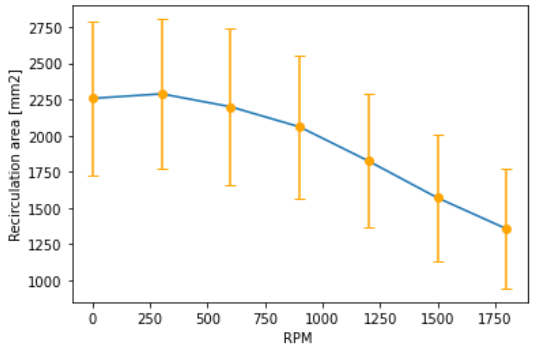

Figure 5.92: Recirculation area per configuration, within a bound of -1 and 1 standard deviation

5.4.2. Rotating 2-seam configuration

The baseball is rotating counterclockwise at different set constant RPM. In the 2-seam configuration the wake starts out small and the y_{cg} has a relative small vertical offset with respect to baseball center. As the RPM increases, this offset also increases. Also the wake similarly decreases, leading to a larger change of the y_{cg}. This is also seen in Table 5.8.

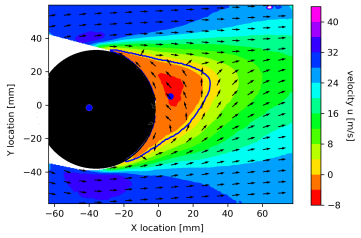

Figure 5.93: 2-seam 300 RPM

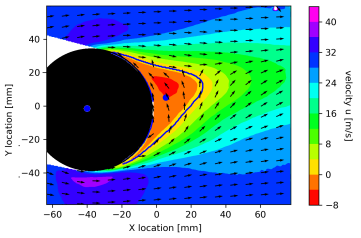

Figure 5.94: 2-seam 600 RPM

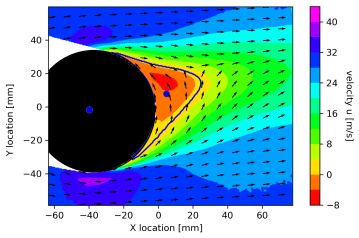

Figure 5.95: 2-seam 900 RPM

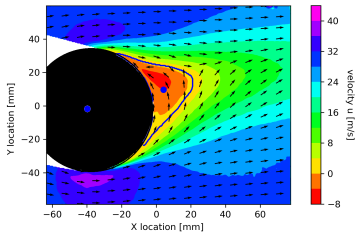

Figure 5.96: 2-seam 1200 RPM

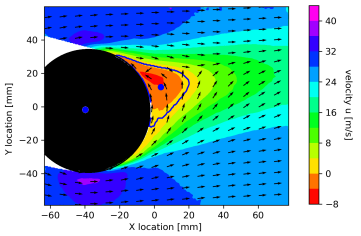

Figure 5.97: 2-seam 1500 RPM

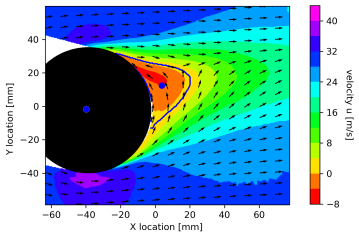

Figure 5.98: 2-seam 1800 RPM

The decrease of the wake size occurs rapidly from 300 RPM to 600 rpm and also noticeable steps are found between 600-1500 RPM, though the wake increases again at 1800. The standard deviation follows the same trend, decreasing rapidly from 300 to 600 RPM and then constantly diminishing, but diminishing less than the previous step. At 1800RPM also a higher standard deviation was found in comparison to 1500RPM.

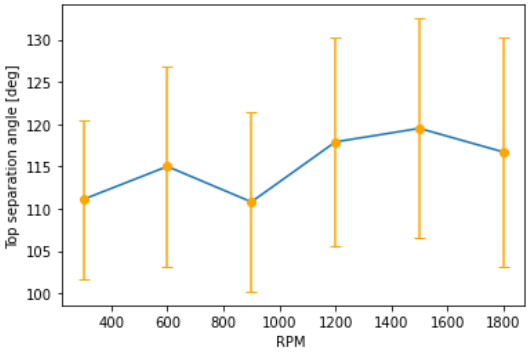

Figure 5.99: Overview top separation angle per configuration, within a bound of -1 and 1 standard deviation

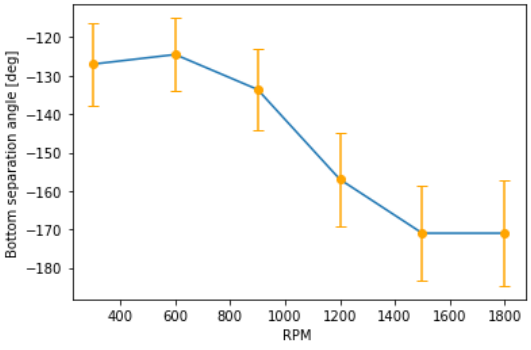

Figure 5.100: Overview bot separation angle per configuration, within a bound of -1 and 1 standard deviation

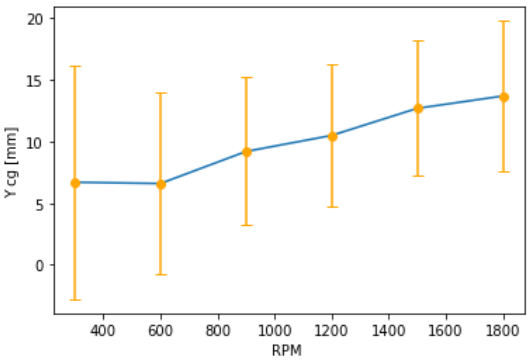

Figure 5.101: Overview y_{cg} per configuration, within a bound of -1 and 1 standard deviation

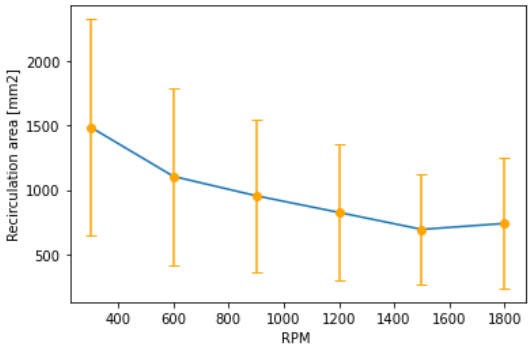

Figure 5.102: Recirculation area per configuration, within a bound of -1 and 1 standard deviation

	TSA avg	TSA mean	TSA StD	BSA avg	BSA mean	BSA StD
0 RPM	-	-	-	-	-	-
300 RPM	111.1	103.9	9.4	-127.0	-109.0	10.8
600 RPM	115.0	108.2	11.9	-124.5	-107.9	9.5
900 RPM	110.8	105.3	10.6	-133.6	-117.5	10.5
1200 RPM	117.9	105.9	12.3	-157.0	-121.6	12.1
1500 RPM	119.5	108.9	13.0	-171.0	-122.5	12.3
1800 RPM	116.7	108.1	13.6	-171.0	-128.6	13.7

Table 5.7: The top and bottom separation angles (average velocity field and mean separation angles) and standard deviations for set RPM

	y_cg avg	y_cg mean	y_cg StD	recirc avg	recirc mean	recirc StD
0 RPM	-	-	-	-	-	-
300 RPM	6.7	6.7	9.5	1485	2515	836
600 RPM	6.6	7.9	7.4	1105	1806	684
900 RPM	9.2	10.3	6.0	955	1573	588
1200 RPM	10.5	11.2	5.8	826	1379	528
1500 RPM	12.7	10.3	5.5	695	1244	425
1800 RPM	13.7	13.3	6.1	741	1302	503

Table 5.8: The y_{cg} and recirculation area (average velocity field and mean values) and standard deviations for set RPM

5.4.3. Rotating 4-seam configuration

For the 4-seam the wake is smaller for lower spin rates, as can be observed in Table 5.10. Due to the wake being smaller, with the same rotational energy the wake is deflected further, as observed from the y_{cg} data from Table 5.10. However, at higher spin rates the wake tends to have a larger size in 2D than for the 2-seam configuration, while the shift in y_{cg} is still more. Similar findings were found by Bin Lyu [42], were the drag value was higher for a rotating 2-seam than for a 4-seam. This was explained that for a higher spin rate, the drag is higher if more seams are exposed to the maximum airflow. The seam exposure index was found to be higher for the 4-seam than the 2-seam. Due to more exposure of the seams for the 4-seam, the flow is tripped more often into separation, while the extra velocity of the rotation causes the flow to be more turbulent and hence delay separation, with a smaller wake as a consequence. For lower spin rates, the seams from the 4-seam configuration have less separating effect and instead due to the combination of similar velocity and a lower RPM have a delayed separation working.

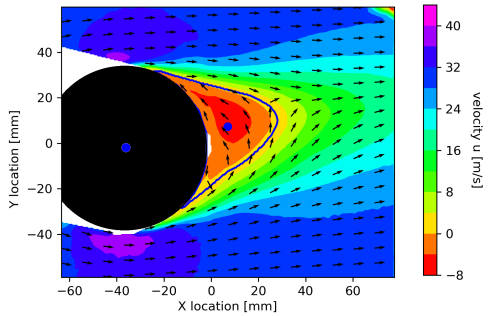

Figure 5.103: 4-seam 600 RPM

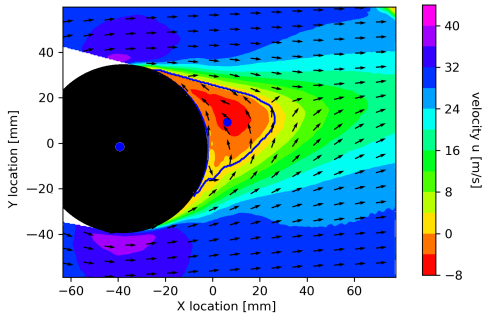

Figure 5.104: 4-seam 900 RPM

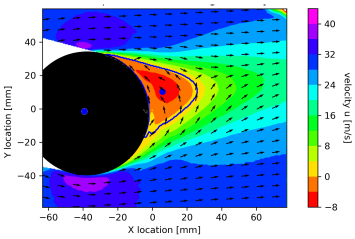

Figure 5.105: 4-seam 1200 RPM

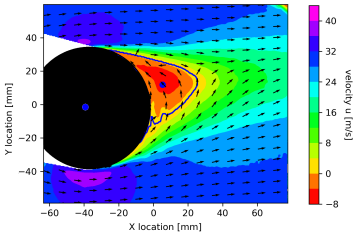

Figure 5.106: 4-seam 1500 RPM

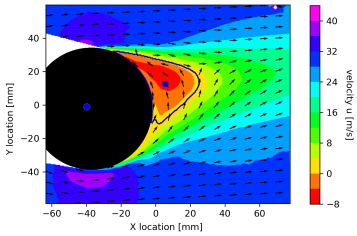

Figure 5.107: 4-seam 1800 RPM

From Table 5.10 also is seen that the wake has a similar response by decreasing in size, while the standard deviation also decreases. The standard deviation for the shift in center of gravity behaves accordingly, with the exception of 1200 RPM, where the standard deviation is larger than previous and next configurations (respectively 4.4 for 1200RPM, 5.0 for 1500RPM and 3.7 for 1800RPM).

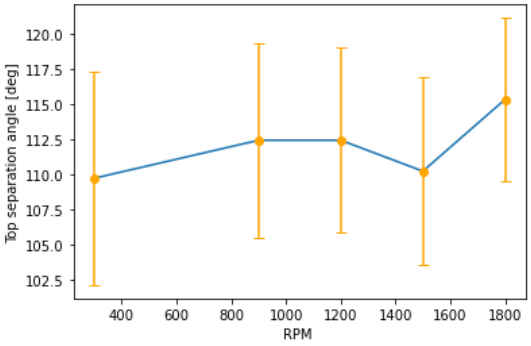

Figure 5.108: Overview top separation angle per configuration, within a bound of -1 and 1 standard deviation

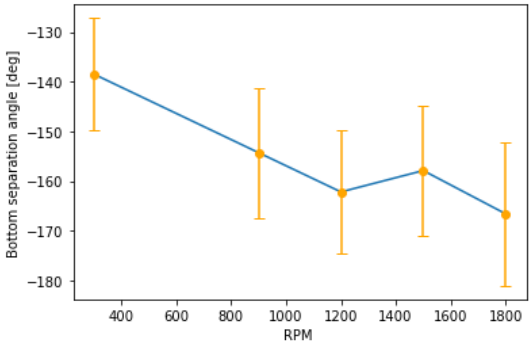

Figure 5.109: Overview bot separation angle per configuration, within a bound of -1 and 1 standard deviation

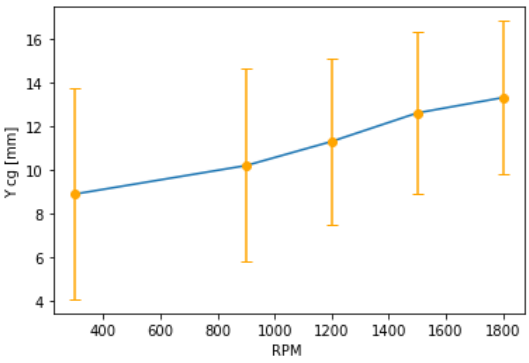

Figure 5.110: Overview y_{cg} per configuration, within a bound of -1 and 1 standard deviation

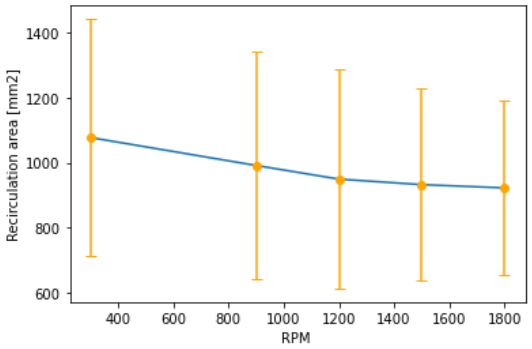

Figure 5.111: Recirculation area per configuration, within a bound of -1 and 1 standard deviation

	TSA avg	TSA mean	TSA StD	BSA avg	BSA mean	BSA StD
0 RPM	-	-	-	-	-	-
300 RPM	109.7	105.0	7.6	-138.5	-113.2	11.3
900 RPM	112.4	108.4	6.9	-154.3	-115.2	13.1
1200 RPM	112.4	108.3	6.6	-162.2	-113.6	12.5
1500 RPM	110.2	108.0	6.7	-157.9	-120.3	13.0
1800 RPM	115.3	112.6	5.8	-166.6	-123.0	14.5

Table 5.9: The top and bottom separation angles (average velocity field and mean separation angles) and standard deviations for set RPM

	y_cg avg	y_cg mean	y_cg StD	recirc avg	recirc mean	recirc StD
0 RPM	-	-	-	-	-	-
300 RPM	-	-	-	-	-	-
600 RPM	8.9	8.6	4.8	1077	1516	365
900 RPM	10.2	9.2	4.4	991	1401	351
1200 RPM	11.3	8.7	3.8	949	1374	337
1500 RPM	12.6	10.4	3.7	932	1325	296
1800 RPM	13.3	10.1	3.5	922	1324	270

Table 5.10: The y_{cg} and recirculation area averages and standard deviations for set RPM

5.4.4. Comparison between the rotating cases

In this section the results of the rotating and static tests are compared with mainly the focus on the y_{cg}. The comparison will be done based on a similar shift in y_{cg} and then investigating how the recirculation area and separation angles differ. It can be observed from Figure 5.112 that the 4-seam experiences a large shift in centre of gravity than the 2-seam. This corresponds with literature data and is explained due to the multitude of the seams. For the 4-seam every ±90° a seam passes by, which causes at this velocity and spin rate to trip the flow and make it turbulent. This leads to a smaller recirculation area, as also can be observed in Figure 5.113, which due to the same momentum from the baseball experiences a larger deflection of the recirculation area. The smooth sphere does not have seams and hence does not experience any tripping behaviour. Instead the smooth sphere offset of the y_{cg} behaves approximately linear, as expected by the 2D Kutta-Jouwkowski theorem, which links the circulation (=spin) linearly with the lift (= displacement of the y_{cg}). The offset from the linear line can be explained due to the change in behaviour in the boundary layer.

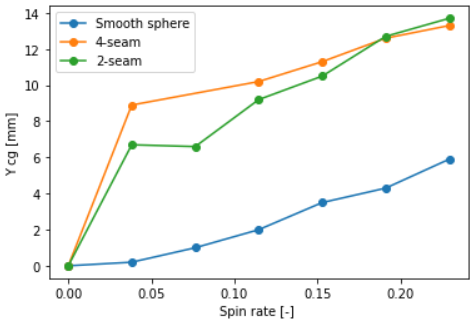

Figure 5.112: Spin rate vs centre of gravity

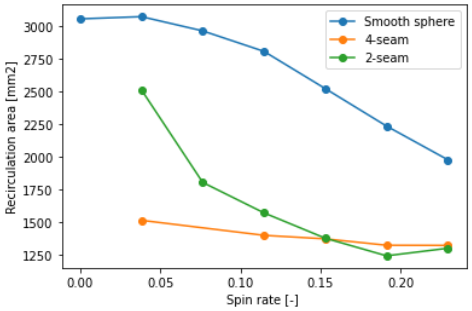

Figure 5.113: Spin rate vs recirculation area

The top and bottom separation angles per spin rate can be observed in Figures 5.114 and 5.115. For the top separation angles, it can be observed that the smooth sphere has separation at ±90°, corresponding to a laminar separation. Due to the increasing rotation, the adverse gradient inside the boundary layer builds up and causes earlier separation. For the baseball however a different trend is observed, for both 2-seam and 4-seam configuration. The rotation causes the seams to pass faster over the flow, tripping the flow and hence delaying separation. The pure rotation without seam effect causes the adverse pressure gradient to increase and would cause earlier separation, without the seam effects, as was observed for the smooth sphere. This however is not a dominating effect, as the baseball separation moves the other way. For the 2-seam case it is more balanced, causing the separation point to move a little more aft or forward, depending on the RPM or spin rate, though generally the separation point moves more aft.

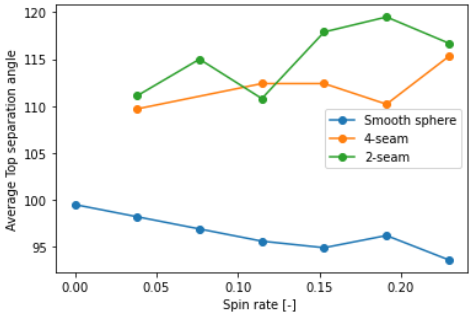

Figure 5.114: Spin rate vs top separation angle

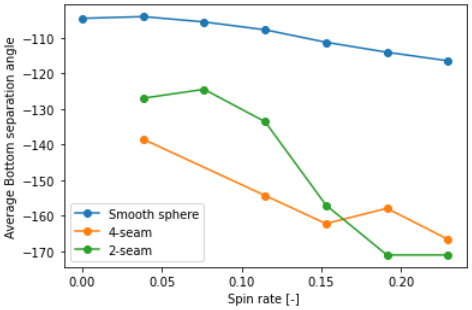

Figure 5.115: Spin rate vs bottom separation angle

The bottom separation angle for the smooth angles tends to move more aft per increasing RPM configuration. As the ball rotates, which yields a velocity in the same direction as the flow, the boundary layer is re-energised and the separation is delayed. A similar trend is observed for the 2-seam and 4-seam, but now the tripping of the seams have an effect in the same direction. This is observed in the plot, where the slope of the separation angle is steeper, meaning that the separation point is moving more aft per configuration than for the smooth sphere.

5.4.5. Comparison between the non-rotating and rotating cases with similar configuration

The 2-seam rotating cases show a shift in centre of gravity from 6.7 to 13.7 mm. This corresponds to a static case with top seam angle 152-140°, meaning that both seams lie on the top half, near the front. This is intuitive as the seams disturb the boundary layer, such that it transitions more on the top side and moves the top separation point more aft, in a similar fashion in the case of the rotating baseball, where the rotation of the seams and the Magnus effect cause an upwards shifted wake.

The 4-seam rotating cases show a shift in centre of gravity from 8.9 to 13.3 mm. This corresponds to the static case with a top right seam angle of 106 to 97°. This can be explained by the fact that when

the top right seam angle is smaller, the separation follows the seam and a separation angle will occur in the range of laminar separation, which is too early. If the top right seam angle is even smaller, it will trip the flow and the flow will becomes turbulent, which would lead to a more aft separation angle than for the rotating case. If the top right seam angle would be larger than 106°, the lower side would have laminar separation, while having turbulent separation on the top side and the centre of gravity of the recirculation would shift to the lower side of the flow field, below the horizontal line through the centre of gravity of the baseball.

5.4.6. Literature data versus shift in centre of gravity experimental data

With the help of the flow fields, the precise working of the seams on the wake and hence the lift coefficient are illustrated. Using the results as proof, the shift in y_{cg} can thus be used to compare the difference in lift quantities. Although these results are an indication of how the seams influence the flow, this is not the total situation as this analysis is only in 2D. The next step is to compare them with the lift coefficient from literature data. For this a scaling factor was used. The offset in the centre of gravity of the smooth sphere was scaled with the lift coefficient of a smooth sphere for a spin rate of 0.2, which is approximately 0.1. Using this scale factor, an overlap figure was made between the literature data and the results from the experiment, as shown in Figure 5.116. The RPM is converted into the spin parameter using Equation 2.4.

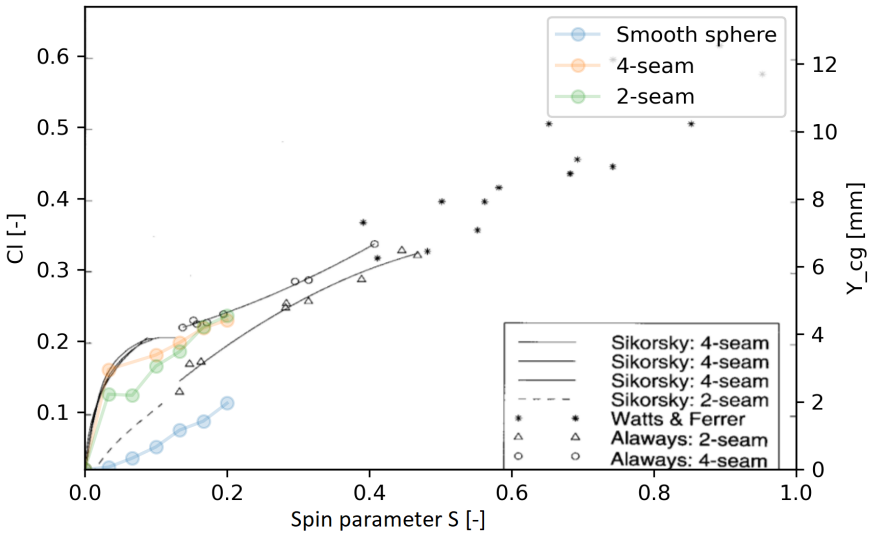

Figure 5.116: Cl vs low spinrate for 4-seam and 2-seam ball [8]

The 2D planar PIV results show a similar response comparing it to the lift coefficient from literature, with also a difference between the 4-seam and 2-seam configuration, where the 4-seam configuration has a higher lift coefficient and larger shift in y_{cg}. The same behaviour where the lift coefficient first increases more rapidly, before approaching a constant linear increase is found. The 2-seam configuration appears to have a larger shift in centre of gravity than for the literature data shows, making the difference with the 4-seam configuration smaller. This can be attributed to the effect of 2D vs 3D, where the shift in centre of gravity is solely taken in 1 plane, while the lift coefficient is for the whole baseball.

6

Conclusion

This thesis focused on the effects of the seam locations on the flow around a baseball, for the 4-seam and 2-seam configuration. The effects were demonstrated by means of 2D planar PIV. The high repetition rate led to statistical convergence, while understanding the 2D planar movement of the flow field for a Reynolds number of 150,000 for low spin configurations. The conclusions of this research are given in Section 6.1, which is followed by the recommendations for future research and development. This is done in Section 6.2.

6.1. Conclusions

Typically baseball measurements are often done by measuring the deflection of a ball and then working backwards to find the corresponding spin and influence, without havng a fully solved flow field. This thesis provides additional data and understanding to the effect of the seams, by answering the following research question:

"What is the effect of the location of the seams of a slow or non-rotating baseball (Spin factor < 0.2) on the wake by visualizing it using 2D planar PIV recording in a wind-tunnel?".

with corresponding sub questions:

1. *"Can the lift coefficient be compared with the y-centre of gravity of 2D planar PIV for baseballs and does it behave similarly?"*
2. *"At which angles can the seam influence be noticed to do nothing, cause transition or cause separation?"*
3. *"Does the stability of the separation angles, wake size and wake centre of gravity change for these specific seam cases?"*
4. *"How does the stability behave for these configurations differ by looking at the mean and standard deviation of the y centre of gravity and separation angles?"*
5. *"Is the perceived influence of the seams on the non-rotational baseball case different for small RPM and is this solely the magnus effect or also a combination of the seam effects with magnus effect?"*
6. *"Why do the 2-seam and 4- seam configurations differ for low spin factors (S < 0.2) baseballs by looking at the y centre of gravity?"*

In this thesis it is proven that for the 2-seam and 4-seam configuration for a Reynolds number of 150,000 for low spin configurations indeed a comparison can be made between the shift in centre of gravity of the recirculation area and the 2D lift proxy, which behaves similarly when compared with the earlier found experimental values.

Furthermore, for both the static 2-seam and 4-seam the areas of influence of the seams are found and given in Figures 6.1 to 6.3. For the 2-seam configuration, the top seam causes between approximately 75 and 105° separation on the seam, while separation on the lower seam is between 40 and 75°. The 4-seam experiences separation on the seam when it is located between 85° and 125°.

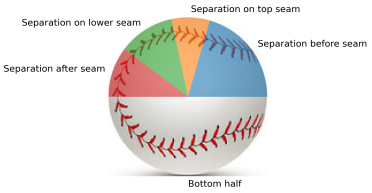

Figure 6.1: Area of influence of the seams on the 2-seam configuration. Orientation with respect to the top seam

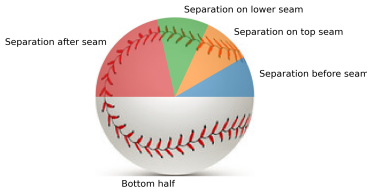

Figure 6.2: Area of influence of the seams on the 2-seam configuration. Orientation with respect to the bottom seam

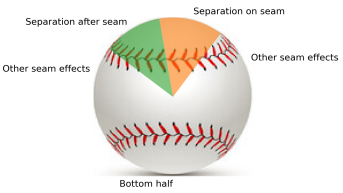

Figure 6.3: Area of influence of the seams on the 4-seam configuration. Orientation with respect to the top right seam

The stability of these cases also changes accordingly. For separation on the seam, the separation point is more precise in the sense that for most instantaneous images the separation point varies less than for other cases. However, due to the nature of the seam, for a few instantaneous cases there a large discrepancies observed, as the seam would not cause separation, but instead cause flow tripping, leading to turbulent and hence more aft separation. When flow tripping occurs, the standard deviations tend to differ more as there is not a geometrical offset anymore causing the separation. Instead the highly energized boundary layer tends to have more differences between the instantaneous images, leading to a more fluctuating separation point. For laminar separation there is less energy and also in many cases the detection point is after 80 or even 90°, making the separation more fixed.

From the difference in behaviour from the upper side and lower side of the baseball for both the 4 seam and 2 seam cases, indeed a combination effect can be observed. For the lower side, the clockwise rotation causes an additional velocity in the opposite direction as the wind, leading to an effective higher velocity and more turbulent flow on the lower side, with a more aft separation point (as seen in Figures 5.100 and 5.109) . On the upper side, the clockwise rotation is counteracting the wind flow and therefore the different effects are counteracting each other, leading to a more fluctuating trend (as seen in Figures 5.99 and 5.108).

To answer the final sub question, the size of the recirculation area is investigated. It is shown that due to the configuration of the 4-seam with more appearing seams and more evenly distributed, the flow experiences more often these seams, which trips the flow and causes turbulent separation, leading to a smaller wake. The smaller wake has a smaller mass, which can be deflected further with similar Magnus force, leading to a higher lift force and hence coefficient in the other direction. When the spin ratio reaches a threshold of approximately > 0.2, the seams of the 2-seam configuration also frequents often enough leading to flow tripping and turbulent separation, with similar lift and lift coefficients as for the 4-seam case.

6.2. Recommendations

Although the results of this thesis mirror the expectations of other literature data, important short-cuts are taken and need to be addressed appropriately. For a high statistical convergence, this experiment was performed in a windtunnel. This included a boxed test section (40cm x 40cm) and a rod through the centre of the baseball. The walls could lead to small effects, such as blockage (although demonstrated in Chapter 4 that this effect will be negligible). But the main deviation from reality is the rod. This rod causes some flow deflections, which are not experienced in free flight. The effects of the rod appear

especially when looking at a supposed balanced, symmetrical case of the smooth sphere. Therefore, these results should be compared with data from free flight to extrapolate these findings further.

Another important shortcut is the working of 2D planar PIV data. For a fully correct assessment, the whole flow field should be considered, especially when considering the pattern of the seams. Although the trend of the data aligns with literature data, the expressed quantities of this research are not 3D lift coefficients.

Also important are the limitations of the test configurations. This thesis has focused solely on the 2-seam and 4-seam configuration, with a perfect rotation through the centre of the baseball. Different, more intermediate configurations between these 2 configurations have not been researched and a hybrid configuration could very well cause a different break of symmetry, with different flow effects as a consequence. Also the rotation itself in a windtunnel is different, as the baseball rotates through the geometrical centre. However, a baseball has an offset between the geometrical centre and the centre of mass, due to different sort of material. Therefore, the baseball ”wobbles” more in free flight, while the windtunnel tests ignore this.

The velocity itself plays also an important role. Due to limitations of the windtunnel, the wind velocity could not exceed 30 m/s. However, as stated in Chapter 1, a common velocity in professional baseball is roughly 100 mph, translating to approximately 45 m/s and a reynolds number of not 150,000, but 225,000. And with a higher translational velocity, also a higher rotational velocity is needed to maintain a similar area of interest for the spin ratio. This would lead to different velocities on the upper and lower side, with also a different frequency of seam appearances and different separation behaviour.

Bibliography

[1] Elmar Achenbach. Experiments on the flow past spheres at very high reynolds numbers. *Journal of Fluid Mechanics*, 54:565–575, 1972.

[2] Elmar Achenbach. Vortex shedding from spheres. *Journal of Fluid Mechanics*, 62:209–221, 1974.

[3] Robert K. Adair. The physics of baseball. *Physics Today*, pages 26–31, 1995.

[4] Robert K. Adair. Comment on ‘‘how to hit home runs: Optimum baseball bat swing parameters for maximum range trajectories,’’ by gregory s. sawicki, mont hubbard, and william j. stronge. *American Journal of Physics*, 73:184–185, 2005. doi: 10.1119/1.1794754.

[5] Sagar Adatrao and Andrea Sciacchitano. Elimination of unsteady background reflections in piv images by anisotropic diffusion. *Measurement Science and Technology*, 30(3), 2019. doi: 10.1088/1361-6501/aafca9.

[6] L.W. Alaways. *Aerodynamics of the curve ball: An investigation of the effects of angular velocity on baseball trajectories*. University of California, 1998.

[7] L.W. Alaways and M. Hubbard. Experimental determination of baseball spin and lift. *Journal of Sports Sciences*, 19:349–358, 2001. doi: 10.1080/02640410152006126.

[8] L.W. Alaways and M. Hubbard. Aerodynamics of golf balls in still air. *Journal of Sports Sciences*, 19:349–358, 2001.

[9] GRETCHEN ALPER. Ccd versus cmos: Blooming and smear performance. *Sensor Technology and Characteristics, Image Quality Improvements*, 2 2015.

[10] Constantin Jux annd Fulvio Scarano and Andrea Sciacchitano. Aerodynamic pressure reconstruction on generic surfaces from robotic piv measurements. *Proceedings of the 13th International Symposium on Particle Image Velocimetry*, 2019. doi: DOI:10.18726/2019_3.

[11] TSI Incoporated (Corporate author). Definition of “time-resolved” for piv data. *APPLICATION NOTE TRPIV-003 (US)*, 2014. URL URL:https://tsi.com/getmedia/79f90407-b1e2-487a-864c-cfa138df5d2a/TRPIV-003_TRPIV_Definition_of_Time_Resolved_PIV_Data-US-web?ext=.pdf. ”[Online; accessed on 13 June 2021]”.

[12] TU Delft (Corporate author). W-tunnel, 2021. URL URL:https://www.tudelft.nl/lr/organisatie/afdelingen/aerodynamics-wind-energy-flight-performance-and-propulsion/facilities/low-speed-wind-tunnels/w-tunnel. ”[Online; accessed on 13 June 2021]”.

[13] Bartonlsmith. Effect of seam height on wake of mlb baseballs: post 35. https://www.baseballaero.com/2019/10/06/effect-of-seam-height-on-wake-of-mlb-baseballs-post-34/, 6 October 2019. [Online; accessed on 27 November 2019].

[14] P.J. Brancazio. The physics of a curveball. *Popular Mechanics*, Volume 174 (10):pp 56–57, 1997.

[15] David M. Bremner, Florence V. Hutcheson, and Daniel J. Stead. *Methodology for the Elimination of Reflection and System Vibration Effects in Particle Image Velocimetry Data Processing*. The NASA STI Program, February 2005.

[16] L. J. Briggs. Effects of spin and speed on the lateral deflection (curve) of a baseball and the magnus effect for smooth spheres. *American Journal of Physics*, 27:589–596, 1959.

[17] Quantel Laser by Lumibird. Evergreen2 (70-200 mj at 532 nm), a state of the art laser for piv. https://www.quantel-laser.com/en/products/item/evergreen-70-200-mj-.html, 2021. [Online; accessed on 27 november 2019].

[18] Juan G. Santiago Carl D. Meinhart, Steve T. Wereley. A piv algorithm for estimating time-averaged velocity fields. *Journal of Fluids Engineering*, June 2000.

[19] Lavision (corporate author). Piv, 2021. URL URL:https://www.piv.de/piv/measurement_principle/page_1.php. "[Online; accessed on 13 June 2021]".

[20] Anchal Sareen et al. Flow past a tranversely rotating sphere. *11th International Conference on Flow- induced vibrations*, 3 2016.

[21] C. Brossard et al. *Principles and applications of particle image velocimetry*. Aerospace Lab Alain Appriou, 2009.

[22] Firoz Alam et al. Aerodynamics of baseball. *Procedia Engineering 13 (2011)*, 207–212, 2011. doi: 10.1016/j.proeng.2011.05.074.

[23] G. Elsinga et al. Tomographic particle image velocimetry. *Exp Fluids*, 41:933– 947, 2006.

[24] Jim Albert et al. Report of the committee studying home run rates in major league baseball. Technical report, Bowling Green State University et al., 24 May 2018.

[25] Markus Raffel et al. *Particle Image Velocimetry A Practical Guide 3rd edition*. Springer International Publishing AG, part of Springer Nature, 2018. ISBN ISBN 978-3-319-68851-0. doi: 10.1007/978-3-319-68852-7.

[26] H. Hu et all. An experimental study of stall hysteresis of a low-reynolds-number airfoil. *International Journal of Aerospace and Lightweight Structures*, Vol. 1, No. 2:pp 221–238, 2011. doi: 10.3850/S2010428611000171.

[27] Sawicki et all. How to hit home runs: Optimum baseball bat swing parameters for maximum range trajectories. *American Journal of Physics*, 71:1152–1162, 2003.

[28] T. Haugen et all. Reaction time aspects of elite sprinters in athletic world championships. *Journal of strength and conditioning research*, 4 2013. doi: 10.1519/JSC.0b013e31826520c3.

[29] Cliff Frohlich. Aerodynamic drag crisis and its possible effect on the flight of baseballs. *American Journal of Physics*, 52:325–334, 1984. doi: 10.1119/1.13883.

[30] J Katz G.I. Roth. Five techniques for increasing the speed andaccuracy of piv interrogation. *Measurement Science and Technology*, 12, 238–245, 2001.

[31] R. Gonzalez. Why it's almost impossible for fastballs to get any faster. *Wired*, 12 2018. URL https://www.wired.com/story/why-its-almost-impossible-for-fastballs-to-get-any-faster/. [Online; accessed on 27 november 2019].

[32] Nancy Hall. Dragsphere. https://www.grc.nasa.gov/www/k-12/airplane/dragsphere.html, 2021. [Online; accessed on 14 May 2021].

[33] hbm machines. Tachometer, 2021. URL URL:https://www.hbm-machines.com/producten/hbm-digitale-toerenteller-met-laser. "[Online; accessed on 13 June 2021]".

[34] Hiroshi Higuchi. Aerodynamics of knuckle ball: Flow-structure interaction problemon a pitched baseball without spin. *Journal of Fluids and Structures*, Vol. 32:pp. 65–77, 2012.

[35] R. Himeno. Computational study of influences of a seam line of a ball for baseball on flows. *The Visualization Society of Japan and Ohmsha, Ltd.*, Vol. 4(2):pp. 197–207, 2001. doi: 10.1119/1.1990332.

[36] Dr. Ing. S. Hoerner. *Fluid-Dynamic Drag*. Published by the author, United States of America, 1965.

[37] Lloyd V. Smith Jeffrey R. Kensrud. In situ drag measurements of sports balls. *8th Conference of the International Sports Engineering Association (ISEA)*, pages 2437–2442, 2010. doi: 10.1016/j.proeng.2010.04.012.

[38] T. Jinji and Shinji Sakura. Direction of spin axis and spin rate of the pitched baseball. *Journal of Sport Biomechanics*, 5:2:pp 197–214, 7 2006. doi: 10.1080/14763140608522874.

[39] T. Jinji and S. Sakurai. Direction of spin axis and spin rate of the pitched baseball. *Sports Biomechanics*, 5:197–214, 2006.

[40] Jeffrey Kensrud. Determining aerodynamic properties of sports balls in situ. Technical report, Washington State University, Department of Mechanical and Materials Engineering, 2010.

[41] LaVision. Imager scmos product information.

[42] Bin Lyu, Jeff Kensrud, and Lloyd Smith. Investigation of the aerodynamic drag of baseballs with gyro spin. *Proceedings*, 49, 2020. doi: 10.3390/proceedings2020049162.

[43] Takashi Furui Matsushi Nishiyama, Minh Khoi Le and Yuji Ikeda. Simultaneous in-cylinder flow measurement and flame imaging in a realistic operating engine environment using high-speed piv. *Applied Sciences*, 9(13), 2019. doi: 10.3390/app9132678.

[44] Rabindra D. Mehta. Aerodynamic of sport balls. *Annual Review of Fluid Mechanics*, 17:151–189, 1985.

[45] Rabindra D. Mehta and Jani Macari Pallis. Sports ball aerodynamics: Effects of velocity, spin and surface roughness. Technical report, NASA Ames Research Center, 2001.

[46] Alan M. Nathan. The effect of spin on the flight of a baseball. *American Journal of Physics*, 76: 119–124, 2008. doi: 10.1119/1.2805242.

[47] Robert Bleischwitz Roeland de Kat. Towards instantaneous lift and drag from stereo-piv wake measurements. *18th International Symposium on the Application of Laser and Imaging Techniques to Fluid Mechanics*, 2006.

[48] T. Sawchik. Baseball's top staffs have come around on the high-spin fastball. *FiveThirtyEight*, 10 2018. URL https://fivethirtyeight.com/features/baseballs-top-staffs-have-come-around-on-the-high-spin-fastball. [Online; accessed on 27 november 2019].

[49] F. Scarano. Course reader for the students of flow measurement techniques, 2013.

[50] A. Spoelstra. Aerodynamics of transiting objects via large-scale piv - the ring of fire concept. *TU Delft, Faculty of aerospace engineering*, 2017.

[51] L. Veldhuis. Lecture sheets aircraft aerodynamics. *Aircraft Aerodynamics*, 2019.

[52] Frank L. Verwiebe. Does a baseball curve? *American Journal of Physics*, Vol. 10:pp. 119–122, 1942. doi: 10.1119/1.1990332.

[53] R. G. Watts and R. Ferrer. The lateral force on a spinning sphere: Aerodynamics of a curve ball. *American Journal of Physics*, 55:40–44, 1987.

[54] Robert G. Watts and Eric Sawyer. Aerodynamics of a knuckleball. *American Journal of Physics*, 43:960–963, 1975. doi: 10.1119/1.10020.

[55] J. Westerweel. Theoretical analysis of the measurement precision in particle image velocimetry. *Exp. Fluids (Suppl.*, S3-S12, 2000.

[56] Bernhard Wieneke. *PIV Uncertainty Quantification and Beyond*. Technische Universiteit Delft, December 2017.

[57] Chong Yao Wong. *Flow within and in the near external field of a fluidic precessing jet nozzle*. University of Adelaide, Department of Mechanical Engineering, 2004.